**Title**
Detailed Balance Modeling of Novel Solar Fuels Designs

**Permalink**
https://escholarship.org/uc/item/4sj4n3vj

**Author**
Keene, Samuel

**Publication Date**
2018

Peer reviewed|Thesis/dissertation

UNIVERSITY OF CALIFORNIA,
IRVINE


Detailed Balance Modeling of Novel Solar Fuels Designs

DISSERTATION


submitted in partial satisfaction of the requirements
for the degree of


DOCTOR OF PHILOSOPHY

in Physics


by


Samuel Thomas Keene

2018

# DEDICATION

To Christine,

You've been there every step of the way. You gave me the courage to make tough decisions, motivated me to do my best, and cheered me up when things didn't go my way. It's been a long road for both of us but we did it together. I'm so excited to be starting the next chapter of my life with you.

Love, Sam

# TABLE OF CONTENTS

# LIST OF FIGURES

# LIST OF TABLES

# ACKNOWLEDGMENTS

Thank you very much to Prof. Shane Ardo, who took me on as a 4th year grad student and allowed me to have free reign over where I thought my project should go. I really appreciate the care and interest you take in making sure your students are happy and successful. I'm happy to be graduating as a member of the Ardo lab!

Thanks to all of my past and present labmates in the Ardo group: Bill Gaieck, Dr. David Fabian, Joseph Cardon, Will White, Jen Glancy, Kevin Tkaczibson, Simon Luo, Eric Schwartz, Rohit Bhide, Nazila Farhang, Leanna Schulte, Anni Zhang, Baldwin Liwanag, Prof. Rohini Bala Chandran, Dr. Larry Renna, Prof. Jingyuan Liu, Dr. Chris Sanborn, Margherita Taddei, and Prof. Mohammad Qureshi. It's been great working with all of you!

Thanks to everyone I worked with in the Law group before I left: Dr. Mark Gibbs, Dr. Jason Tolentino, Dr. Vineet Nair, Dr. Amanda Weber, Dr. Moritz Limpinsel, Dr. Nima Farhi, Mohammed El Makkaoui, Trenton Salk, Alex Abelson, Zhongyue Luan, Glen Junor, Kan Fu. You guys were great and made working for a horrible PI a little more enjoyable. In particular thanks to Mark for being a terrific mentor in my first year.

Most of all, thanks to Christine, Boots, and all of my friends and family. You've all been amazingly supportive and I'm lucky to have you in my life.

# CURRICULUM VITAE

## Samuel T. Keene

## Professional Experience

Dec. 2016 – Nov. 2018    *Ph.D. Student Researcher*, Ardo Group, University of California, Irvine

**Projects:** 1) Developed a detailed balance numerical model to calculate the maximum efficiency of Z-scheme water splitting mediated by a redox shuttle. 2) Developed a finite element model of the photocatalysis of simultaneous redox reactions on the surface of a semiconductor nanoparticle. 3) Designed a mass spectrometer system to measure the evolved gaseous products from electrode-free photocatalysis.

Sep. 2013 – Nov. 2016    *Ph.D. Student Researcher*, Law Group, University of California, Irvine

**Projects:** 1) Fabricated quantum dot solar cells and FETs and characterized them using electron microscopy, photoelectron spectroscopy, & X-ray diffraction. 2) Designed, built, and maintained a custom atomic layer deposition system. 3) Oversaw and maintained: RF sputter system, nitrogen gloveboxes, thermal evaporator, 4-point probe station, PL spectrometer, & solar simulator.

Jun. 2011 – Jun. 2013    *Assistant Research Specialist,* Beckman Laser Institute, Irvine, CA

**Projects:** 1) Assisted in the design and fabrication of diffuse optical spectroscopic medical devices. 2) Tested devices and performed experiments in the operating room. 3) Developed MATLAB scripts to automatically filter and correct noisy data.

Sep. 2010 – May 2011    *Team Leader, Senior Clinic Project,* Harvey Mudd College, Claremont, CA

**Project:** Led a year-long National Renewable Energy

Laboratory (NREL)-sponsored project to study and mitigate the effects of weathering on concentrated solar thermal plants.

## Education

Jul. 2013 – Nov. 2018      *Ph.D.* in Physics, University of California, Irvine. 2018

Sep. 2007 – May 2011      *B.S.* in Physics, Harvey Mudd College, Claremont, CA

## Teaching Experience

Winter 2018      *Teaching Assistant,* CHEM 1B: General Chemistry 2, Department of Chemistry, University of California, Irvine

Spring 2014      *Teaching Assistant,* PHYS 7E: Physics Lecture 3, Department of Physics, University of California, Irvine

Winter 2014      *Teaching Assistant,* PHYS 3LB: Physics Lab 2, Department of Physics, University of California, Irvine

Fall 2013      *Teaching Assistant,* PHYS 7LC: Physics Lab 1, Department of Physics, University of California, Irvine

## Awards

Apr. 2014      National Science Foundation Graduate Research Fellowship: Honorable Mention

Sep. 2013 – Sep. 2015      UC Irvine Chancellor's Graduate Student Fellowship

Sep. 2007 – May 2011      Harvey S. Mudd Merit Award

Sep. 2007 – May 2011      Dean's List, Harvey Mudd College

## Publications

1. **Keene, S.**, Ardo, S. "Detailed Balance Model of Light-Absorber Ensembles Performing Solar Fuels Reactions". 2018, In Preparation.
2. **Keene, S.**, Chandran, R. B., Ardo, S. "Calculations of Theoretical Efficiencies for Electrochemically-Mediated Tandem Solar Water Splitting as a Function of Bandgap Energies and Redox Shuttle Potential". *Energy and Environmental Science*, 2018, DOI: 10.1039/c8ee01828f
3. Patra, A. Chauhan, M. **Keene, S.** Gogoi, G. Anki R., Ardo, S., Prasad, D. Qureshi, M. "New Insights into the Synergistic Effects of Cerium Doping, Oxygen Vacancies, and Structural Distortions in Photocatalytic Hydrogen Production Efficiency of $BaZrO_{3-\delta}$

Hollow Nanospheres: A Combined Experimental and Theoretical Study". *Chemistry of Materials, 2018,* Submitted.

4. Yun, H. J., Lim, J., Fuhr, A., **Keene, S.**, Law, M., Pietryga, J. M., Klimov, V. I. "Charge Transport Mechanisms in CuInSe$_x$S$_{2-x}$ Quantum Dot Films". *ACS Nano*, 2018, Submitted.

5. Gogoi, G., **Keene, S.**, Patra, A. S., Sahu, T. K., Ardo, S., Qureshi, M. "Hybrid of g-C$_3$N$_4$ and MoS$_2$ Integrated onto Cd$_{0.5}$Zn$_{0.5}$S: Rational Design with Efficient Charge Transfer for Enhanced Photocatalytic Activity". *ACS Sustainable Chemical Engineering,* 2018, 6(5), 6718-6729

6. Cerussi, A. E. , Warren, R., Hill, B., Roblyer, D., Leproux, A., Durkin, A. F., O'Sullivan, T.D., **Keene, S.**, Haghany, H., Quang, T., Mantulin, W. M., Tromberg, B. J. "Tissue phantoms in multicenter clinical trials for diffuse optical technologies". *Biomedical Optics Express*, 2012, 3, 966.

## Proceedings and Posters

1. **Keene, S.**, Chandran, R. B., Gaieck, W., Zhang, A., Yaghoubi, H., Liu, J., Ardo, S. "Understanding Redox Shuttle Photocatalysis in Z-scheme Solar Water Splitting Reactors". *Gordon Research Conference on Solar Fuels*, 2018, Ventura, CA

2. **Keene, S.**, Cerussi, A. E. , Warren, R., Hill, B., Roblyer, D., Leproux, A., Durkin, A. F., O'Sullivan, T.D., Haghany, H., Quang, T., Mantulin, W. M., Tromberg, B. J. "Development of quality control and instrumentation performance metrics for diffuse optical spectroscopic imaging instruments in the multi-center clinical environment". *Proceedings of the SPIE: Optical Tomography and Spectroscopy of Tissue X*, 2013, San Francisco, CA

3. Nelson, A., **Keene, S.**, Diaz, J. M., Susca, E., Nazarian, D., Gonzales, E., Kennedy, C. "Understanding soil adhesion in Concentrating Solar Power plants: a novel analysis of soil characteristics". *Proceedings of the SolarPACES,* 2011, Granada, Spain

# ABSTRACT OF THE DISSERTATION

Detailed Balance Modeling of Novel Solar Fuels Designs

By

Samuel Thomas Keene

Doctor of Philosophy in Physics

University of California, Irvine, 2018

Professor Shane Ardo, Chair

Models of solar fuels devices that are completely electrochemically-mediated and consist of ensembles of optically thin light absorbers were used to calculate their maximum theoretical solar-to-fuel efficiencies. These models are based on the thermodynamic principles of detailed balance and blackbody radiation, semiconductor device physics, and simple catalysis. The maximum efficiency of an electrochemically-mediated tandem water splitting device was calculated and the crucial dependence of this efficiency on the redox shuttle thermodynamic potential was elucidated. A novel model of a stack of optically thin, radiatively coupled light-absorbers that each independently perform solar fuels reactions was developed to demonstrate the substantial gains in solar-to-fuel efficiency that are possible when using ensembles of small light-absorbers. The results presented herein can be used by researchers to develop high-efficiency, low-cost solar fuels materials and devices.

# Introduction

Limiting the extent of anthropogenic climate change is one of society's greatest challenges for the 21st century. It is projected that if greenhouse gas emissions are allowed to increase at their current rate, the global average surface temperature will increase by 4°C, the mean sea level will rise nearly one meter, and the oceans will acidify by 0.3 pH by the year 2100[1]. In order to avoid these catastrophic changes to Earth's climate, the primary energy share from renewable sources must more than double by 2030 and quadruple by 2050. Because wind and solar, the renewable sources for which there is the most generation capacity, are intermittent energy sources and because the current electric grid in the United States can only accommodate about 30% electricity generation from intermittent sources, such a rapid scale-up of renewable energy will require widespread energy storage[2]. Thus the development of a cheap, scalable technology to directly convert sunlight into storable fuel would be a monumental achievement.

One of the most well-researched solar fuels concepts over the last 50 years has been the use of photocatalysts to electrochemically drive fuel-forming reactions[3–8]. Specifically, the reaction by which water is electrochemically dissociated into hydrogen and oxygen (colloquially called water splitting) is promising because hydrogen is a storable fuel that can be used for both transportation and grid-scale energy storage[9–11]. The cathodic and anodic half-reactions required for water splitting in acidic conditions are, respectively,

$$2H^+ + 2e^- \rightarrow H_2 \tag{1}$$

$$H_2O \rightarrow 2H^+ + 2e^- + \frac{1}{2}O_2 \tag{2}$$

The free energy change under standard conditions to perform both half-reactions is 1.23 eV per electron and thus a substantial portion of the photons in the solar spectrum possess enough energy to excite electrons that can drive water splitting.

Photoelectrochemical water splitting was first demonstrated in 1972 by Fujishima and Honda by illuminating a $TiO_2$ crystal with UV light and using a platinum counter electrode[12,13]. This discovery was soon validated and the methods improved by other groups using materials such as $SrTiO_3$ perovskite, launching the field of modern solar water splitting[14–18]. Due to the overpotentials required to perform the hydrogen evolution reaction (HER) and particularly the oxygen evolution reaction (OER), the minimum required voltage for a device is around 1.6 – 1.7 V so in order to effectively utilize the solar spectrum, a tandem of light absorbers is required; much of the field has thus focused on a tandem approach. In the subsequent decades, semiconductor materials, catalysts, and device structures have been improved, leading to the development of devices that achieve over 10% solar to hydrogen (STH) efficiency[19–27]. The current world record for STH efficiency is over 30% using an approach that requires both a photoelectrochemical device and an electrolyzer[28]. There are several common elements between these most efficient demonstrations: all use tandems of monolithic light-absorbers either in direct electronic contact or electronically connected in a circuit, all evolve both gaseous products in the same container, and all except three[23,26,27] utilize III-V semiconductor light-absorbers and precious metal catalysts.

The costs associated with III-V materials, precious metals, gas separation, and mitigating the explosive hazard of mixed hydrogen and oxygen gas are technical and

economic barriers to plant-scale implementation of solar water splitting, despite the high efficiencies demonstrated[29,30]. New device schemes are required to achieve a system that is efficiency, cheap, and safe. One of the most promising designs is the Z-scheme particle suspension reactor, depicted schematically in Figure 1. In this design, two plastic containers with suspensions of photocatalyst particles in electrolyte solutions are stacked vertically (optically in series) and separated by membranes that allow electrolyte flow but prohibit particle flow. The electrolyte is a transparent redox shuttle; a chemical species that can easily and reversibly be changed between an oxidized and a reduced state. The particles in one container perform the OER and redox shuttle reduction while the particles in the other container perform the HER and redox shuttle oxidation. The two halves of the tandem are thus *electrochemically connected* via diffusion of the redox shuttle. Because the gases are evolved in separate containers, there is no risk of explosion and no cost associated with gas separation. Because the containers are vertically aligned, the redox shuttle can cycle between the two containers by diffusion alone without the need for external circulation mechanisms.
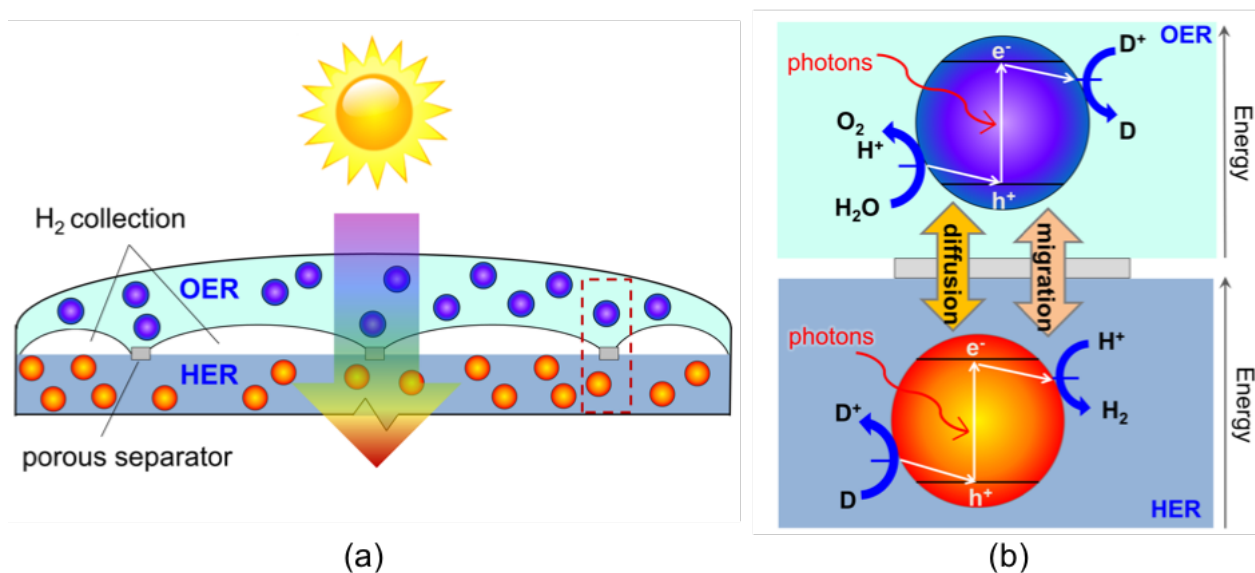
Figure 1. (a) Schematic of the Z-scheme vertically-stacked particle suspension reactor. (b) The desired chemistry and direction of electron transfer reactions, where D and $D^+$ are the reduced and oxidized redox shuttle species, respectively.

As long as inexpensive photocatalyst materials are used, the particle suspension reactor has the potential to be economically feasible for large-scale hydrogen production[29]. Recently our group developed a model that demonstrated the ability of a particle suspension reactor to operate indefinitely at 4% STH efficiency over day/night cycles[31].

Despite many experimental demonstrations of particle-based, electrochemically-connected water splitting[32–41], no system has been developed that achieves more than a 1% STH efficiency[42]. One of the major missing components in this field is a guiding theory that describes, using the most fundamental physics of the system, the dependence of the STH efficiency on the most basic parameters of the system such as light-absorber bandgaps, kinetic Tafel parameters, and particle size and optical properties. Although such theory is well-developed for water-splitting based on monolithic light-absorbers[43–51], there exist fundamental differences between these systems and Z-scheme particle suspension reactors

4

and related systems that have never been considered theoretically. Specifically, the difference between electronic and electrochemical connection in a tandem device changes the constraints upon the operating potential for both halves of the tandem. Additionally, the photon densities, overpotentials, and dark currents associated with generation of hydrogen or other solar fuels using an ensemble of independent small photocatalyst particles lie in a completely different regime compared to a monolithic photocatalyst.

In this thesis, I use the well-established principles of detailed balance and catalytic load-matching to develop novel models that describe the maximum STH efficiencies and STH efficiency dependence on fundamental parameters for systems relevant to Z-scheme particle suspension reactors. In Chapter 1, I describe the theoretical framework on which the models are based. In Chapter 2, I describe the model of efficiency limits of electrochemically-connected water splitting and present results which demonstrate a strong dependence of STH efficiency on the thermodynamic potential of the redox shuttle. In chapter 3, I describe the model of efficiency limits of ensembles of optically thin light-absorbers that individually perform net solar fuels reactions and present results which show the potential for drastic efficiency improvement given certain reasonable materials properties. The work presented herein can serve as a framework for future researchers to guide their materials and device development for high-efficiency, low cost, solar water splitting devices.

# 1. Theory

The monumental discoveries in quantum mechanics in the early twentieth century led to the development of the field of solid state physics and eventually the understanding and fabrication of the first practical solar cells at Bell labs in the early 1950s[52,53]. The promise of solar energy was recognized, and solar cells continued to be researched and developed. One of the most important publications in the theory of solar cells is the so-called "Shockley-Queisser Limit" in 1961 by William Shockley and Hans-Joachim Queisser in which the maximum theoretical efficiency of a p-n junction solar cell is derived using basic thermodynamics and idealized assumptions about the semiconductor properties[54]. This theory has been expanded, slightly corrected, and adapted to more complex photovoltaic systems[44,55–58]. A Shockley-Queisser type analysis of a solar energy device is one of the key first steps to guiding successful implementation, because it lays out the optimal value for one of the most basic material properties: the light-absorber's optical bandgap. For tandem devices, solar fuels devices, and devices with non-ideal properties such as substantial nonradiative recombination, it also serves as a sensitivity analysis for bandgap combinations, kinetic parameters, and parameters related to nonideality. The fundamental building blocks for this theory are described below. For an extended derivation and discussion, *Physics of Solar Cells: From Principles to New Concepts* by Peter Wurfel is an excellent resource[59].

## 1.1.    Blackbody Radiation

Consider some solar energy converting device in chemical and thermal equilibrium with its surroundings at a finite temperature $T$. A consequence of thermal equilibrium is that the device obeys detailed balance: the rates of any and all processes are exactly equal to the rates of their respective reverse processes. Because the device is capable of absorbing light and because its surroundings act as a thermal bath, both the device and the surroundings act as blackbodies and both exchange radiation with one another at equal rates. Specifically, Kirchhoff's law of thermal radiation requires that the rates of absorption and emission must be equal *at each photon energy and momentum*. We therefore seek a generalized expression for the photon density in an ideal blackbody $dn(hv)$ for photon energies between $hv$ and $dhv$ where $h$ is the Planck constant and is $v$ the photon frequency. This photon density is a product of the density of states $D(hv)$ and the probability of state occupation, or distribution function, $f(hv)$

$$dn(hv) = D(hv)f(hv)dhv \tag{1.1}$$

Because photons are bosons, their distribution function is the Bose-Einstein distribution

$$f(hv) = \frac{1}{\exp[(hv - \mu)/kT] - 1} \tag{1.2}$$

where $k$ is the Boltzmann constant and $\mu$ is the chemical potential of the photons which is zero for thermal radiation. We treat the blackbody as a box of arbitrary volume $V = L_x L_y L_z$ with allowed photon momenta following the well-known particle-in-a-box solution

$$p = \frac{h}{2}\sqrt{\left(\frac{n_x}{L_x}\right)^2 + \left(\frac{n_y}{L_y}\right)^2 + \left(\frac{n_z}{L_z}\right)^2} \qquad n_i \in \mathbb{Z} \tag{1.3}$$

Each state has volume $h^3/V$ in momentum space and there are two states per value of momentum corresponding to the two possible values of photon spin ($\pm 1$). The number of states with momentum between 0 and some arbitrary momentum $p$ is then the volume in momentum space of a sphere of radius $p$ divided by the volume per state times the number of states per momentum value. Using the dispersion relation for photons $h\nu = pc$ we convert this to the number of states $N_\gamma(h\nu)$ with energy between 0 and some arbitrary energy $h\nu$

$$N_\gamma(h\nu) = \frac{(8\pi/3)V(h\nu)^3}{(hc)^3} \tag{1.4}$$

Where $c = c_0/n$ is the velocity of light in the blackbody which depends on its index of refraction $n$. The density of states per unit volume per unit energy per solid angle is the change in number $\mathrm{d}N_\gamma$ per change in energy $\mathrm{d}h\nu$ divided by the volume divided by the integral over all solid angles $4\pi$

$$D_\Omega(h\nu) = \frac{1}{4\pi V} \times \frac{\mathrm{d}N_\gamma(h\nu)}{\mathrm{d}(h\nu)} = \frac{2(h\nu)^2}{(hc)^3} \tag{1.5}$$

We can now apply Equations 1.5 and 1.2 to Equation 1.1 to obtain Planck's law which describes the blackbody photon density per photon energy interval $\mathrm{d}h\nu$ per solid angle $\mathrm{d}\Omega$

$$\frac{\mathrm{d}n(h\nu)}{\mathrm{d}h\nu} = D_\Omega(h\nu)f(h\nu)\mathrm{d}\Omega = \frac{2(h\nu)^2\mathrm{d}\Omega}{(hc)^3}\frac{1}{\exp(h\nu/kT) - 1} \tag{1.6}$$

## 1.2.    Generation and Recombination

In order to convert photon energy to electric or electrochemical energy, a device must have a mechanism by which electric charge carriers are excited upon photon absorption. The rate at which this process occurs is called the generation rate $G$, while the rate at which

8

excited electric charges lose their energy via emission of a photon is called the radiative recombination rate $R$. When the device is in equilibrium, detailed balance requires that these rates $G_0$ and $R_0$ are equal for all photon energies. We can determine these equilibrium rates by calculating the rate at which blackbody radiation from the surroundings are absorbed. In order to do so, we must have some knowledge about how well the device absorbs light which in turn depends on the device's geometry and photon energy-dependent absorption coefficient $\alpha(h\nu)$. Here we make the simplifying assumption that the device is planar with thickness $d$. This allows us to define a single optical thickness $\tau(h\nu) = \alpha d$ and absorptance $a(h\nu) = 1 - \exp(-\alpha d)$. We also assume that each absorbed photon only produces a single excitation. The net equilibrium generation rate per unit area over the entire thickness of the device is the absorptance-weighted Planck's law integrated over all energies and solid angles

$$G_0 = R_0 = \oint \cos(\theta)\, d\Omega \int_0^\infty a(h\nu) \frac{2(h\nu)^2}{(hc)^3} \frac{1}{\exp\left(\frac{h\nu}{kT}\right) - 1}\, dh\nu \tag{1.7}$$

If the index of refraction of the device is larger than its surroundings, there exists an additional term that accounts for the angles for which photons are not exchanged between the two media due to Snell's law. Because we seek a general description, we assume there is no index mismatch that results in total internal reflection.

Up to this point we have not described the mechanism of charge carrier excitation in the solar device. The above derivation is extremely general and thus powerful. We will subsequently focus on generation and recombination processes in semiconductors, but much of the derivation applies with little or no modification to other systems. In a

semiconductor, the valence and conduction bands are separated by a bandgap energy $E_g$ and electrons(holes) can be excited into the conduction(valence) band by the absorption of photons. Similar to photons in a blackbody, we seek to describe the density of electrons in the conduction band $dn_e$ as a function of their energy $E_e$ in terms of a density of states $D_e(E_e)$ and a distribution function $f_e(E_e)$

$$dn_e(E_e) = D_e(E_e)f_e(E_e)dE_e \tag{1.8}$$

Electrons are fermions so their distribution function is the Fermi-Dirac distribution

$$f(E_e) = \frac{1}{\exp[(E_e - E_F)/kT] + 1} \tag{1.9}$$

Where $E_F$ is the Fermi energy. The allowed momenta for a gas of electrons in a volume $V$ is the same as the momenta for a gas of photons and is described by Equation 1.3. We can then write the number of states with momentum between 0 and some arbitrary momentum $p$ as the volume in momentum space of a sphere of radius $p$ divided by the volume per state times the number of states per momentum value which is two for the two allowed spin states ($\pm 1/2$)

$$N_e(|p|) = \frac{8\pi |p|^3 V}{3h^3} \tag{1.10}$$

Any electrons excited into the conduction band will quickly lose energy to the lattice and thermalize to the band edge, thus we can use the effective mass approximation for a quadratic dispersion relation[60-63]

$$E_e = E_C + \frac{p^2}{2m_e^*} \tag{1.11}$$

where $E_C$ is the conduction band energy. We obtain the density of states by converting Equation 1.10 to energy using Equation 1.11, differentiating with respect to energy and dividing by the volume

$$D_e(E_e) = \frac{1}{V}\frac{dN_e(E_e)}{dE_e} = 4\pi\left(\frac{2h^2}{m_e^*}\right)^{3/2}(E_e - E_C)^{1/2} \tag{1.12}$$

we now have a full expression for the electron density $dn_e(E_e)$ which we can integrate over all energies to obtain the total number of electrons in the conduction band per unit volume

$$n_e = \int_{E_C}^{\infty} D_e(E_e)f_e(E_e)dE_e \tag{1.13}$$

Although Equation 1.12 is valid only for energies close to the conduction band, the distribution function $f_e(E_e)$ vanishes for high energies so the integral is valid. Furthermore, as long as $E_e < E_f - 3kT$, the Fermi-Dirac distribution can be approximated as a Boltzmann distribution which simplifies the integral

$$f(E_e) = \exp[-(E_e - E_F)/kT] \tag{1.14}$$

The above approximations are generally valid at room temperature for nondegenerate semiconductors with bandgaps above 200 mV[55,56,59,62]. They allow us to analytically evaluate Equation 1.13 and calculate the total density of electrons in the conduction band

$$n_e^0 = N_C \exp\left[-\frac{(E_C - E_F)}{kT}\right] \tag{1.15}$$

with

$$N_C = 2\left(\frac{2\pi m_e^* kT}{h^2}\right)^{3/2} \tag{1.16}$$

An identical analysis can be done for the density of holes in the valence band $n_h$

$$n_h^0 = N_V \exp\left[-\frac{(E_F - E_V)}{kT}\right] \tag{1.15}$$

with

$$N_V = 2\left(\frac{2\pi m_h^* kT}{h^2}\right)^{3/2} \tag{1.16}$$

where $E_V$ is the valence band energy and $m_h^*$ is the effective mass of holes. We have used to superscript "0" to indicate that these are the carrier densities in the equilibrium, unilluminated case. We can relate $n_e^0$ and $n_h^0$ to the intrinsic density $n_i$ by

$$n_e^0 n_h^0 = {n_i}^2 = N_C N_V \exp\left(-\frac{E_g}{kT}\right) \tag{1.17}$$

When the semiconductor is illuminated, additional electrons and holes are excited and the density of electrons(holes) in the conduction(valence) band increases. We have also assumed that they instantaneously interact and establish thermal equilibrium with the lattice. The only way this is possible is if there is a new Fermi energy for the distribution of excited electrons and excited holes. We define these "quasi-Fermi energies" $E_{FC}$ and $E_{FV}$ for electrons in the conduction band and holes in the valence band, respectively. Under illumination, the changes in carrier concentration in the two bands dictate that $E_{FC}$ is higher than $E_F$ and $E_{FV}$ is lower than $E_F$. The new carrier densities are

$$n_e = N_C \exp\left[-\frac{(E_C - E_{FC})}{kT}\right] \tag{1.18}$$

$$n_h = N_V \exp\left[-\frac{(E_{FV} - E_V)}{kT}\right] \tag{1.19}$$

which we can relate to the product of carrier densities in the unilluminated case from Equation 1.17

$$n_e n_h = n_i^2 \exp\left(\frac{E_{FC} - E_{FV}}{kT}\right) = n_e^0 n_h^0 \exp\left(\frac{E_{FC} - E_{FV}}{kT}\right) \tag{1.20}$$

Radiative recombination involves one electron and one hole, so the general rate law is

$$R_e = R_h = B n_e n_h \tag{1.21}$$

Where $B$ is some constant. We know the value of $R_e^0 = R_h^0 = G_0$ from Equation 1.7 and we know the relationship between $n_e n_h$ and $n_e^0 n_h^0$ from Equation 1.20 which allows us to determine the recombination rate as a function of quasi-Fermi level splitting

$$R_e = R_h = G_0 \exp\left(\frac{E_{FC} - E_{FV}}{kT}\right) \tag{1.22}$$

$E_{FC} - E_{FV}$ is the total change in chemical potential in the semiconductor. If we assume that the semiconductor is in a device configuration where all excited carriers that do not recombine are extracted as electric current, then this change in chemical potential is equal to the available electric potential energy $qV$ where $q$ is the fundamental charge and $V$ is the electric potential. Practically this assumption requires a device configuration such as a p-n junction or selective contacts that both separates and extracts electrons and holes without energy losses. Defining an incident solar photon flux $\Phi_0(h\nu)$ we can now define the current density $j$ through the device as the sum of the generation rate due to solar absorption, the generation rate due to blackbody absorption, and the radiative recombination rate

$$j = q \int_0^\infty a(h\nu) \Phi_0(h\nu) \mathrm{d}h\nu + qG_0 \left(1 - \exp\left[\frac{qV}{kT}\right]\right) \tag{1.23}$$

Note that although the lower bound of the integral is zero, the above description of the semiconductor requires that $a(h\nu) = 0$ for $a(h\nu) < E_g$. Equation 1.23 is the Shockley diode equation[52]. This equation only considers radiative recombination and neglects other forms such as Auger or Shockley-Read-Hall recombination. A rate law such as the one in Equation

1.21 can be defined for these processes, but the rate dependence on quasi-Fermi level splitting analogous to Equation 1.22 is more difficult to derive and depends on the specific system of interest. The most basic way to accommodate nonradiative recombination is to assume that is has the same rate dependence on quasi-Fermi level splitting as radiative recombination and that there is a known equilibrium fraction of recombination that is radiative $f_c$[54]. This tells us that for every radiative recombination event, there are $1/f_c - 1$ nonradiative recombination events. Then by detailed balance the contribution to the current density from nonradiative recombination is

$$j_{NR} = \left(\frac{1}{f_c} - 1\right) q G_0 \left(1 - \exp\left[\frac{qV}{kT}\right]\right) \tag{1.24}$$

Equation 1.24 is then added to Equation 1.23 to obtain the complete $j$-$V$ relationship.

## 1.3.   Electrocatalysis, Load Matching, and Efficiency

In a photovoltaic device, electric current $j$ is extracted in an external circuit with electric potential $V$ across the device. A load is applied to the circuit such that the power supplied by the device is maximized and the power conversion efficiency (PCE) is defined as

$$\eta_{PCE} = \frac{\max (j \times V)}{I_0} \tag{1.25}$$

Where $I_0$ is the total solar irradiance

$$I_0 = \int_0^\infty h\nu \times \Phi_0(h\nu) \mathrm{d}h\nu \tag{1.26}$$

Kirchhoff's current law is obeyed in the photovoltaic device simply because the current entering one terminal is equal to the current exiting the other terminal. When a device is used to drive redox chemistry, Kirchhoff's law is obeyed as long as the device drives a

cathodic reaction and an anodic reaction at the same rate. This is essentially the same as the photovoltaic case with a slightly different sign convention: $j$ is the flux of negative charge entering one end of the device via the anodic reaction and $-j$ is the flux of positive charge entering the other end of the device via the cathodic reaction, where the anodic reaction is defined to be the reaction with the higher reduction potential. This sign convention ensures that $j$ has a positive value for the fuel-forming reaction. The kinetics of the two half-reactions are described by the Butler-Volmer equation

$$j = j_0^{ox} \left( \exp\left( \frac{\alpha_a^{ox} \eta_{ox} q}{kT} \right) - \exp\left( -\frac{\alpha_c^{ox} \eta_{ox} q}{kT} \right) \right) \tag{1.27}$$

$$-j = j_0^{red} \left( \exp\left( \frac{\alpha_a^{red} \eta_{red} q}{kT} \right) - \exp\left( -\frac{\alpha_c^{red} \eta_{red} q}{kT} \right) \right) \tag{1.28}$$

The scripts "ox" and "red" refer to the net oxidative (anodic) and net reductive (cathodic) reactions, the $j_0^i$ terms are the exchange current densities, the $\eta_i$ terms are the overpotentials, and the $\alpha_a^i$ and $\alpha_c^i$ terms are the anodic and cathodic charge transfer coefficients. Neglecting concentration overpotentials, the potential across the device is the sum of the standard thermodynamic potential of the complete reaction $E^0$ and the kinetic overpotentials

$$V = E^0 + \eta_{ox} - \eta_{red} \tag{1.29}$$

Equation 1.29 provides the coupling between Equations 1.23, 1.27, and 1.28. Unlike the case of the photovoltaic device, where the operating $j$-$V$ point in Equation 1.23 was selected to optimize $j \times V$, there is only one $j$-$V$ point that solves all four equations. The solar-to-fuel (STF) efficiency, or specifically for water splitting the solar-to-hydrogen (STH) efficiency, is

the ratio of power generated to incident solar power. Because the potential energy of each

fuel molecule is fixed by $E^0$, the STF efficiency only depends on the current density

$$\eta_{\text{STF}} = \frac{j \times E^0}{I_0} \tag{1.30}$$

The models in the following chapters are based upon the relationships derived above.

# 2. Calculations of Theoretical Efficiencies for Electrochemically-Mediated Tandem Solar Water Splitting

Tandem Z-scheme solar water splitting devices comprised of two light-absorbers that are connected electrochemically by a soluble redox shuttle constitute a promising technology for cost-effective solar hydrogen production. Herein, efficiency limits of these devices are modeled by combining the detailed-balance model of the light-absorbers with Butler–Volmer electron-transfer kinetics. The impacts of the redox shuttle thermodynamic potential, light-absorber bandgaps, and electrocatalytic parameters on the solar-to-hydrogen conversion (STH) efficiency are modeled. We report that the thermodynamic potential of the redox shuttle with respect to the hydrogen and oxygen evolution potentials has a direct effect on both the STH efficiency and the optimal tandem light-absorber bandgaps needed to achieve the maximum possible STH efficiency. At 1 Sun illumination and assuming ideal and optimally selective electrocatalytic parameters, the STH efficiency varies from a minimum of 21%, for a redox shuttle potential of 0 V *vs.* RHE, to a maximum of 34%, for a redox shuttle potential of either 0.36 V or 1.06 V *vs.* RHE. To attain the maximum possible STH efficiency of 34%, the light-absorber bandgaps must be 1.53 eV and 0.75 eV, yet the optimal redox shuttle potential depends on whether the hydrogen-evolving

or oxygen-evolving light-absorber has the larger bandgap. Results also underscore the importance of optimizing the absorptance of the top light-absorber, which enables large STH efficiencies to be achieved with a wider range of bandgap combinations. Moreover, given the large overpotentials for the oxygen evolution reaction and reasonably low overpotentials for most redox shuttle reactions, the tandem design is more efficient than a single light-absorber design even when the potential of the redox shuttle exceeds 1.23 V *vs.* RHE. When the exchange current density of the redox shuttle reactions is as low as $10^{-5}$ mA/cm$^2$, STH efficiencies as large as 22% are still achievable as long as optimal selective catalysis is assumed, suggesting that even slow redox shuttle reactions may not limit the practicality of these devices.

## 2.1. Motivation

The process of solar water splitting provides renewable and storable energy in the chemical bonds of hydrogen and oxygen gas. This process is initiated through sunlight absorption by at least one light-absorber, which for the purpose of this work is a material that absorbs light and generates mobile charge carriers that ultimately participate in water electrolysis redox reactions either with or without co-catalysts. The photovoltage required to effectively drive water electrolysis at 25 °C under standard-state conditions is the sum of the thermodynamic potential difference between the two half reactions (1.23 V), overpotentials, and resistive losses,[64] which based on state-of-the-art light-absorbers equals at least 1.6 V. In order to provide this photovoltage with a single light-absorber its bandgap must exceed ~1.9 eV. However, this is inefficient, because a ~1.9 eV bandgap light-absorber is not optimum for maximum power-conversion efficiency, which instead

occurs for a single light-absorber with a bandgap of 1.1 – 1.4 eV.[54] A common solution to this energetic discrepancy is to use two or more light-absorbers in tandem, i.e. optically in series, that together generate the required photovoltage. In the vast majority of demonstrations of tandem solar water electrolysis, the light-absorbers are connected *electronically* in series (Figure 2.1a).[8] Under illumination, electrons in one light-absorber reduce protons, or water, to hydrogen via the hydrogen evolution reaction (HER) while holes at the other light-absorber oxidize water, or hydroxide, to oxygen via the oxygen evolution reaction (OER). The other electronic charge carriers recombine at low-resistance contacts to maintain charge balance. These electronically-connected tandem devices are often challenging to fabricate as they typically require high-quality metallurgical junctions,[28] and they have been described and modeled extensively in the literature.[43–51,65]

Another approach to tandem solar water electrolysis replaces electronic connection(s) between the light-absorbers with *electrochemical* connection(s) (Figure 2.1b). These electrochemically-connected tandem devices use redox shuttles (denoted by A/A$^-$ in Figure 2.1b) that are oxidized by holes from the $H_2$-evolving light-absorber and that are reduced by electrons from the $O_2$-evolving light-absorber. An example of an electrochemically-connected tandem device is the redox-shuttle-mediated Z-scheme particle suspension reactor for solar water electrolysis, which facilitates $H_2$ evolution and $O_2$ evolution in separate compartments and does not require the use of an ion-selective membrane, like Nafion.[42,50,66–68] This design, depicted in Figure 2.1b, maximizes light-absorption by stacking the compartments optically in series, and by evolving $H_2$ and $O_2$ in separate compartments avoids explosive hazards. As a result, techno-economic projections

suggest that Z-scheme particle suspension reactors for plant-scale production of $H_2$ are a scalable technology that can be cost-competitive with $H_2$ generated by steam methane reforming,[31,42,66,69–71] provided that photocatalyst materials, redox shuttles, and additional reactor components are discovered that are efficient, durable, and inexpensive.[29,72]



**a**

$4H^+ + 4e^- \rightarrow 2H_2$

Light-absorber 1

Light-absorber 2

$2H_2O + 4h^+ \rightarrow 4H^+ + O_2$

**b**

$4A^- + 4h^+ \rightarrow 4A$   $4H^+ + 4e^- \rightarrow 2H_2$

Light-absorber 1

$A/A^-$ transport

Light-absorber 2

$4A + 4e^- \rightarrow 4A^-$   $2H_2O + 4h^+ \rightarrow 4H^+ + O_2$
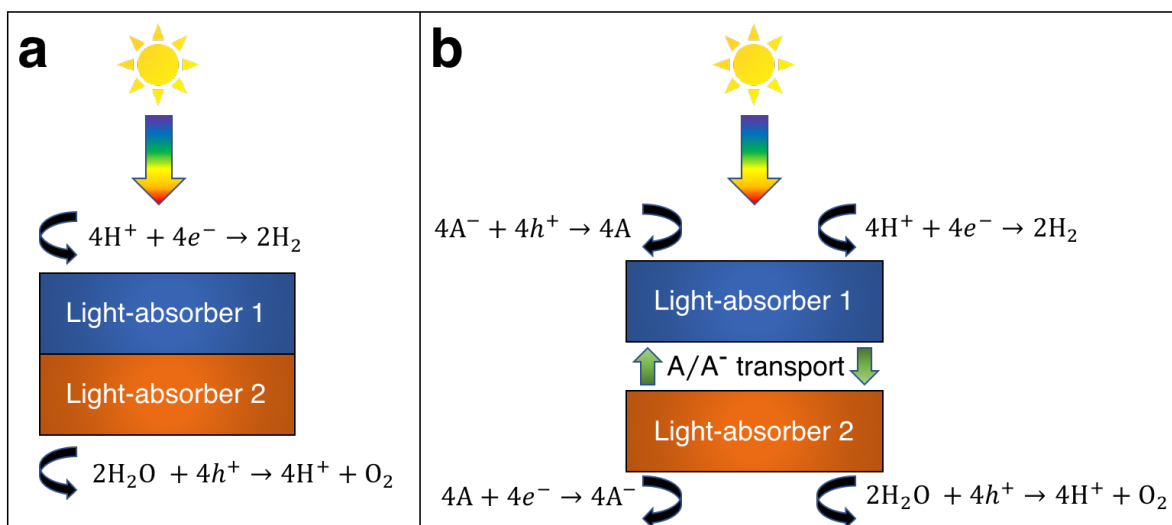
Figure 2.1. An exemplary design for solar water electrolysis in an acidic environment and based on (a) *electronically*-connected tandem devices and (b) *electrochemically*-connected tandem devices. Electronically-connected tandem devices utilize two catalytically active light-absorbers that are electrically and optically in series, while light-absorbers in electrochemically-connected tandem devices are electronically isolated and instead charge transfer is mediated by a soluble redox shuttle.

However, there are still challenges for this concept, because experimental demonstrations of electrochemically-connected tandem devices for solar water electrolysis often exhibit < 1% STH efficiency,[42] as compared to the large number of demonstrations with > 10% STH efficiency for the electronically-connected tandem devices.[8,28] Recently, our group developed transport and kinetic models for Z-scheme particle suspension reactors that established that passive diffusive species transport with $IO_3^-/I^-$ and quinone/hydroquinone ($Q/QH_2$) redox shuttles can sustain up to a 4% solar-to-hydrogen

conversion (STH) efficiency in centimeter-tall reactors.[31] In that work, we identified optimal reactor designs and operating conditions by investigating the impacts of light absorption, species transport, and electrokinetics for a few commonly investigated semiconductor materials ($TiO_2$, $BiVO_4$ and Rh-doped $SrTiO_3$) and plausible redox shuttles ($Fe^{3+}/Fe^{2+}$, $IO_3^-/I^-$, $Q/QH_2$). That work did not optimize the STH efficiency for the bandgap combinations of the photocatalysts or the redox shuttle potentials of the electrolyte, in part because of the complexity of the model, which had many adjustable parameters.

Evaluation of theoretical limiting efficiencies for solar energy conversion processes as a function of the bandgap of the light-absorbers is a critical step toward identifying the primary factors that influence device performance. While numerous studies have reported the Shockley–Queisser detailed-balance efficiency limits for solar water electrolysis using *electronically*-connected tandem devices,[43–47,50] such predictions are not available for *electrochemically*-connected tandem devices. To establish theoretical STH efficiency limits and design requirements for redox-shuttle-mediated electrochemically-connected tandem devices for solar water electrolysis, herein we present a comprehensive numerical analysis as a function of light-absorber bandgaps, redox shuttle potential, and redox shuttle electrocatalytic parameters. Notably, we found that the thermodynamic potential of the redox shuttle and the light-absorber bandgaps each influence the maximum possible STH efficiency. The resulting optimal bandgap combinations differ from combinations previously deduced from models of electronically-connected tandem designs, which further supports the merit in this work. We also determine that the range of redox shuttle potentials for the electrochemically-connected tandem design to outperform the

performance of a single light-absorber depends on the exchange current densities modeled for the redox shuttle.

## 2.2.    Numerical Model

Models for electronically-connected tandem devices for solar water electrolysis that are positioned optically and electronically in series (Figure 2.1a) are well known.[43,45–47,50] Electrochemically-connected devices (Figure 2.1Figure 2.1b) are more complex due to additional constraints imposed by electrochemical reactions with the redox shuttle. Therefore, equations for the electronically-connected tandem devices are presented first, followed by several modifications required to describe the electrochemically-connected tandem devices. For the electronically-connected devices, *the sum of the photovoltages generated by the light-absorbers must exceed the electrochemical load*, which is defined as the difference of the thermodynamic reaction potentials plus the overpotentials as follows,

$$V_{\text{top}} + V_{\text{bottom}} = (E_{\text{OER}} - E_{\text{HER}}) + (\eta_{\text{OER}} - \eta_{\text{HER}}) \tag{2.1}$$

where, $V_{\text{top}}$ and $V_{\text{bottom}}$ are the operating potentials of the top and bottom light-absorber, respectively, $E_{\text{OER}}$ and $E_{\text{HER}}$ are the thermodynamic potentials for the OER and the HER, respectively, and whose difference is the thermodynamic minimum electrochemical load and equals the potential to electrolyze water, and $\eta_{\text{OER}}$ and $\eta_{\text{HER}}$ are the electrocatalytic overpotentials for the OER and the HER, respectively. Because there is only one electrochemical load, the physical locations of the light-absorbers that drive the OER and the HER in the top or bottom positions do not affect the values obtained using Equation 2.1, and therefore, the positions of these reactions are interchangeable.

For the electrochemically-connected tandem devices charge is mediated between the two light-absorbers by a soluble redox shuttle, A/A⁻ (Figure 2.1b). In these devices, *the photovoltage generated by each light-absorber must exceed the electrochemical load for its associated oxidation and reduction half-reactions* as follows,

$$V_{\text{bottom/top}} = (E_{\text{OER}} - E_{\text{shuttle}}) + (\eta_{\text{OER}} - \eta_{\text{shuttle,red}}) \tag{2.2}$$

$$V_{\text{top/bottom}} = (E_{\text{shuttle}} - E_{\text{HER}}) + (\eta_{\text{shuttle,ox}} - \eta_{\text{HER}}) \tag{2.3}$$

where $E_{\text{shuttle}}$ is the thermodynamic potential of the redox shuttle oxidation/reduction reaction, the differences $(E_{\text{shuttle}} - E_{\text{HER}})$ and $(E_{\text{OER}} - E_{\text{shuttle}})$ are the thermodynamic minimum electrochemical loads for the reactions taking place at each light-absorber, and $\eta_{\text{shuttle,ox}}$ and $\eta_{\text{shuttle,red}}$ are the electrocatalytic overpotentials for oxidation and reduction of the redox shuttle, respectively. The operating electrochemical loads are thus the full sums described on the right-hand sides of Equations 2.2 and 2.3, and 2.1 (Figure 2.2). To maximize the STH efficiency, the larger electrochemical load is driven by the light-absorber with the larger bandgap and that light-absorber is located spatially at the top of the reactor, while the smaller electrochemical load is driven by the light-absorber with the smaller bandgap and that light-absorber is located spatially at the bottom of the reactor. Because each electrochemical load depends on the thermodynamic potential of the redox shuttle, the choice of redox shuttle dictates whether the OER or the HER should occur in the top or bottom compartment of the device. In our numerical model, we only considered arrangements that produced the optimal STH efficiency.
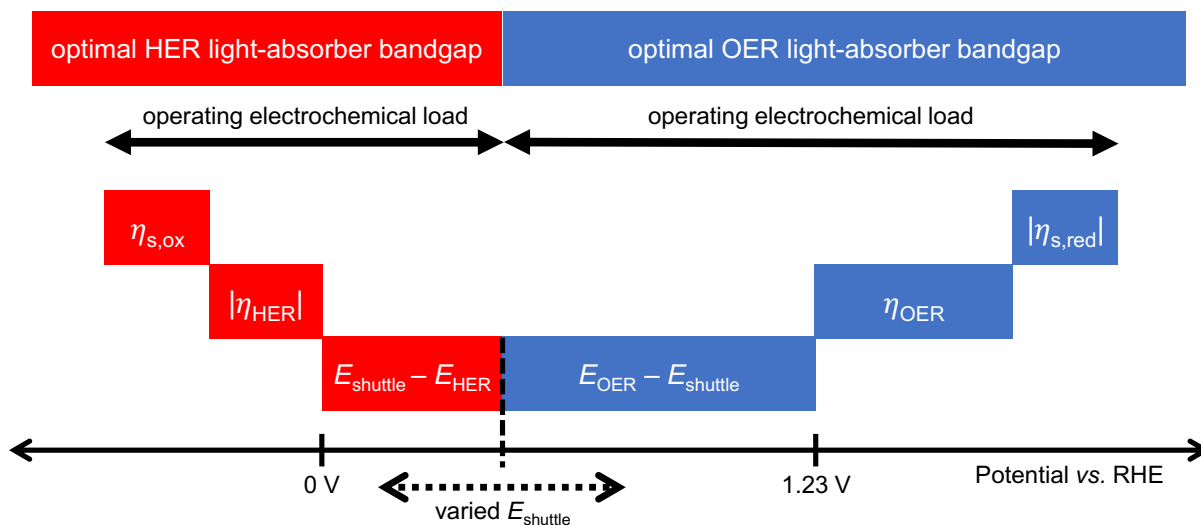
Figure 2.2. A visual representation of the terms that dictate the operating electrochemical load for each light-absorber and the optimal light-absorber bandgaps under the detailed-balance limit.

All model calculations were performed using MATLAB 2017b and numeric solutions to coupled equations were found using the vpasolve function. Several assumptions are made in the model including a standard temperature of 300 K, unity activity for gases such that $(E_{OER} - E_{HER})$ = 1.23 V, unity activity for redox shuttle species that each react by an outer-sphere single-electron transfer mechanism, no parasitic light absorption by the redox shuttle species, no ohmic resistance/ion migration losses, and no concentration overpotentials due to species concentration gradients from finite rates of mass transport. Additionally, we assume that the device configuration and selection of light-absorbers and any additional co-catalysts are such that the band edges at the active surfaces straddle the appropriate redox potentials as required for device operation. This means that for each light-absorber, the potential of the valence-band edge is larger than the corresponding potential of the oxidation reaction and the potential of the conduction band edge is smaller than the corresponding potential of the reduction reaction.

24

Each light-absorber is modeled as an ideal photodiode via the typical areal current-density *vs.* voltage (*j–V*) relationship[50,51,73,74],

$$j = j_{ph} + j_{th}\left(1 - e^{\frac{qV}{k_B T}}\right) \tag{2.4}$$

$$j_{ph} = Aq \int_{E_g/h}^{\infty} n(v)\,dv \tag{2.5}$$

$$j_{th} = \frac{2\pi Aq}{c^2} \int_{E_g/h}^{\infty} v^2 e^{\frac{hv}{k_B T}}\,dv \tag{2.6}$$

where $j_{ph}$ is the current density due to the absorbed solar photon flux, $j_{th}$ is the current density due to radiative recombination assuming the device is a blackbody at 300 K and emits into vacuum from two parallel flat surfaces,[54] $q$ is the fundamental charge, $k_B$ is the Boltzmann constant, $T$ is the temperature of the device and is assumed to be 300 K, $A$ is the non-dimensional, frequency-independent absorptance, which is the fraction of light absorbed/emitted by the light-absorber and ranges from 0 to 1, $E_g$ is the energy of the bandgap of the light-absorber, $h$ is the Planck constant, $v$ is the photon frequency, $n$ is the frequency-dependent incident photon flux, and $c$ is the speed of light in vacuum. Excited-state charge carriers are assumed to rapidly thermalize to the band edges, such that each absorbed photon produces only one e⁻/h⁺ pair. The refractive index of the light-absorber is assumed to be equal to 1 so that the analysis is general for a wide range of light-absorber bandgaps.[54,57] For the top light-absorber, $n(v)$ is the solar photon flux, while for the bottom light-absorber, $n(v)$ is the net photon flux transmitted through the top light-absorber, i.e. the solar photon flux minus the photon flux absorbed by the top light-absorber.

The frequency-independent absorptance ($A$) is included in Equation 2.5 to consider partial absorption of above-bandgap photons by the top light-absorber, and therefore, partial transmission of the incident photons to the bottom light-absorber. Likewise, Equation 2.6 guarantees that the rate of radiative recombination equals the rate of blackbody photon absorption at thermal radiative equilibrium, as mandated by the principle of detailed balance.[54,57] The benefit of partial absorption of above-bandgap light is that with appropriately chosen absorptance values, a larger range of bandgap combinations results in large STH efficiencies, as shown previously for electronically-connected tandem devices.[47,75] Absorptance/emittance is typically a frequency-dependent quantity that depends on the optical absorption coefficient of the light-absorber and the pathlength that light travels within the light-absorber.[76] This is strictly true, given our model assumption of no absorption by the electrolyte. In electronically-connected tandem devices, the absorptance/emittance can be varied by altering the thickness of the hundreds-of-nanometers to hundreds-of-microns thick light-absorber and/or by altering its frequency-dependent absorption coefficient. In electrochemically-connected tandem particle suspension reactors, the absorptance/emittance can be varied through facile variations in the height of the suspension-filled reactor, the particle concentration, the particle size, or more challenging, the frequency-dependent absorption coefficient of the light-absorber.[31] Because these facile variations are most likely to be incorporated in actual reactors and they result in frequency-independent variations in $A$, we incorporated frequency-independent values for the absorptance/emittance in the model.

For most cases, $A$ is set equal to one for all photons with energy larger than the light-absorber bandgap. However, when the absorbed photon flux by the bottom light-absorber limits the overall operating current density of the tandem device, $A_{\text{top}}$ is allowed to vary between 0 and 1 to enforce current-matching between the top and bottom light-absorbers, by a process that we term *absorptance optimization*. Absorptance optimization is not useful for the bottom light-absorber, because there is no benefit in transmitting photons through the bottom light-absorber. Moreover, when the overall operating current density of the tandem device is limited by the absorbed photon flux by the top light-absorber, absorptance optimization is also not useful, and in this case, the largest STH efficiency occurs when $A_{\text{top}}$ = 1 and no photons whose energy is larger than the bandgap of the top light-absorber can be absorbed by the bottom light-absorber.

The electrocatalytic behavior of the two coupled redox reactions that occur at each light-absorber surface are modeled by the Butler–Volmer equation,

$$j = j_0^{\text{ox}} \left( \exp\left( \frac{\alpha_a^{\text{ox}} \eta_{\text{ox}} q}{kT} \right) - \exp\left( -\frac{\alpha_c^{\text{ox}} \eta_{\text{ox}} q}{kT} \right) \right) \tag{2.7}$$

$$-j = j_0^{\text{red}} \left( \exp\left( \frac{\alpha_a^{\text{red}} \eta_{\text{red}} q}{kT} \right) - \exp\left( -\frac{\alpha_c^{\text{red}} \eta_{\text{red}} q}{kT} \right) \right) \tag{2.8}$$

where $j_0$ are the exchange current densities, $\alpha_a$ and $\alpha_c$ are the anodic and cathodic charge transfer coefficients, respectively, $\eta$ are the overpotentials, and the indices *ox* and *red* refer to the net oxidation and net reduction reactions, respectively, on each light-absorber. For instance, on the hydrogen evolving light-absorber, the HER is the reduction reaction while oxidation of the redox shuttle is the oxidation reaction. The negative sign in Equation 2.8 ensures that the current densities associated with the oxidation and reduction half-

reactions are equal. This satisfies Kirchhoff's current law such that no charge builds up on any light-absorber. This operating current density, $j$, is the same $j$ that appears on the left-hand-side of Equation 2.4.

Experimentally-measured kinetic parameters for state-of-the-art RuO$_2$ OER electrocatalysts and state-of-the-art Pt HER electrocatalysts,[50,77,78] which were used in previous models of electronically-connected tandem devices,[10] are incorporated herein for conditions of net production of O$_2$ and H$_2$, respectively, but with optimal selectivity such that $\alpha$ for the undesired reactions are set equal to zero ($j_{0,HER} = 0.147$ mA/cm$^2$; $j_{0,OER} = 3.26$ x 10$^{-6}$ mA/cm$^2$; $\alpha_{a,HER} = 0$; $\alpha_{c,HER} = 1.97$; $\alpha_{a,OER} = 1.60$; $\alpha_{c,OER} = 0$). While convenient, the assumption of optimal selectivity for OER and HER electrocatalysis are inconsequential to the outcomes of the simulations; when perfectly symmetric non-selective electrocatalytic behavior is simulated using $\alpha_{a,HER} = \alpha_{c,HER} = 1.97$ and $\alpha_{c,OER} = \alpha_{a,OER} = 1.60$, the maximum calculated STH efficiency changed by < 0.15 % from the value obtained for the case of optimal selectivity (33.92% *vs.* 33.96%). Kinetic parameters for the redox shuttle reactions were chosen so that the reactions were modeled as being rapid, which was implemented by setting the exchange current density to an arbitrarily chosen large value such that the overpotentials were effectively equal to zero. In addition, all redox shuttle reactions were assumed to have optimal selectivity, which was implemented by setting the charge-transfer coefficients for the desired redox shuttle reactions to one and the charge-transfer coefficients for the undesired reactions to zero. We term this selectivity optimal, because it simulates the Butler–Volmer electrokinetic condition where at the HER light-absorbers only the rate of oxidation of the redox shuttle increases with increased bias voltage, and at

28

the OER light-absorbers only the rate of reduction of the redox shuttle increases with increased bias voltage. The significance of selective, asymmetric redox shuttle electrocatalysis and optimal redox shuttle kinetic parameters were discussed in our prior work.[31]

The relationship between the operating voltage and the overpotentials are described by Equations 2.2 and 2.3 for the light-absorbers that perform the OER and the HER, respectively. In the absence of absorptance optimization, $A_{\text{top}}$ is set to one and Equations 2.2 or 2.3 and 2.4, 2.7, and 2.8 are numerically solved for each light-absorber to obtain the operating current density and voltage. To enforce current-matching, the smaller of the two current densities is selected as the overall operating current density. When absorptance optimization is used, Equations 2.2 and 2.3, and two versions of Equations 2.4, 2.7, and 2.8, one of each for each light-absorber, are simultaneously solved under the constraint of current-matching, i.e. $j_{top} = j_{bottom}$, and with $A_{\text{top}}$ as a free parameter. Other designs can also be modeled using similar procedures. In the model of an electronically-connected tandem device, Equations 2.1, 2.7, and 2.8, and two versions of Equation 2.4, one for each light-absorber, are simultaneously solved to obtain the overall operating current density. For the single light-absorber design, Equations 2.1, 2.7, and 2.8, and one version of Equation 4 are simultaneously solved to obtain the overall operating current density. For a side-by-side electrochemically-connected tandem design, where the light-absorbers are positioned optically in parallel, Equations 2.2 or 2.3, and 2.4, 2.7, and 2.8, are solved for each light-absorber. In this case, $n(v)$ for each light-absorber is set equal to the solar photon flux and $A$ is set equal to one, but the current density of each light-absorber is

multiplied by the fraction of the area it occupies out of the total area of the tandem design. In the base case, this fraction is set equal to one half (0.5) for both light-absorbers and the smaller of the two current densities is selected as the overall operating current density to enforce current matching. In the optimized case, the fractions are allowed to vary between 0 and 1 (under the restriction that the two fractions sum to 1) and Equations 2.2 and 2.3, and two versions of Equations 2.4, 2.7, and 2.8, one of each for each light-absorber, are simultaneously solved under the constraint of current-matching.

The ultimate performance metric is the STH efficiency,

$$\eta_{STH} = \frac{j \times E^0_{O_2/H_2O}}{I_{AM,1.5}} \tag{2.9}$$

where $I_{AM,1.5}$ is the frequency-integrated AM 1.5 solar irradiance. The value of $\eta_{STH}$ is evaluated over a range of tandem light-absorber bandgaps (0.2 eV to 3.0 eV in steps of 0.01 eV), redox shuttle potentials (–0.2 V to +1.5 V in steps of 0.01 eV), and the electrocatalytic parameters. The only parameter in Equation 2.9 that is variable is $j$, and thus the STH efficiency is completely determined by the matched operating current of the two light-absorbers.

## 2.3.    Results and Discussion

Figure 2.3 presents STH efficiencies for the electronically-connected and electrochemically-connected tandem devices as a function of the light-absorber bandgaps. For the electronically-connected devices (Figure 2.3a) the predicted maximum STH efficiency is 34%, which occurs for light-absorber bandgaps of 1.53 eV and 0.75 eV. This STH efficiency is slightly larger than the value of 30% obtained by Hu, et al.,[50] because of additional

solution resistance terms that were included in their work. Figure 2.3b and 2.3c depict the STH efficiencies for electrochemically-connected tandem designs for the specific cases of $E_{shuttle}$ = 0.36 V and $E_{shuttle}$ = 1.06 V, redox shuttle potentials that lead to maximum STH efficiencies equal to that of the electronically-connected devices.

For $E_{shuttle}$ = 0.36 V *vs.* RHE (Figure 2.3b), the minimum electrochemical load for the light-absorber driving the HER and redox shuttle oxidation (labeled as HER light-absorber) is 0.36 V (0.36 V – 0 V), whereas the minimum electrochemical load for the light-absorber driving the redox shuttle reduction and the OER (labeled as OER light-absorber) is 0.8 V (1.23 V – 0.36 V). In an optimal configuration the OER light-absorber has the larger bandgap and generates the larger photovoltage and is thus positioned on top of the HER light-absorber. For $E_{shuttle}$ = 1.06 V *vs.* RHE (Figure 2.3c), the minimum electrochemical load for the HER light-absorber is 1.06 V (1.06 V – 0 V), whereas the minimum electrochemical load for the OER light-absorber is 0.17 V (1.23 V – 1.06 V). Even with OER overpotentials of 0.3 V – 0.4 V, the HER light-absorber has the larger bandgap and thus in an optimal configuration it is positioned on top of the OER light-absorber.

Because of the important distinction between the HER light-absorber and the OER light-absorber in these two cases, the axes in Figure 2.3b and 2.3c are labeled as HER and OER light-absorber bandgap as opposed to the usual convention (a) of top and bottom light-absorber bandgap. Because of this reason, Figure 2.3b and 2.3c are related by reflection across the 45º slope line (diagonal) for the ranges shown. This is evident based on the maximum possible STH efficiency of 34%, which is achieved with an HER light-absorber bandgap of 0.75 V and an OER light-absorber bandgap of 1.53 V in Figure 2.3b,

and with an HER light-absorber bandgap of 1.53 V and an OER light-absorber bandgap of 0.75 V in Figure 2.3c.
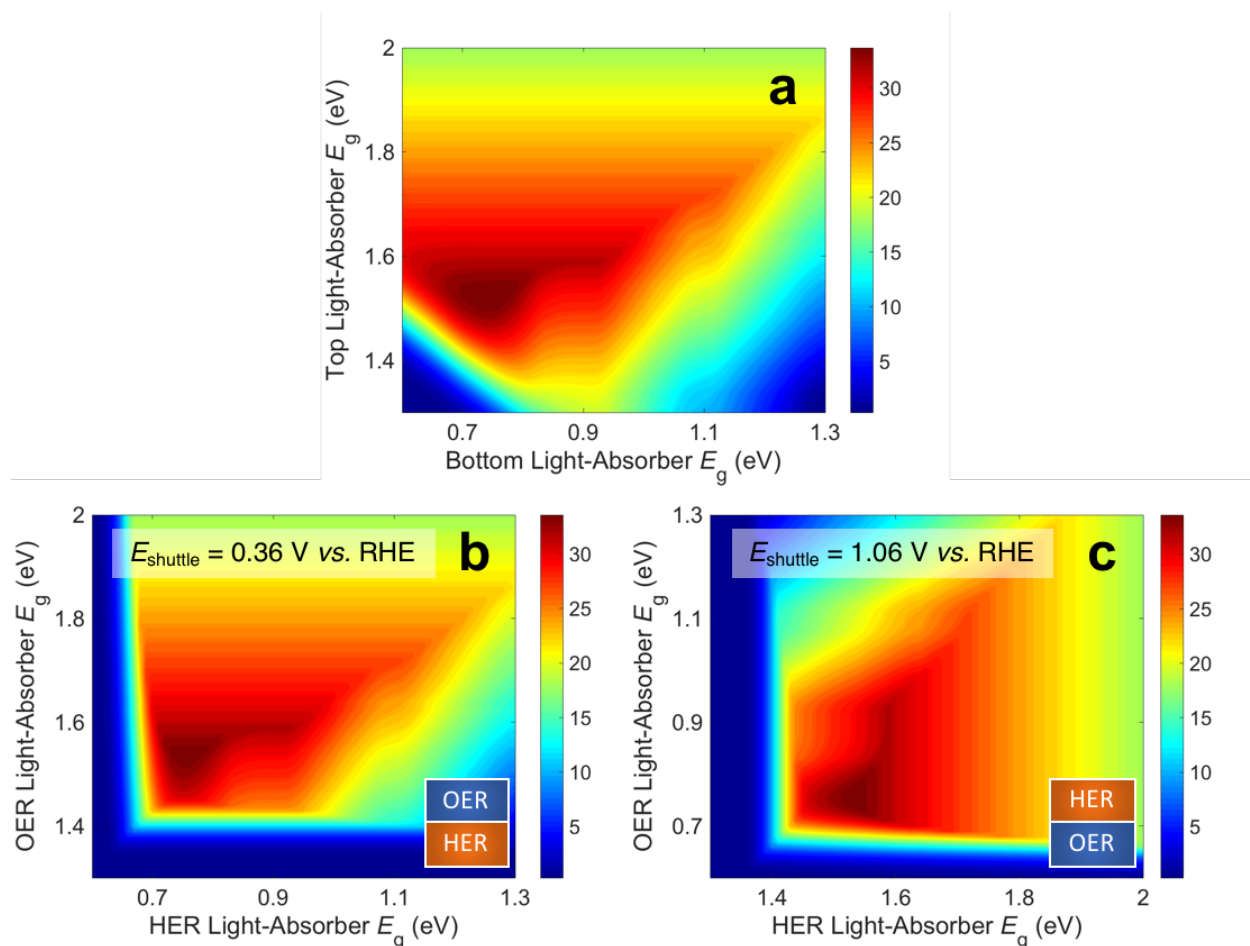


Figure 2.3. Contour plots of STH efficiency as a function of the energy of the bandgap ($E_g$) of each light-absorber assuming ideal electrocatalytic parameters with no absorptance optimization for (a) an electronically-connected tandem configuration, (b) an electrochemically-connected tandem configuration with $E_{shuttle}$ = 0.36 V *vs.* RHE and an OER top light-absorber, and (c) an electrochemically-connected tandem configuration with $E_{shuttle}$ = 1.06 V *vs.* RHE and an HER top light-absorber.

Figure 2.3 illustrates that the predicted STH efficiencies for electrically-connected and electrochemically-connected tandem devices largely follow similar trends, except when one light-absorber bandgap is too small to supply the minimum electrochemical load of its desired half reactions, as seen in Figure 2.3b and 2.3c for an HER light-absorber

bandgap of < 0.7 V or an OER light-absorber bandgap of < 1.4 V. In the electronically-connected case, the same phenomena is observed, but within a smaller region bounded by the diagonal line that satisfies the condition that the sum of the light-absorber bandgaps is < 1.7 V, and is therefore too small to supply the minimum electrochemical load for overall water electrolysis. The two values of $E_{shuttle}$ selected for Figure 2.3b and 2.3c are the only cases where the maximum possible STH efficiency for the electronically-connected device equals the maximum possible STH efficiency for the electrically-connected device. In general, the redox shuttle potential affects the distribution of STH efficiency values in the contour plot and in most cases the maximum STH efficiency is not the same.

Plotting the maximum possible STH efficiency from each contour plot as a function of the redox shuttle potential generates Figure 2.4. The observed trend results because the redox shuttle potential determines how the electrochemical loads (Equations 2.2 and 2.3) are split between the two light-absorbers, and each light-absorber must generate a photovoltage in excess of its electrochemical load. This trend is present irrespective of whether redox shuttle reactions require a kinetic overpotential. Large electrochemical loads require large photovoltages which are obtained using large bandgap light-absorbers; these light-absorbers inherently absorb less sunlight than small bandgap light-absorbers, and in turn generate smaller photocurrents than small bandgap light-absorbers. Because the photocurrent density is directly related to the STH efficiency (Equation 2.9), the STH efficiency is maximized when the bandgap energy is small while still allowing the light-absorber to attain the photovoltage required to drive its electrochemical load at a fast rate. This requirement results in four distinct regions to the data shown in Figure 2.4 that each

33

define which light-absorber limits the STH efficiency and how this limitation changes with respect to the potential of the redox shuttle. For regions 1 and 2, the top light-absorber drives the OER and reduction of the redox shuttle while the bottom light-absorber drives the HER and oxidation of the redox shuttle; for regions 3 and 4 the locations of the redox reactions are switched.
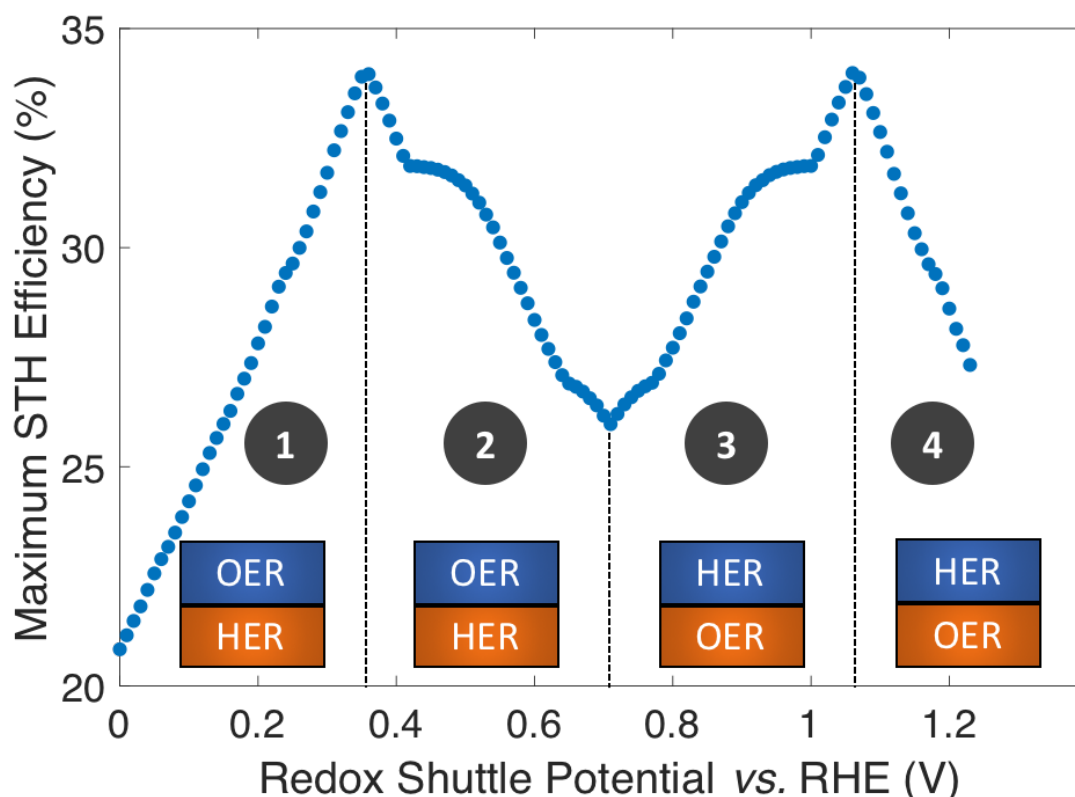


Figure 2.4. Maximum STH efficiency *vs.* $E_{shuttle}$ with ideal catalytic parameters. The maxima occur at $E_{shuttle}$ = 0.36 V, where the OER occurs at the top light-absorber, and $E_{shuttle}$ = 1.06 V, where the OER occurs at the bottom light-absorber. In regions 1 and 4, the top light-absorber limits the STH efficiency while in regions 2 and 3, the bottom light-absorber limits the STH efficiency.

As the redox shuttle potential is increased from its smallest value of 0 V to 0.36 V *vs.* RHE, the electrochemical load for the OER light-absorber decreases (Equation 2.2), while the electrochemical load for the HER light-absorber increases (Equation 2.3), all while

$V_{top} > V_{bottom}$. In this region, the electrochemical load on the top OER light-absorber is still substantially larger than the electrochemical load on the bottom HER light-absorber, forcing the bandgap of the top light-absorber to be large, and ranging from ~2.0 eV to ~1.5 eV; requiring such large bandgaps to overcome the minimum load of (1.23 V – 0.87 V) is an outcome of the slow OER kinetics. The large bandgap of the OER light-absorber means that it absorbs incident photons poorly, which results in a photocurrent that is always smaller than the photocurrent possible from an optimal bottom HER light-absorber. In region 1, there are no conditions where the electrochemical load on the bottom HER light-absorber becomes so large that its bandgap does not allow for sufficient absorption of transmitted sunlight to current-match with the top OER light-absorber. Even when the redox shuttle potential is as large as 0.36 V, the increase in the electrochemical load for the HER in this region does not negatively influence the predicted STH efficiencies because the relatively large top light-absorber bandgap still limits the net photocurrent. Therefore, in this region the STH efficiency increases with $E_\text{shuttle}$ until it equals 0.36 V, a condition where the STH efficiency reaches a global maximum value of 34 %.

In region 2, the electrochemical load is split more evenly between the two light-absorbers. Excluding the overpotentials, the minimum load on the HER light-absorber increases from 0.36 V to 0.71 V, while the load on the OER light-absorber decreases from 0.87 V to 0.52 V. Therefore, the minimum bandgap required for the top OER light-absorber to generate a photovoltage in excess of its electrochemical load is not prohibitively large, meaning that fewer photons are transmitted to the bottom light-absorber. This effect, combined with the increase in the electrochemical load on the bottom light-absorber

compared to region 1, causes photon absorption by the bottom light-absorber to limit the STH efficiency. Therefore, a decrease in STH efficiency is observed with increasing value of $E_{shuttle}$ until a local minimum in STH efficiency is observed at $E_{shuttle}$ = 0.71 V. At this point, the operating electrochemical load is equal for the two light-absorbers, and therefore this is the only condition where the location of the HER and OER light-absorbers is interchangeable. This redox shuttle potential also results in the condition where the optimum bandgap of the bottom light-absorber is the largest.

In regions 3 and 4, $E_{shuttle}$ > 0.71 V and thus, the electrochemical load on the HER light-absorber is larger than the electrochemical load on the OER light-absorber; the HER light-absorber is positioned on top of the OER light-absorber. The trend in STH efficiency as a function of $E_{shuttle}$ mirrors the trend in regions 2 and 1, because of the explanations above, but with the HER light-absorber exposed to sunlight first. The STH efficiency again reaches a global maximum of 34 %, but this time when $E_{shuttle}$ equals 1.06 V. As in region 1, when $E_{shuttle}$ > 1.06 V (region 4), STH efficiency decreases because the electrochemical load on the top HER light-absorber limits its bandgap to large values and thus its poor light absorption limits the photocurrent and therefore the STH efficiency. The reason why $E_{shuttle}$ = 1.23 V results in a substantially larger STH efficiency compared to $E_{shuttle}$ = 0 V (27% compared to 21%) is because the Pt HER electrocatalyst is at least two orders of magnitude faster than the $RuO_2$ OER electrocatalyst for the same magnitude of overpotential. This difference in reactivity is widely observed and the underlying causes of this disparate behavior are the subject of substantial ongoing research efforts.[79–81] Therefore, in region 4, relatively smaller bandgap requirements are placed on the top, HER light-absorber compared to in

region 1 for the top, OER light-absorber. In summary, the maximum STH efficiency for each value of $E_{shuttle}$ is limited by photon absorption, and therefore photocurrent (Equation 2.9), dictated by the electrochemical load of the light-absorbers: in regions 1 and 4, the large electrochemical load on the top light-absorber limits its absorption of incident solar photons while in regions 2 and 3, the bottom light-absorber has fewer solar photons transmitted to it and its electrochemical load limits its onset of absorption of transmitted light. In Figure 2.4 there are several regions where the plot changes curvature, roughly at 0.4 V – 0.5 V, 0.65 V – 0.75 V, and 0.9 V – 1.0 V. These sharp changes are a consequence of the irregular shape of the AM1.5G solar spectrum with abrupt changes in the photon fluxes. Figure 2.5 shows an analogous plot to Figure 2.4 that uses an analytical, smooth blackbody spectrum with temperature of 5800 K instead of the AM 1.5G spectrum. The overall shape of the plot is the same but the sharp changes in curvature are not present.
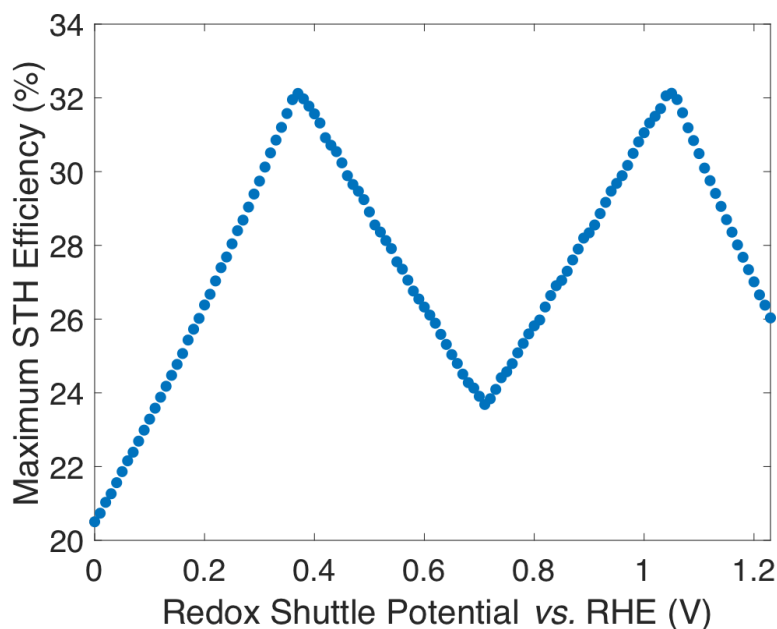


Figure 2.5. Maximum STH efficiency *vs.* $E_{shuttle}$ assuming ideal electrocatalytic parameters and using an incident spectrum of a blackbody at 5800 K instead of the solar spectrum.

Figure 2.6 presents the contour plots of STH efficiency as a function of bandgap combination without absorptance optimization (Figure 2.6a and 2.6b) and with absorptance optimization (Figure 2.6c and 2.6d) at two values of $E_{shuttle}$: $E_{shuttle}$ = 0.36 V (Figure 2.6a and 2.6c) is a redox potential that results in a global maximum for STH efficiency and $E_{shuttle}$ = 0.71 V (Figure 2.6b and 2.6d) is a redox potential that results in a local minimum in STH efficiency and where the location of the OER and the HER are interchangeable. Without absorptance optimization (Figure 2.6a and 2.6b) there exists a single bandgap combination for each value of $E_{shuttle}$ that results in its maximum STH efficiency: for $E_{shuttle}$ = 0.36 V, the bandgaps are 1.53 eV and 0.75 eV for a 34% STH efficiency, and for $E_{shuttle}$ = 0.71 V, the bandgaps are 1.75 eV and 1.13 eV for a 26% STH efficiency. When absorptance optimization is used, a single bandgap combination also maximizes STH efficiency for $E_{shuttle}$ = 0.36 V. However, the range of bandgap combinations that produce a near-optimal STH efficiency is slightly larger, as seen by the small expansion of higher efficiency contours in the lower right-hand-side of Figure 2.6c, which represent combinations where the two bandgaps are similar. Without absorptance optimization, these combinations have low efficiency because there is very little light that is absorbed by the bottom light-absorber but not by the top light-absorber, causing the bottom light-absorber to limit the overall current.

For $E_{shuttle}$ = 0.71 V, which resulted in equal operating electrochemical loads for both light-absorbers, absorptance optimization allows a larger range of bandgap combinations to produce a near-optimal STH efficiency value of 26%. Disregarding small fluctuations in the AM1.5G solar spectrum by analyzing conditions that result in at least 99% of this

maximum STH efficiency value, absorptance optimization allows the top light-absorber bandgap to range from 1.75 eV to 1.13 eV, with $A_{\text{top}}$ ranging from 0.5 to 1, and with the bottom light-absorber bandgap fixed at 1.13 eV. In every case all photons with energy > 1.13 eV are absorbed such that the photocurrent of each light-absorber is the same.
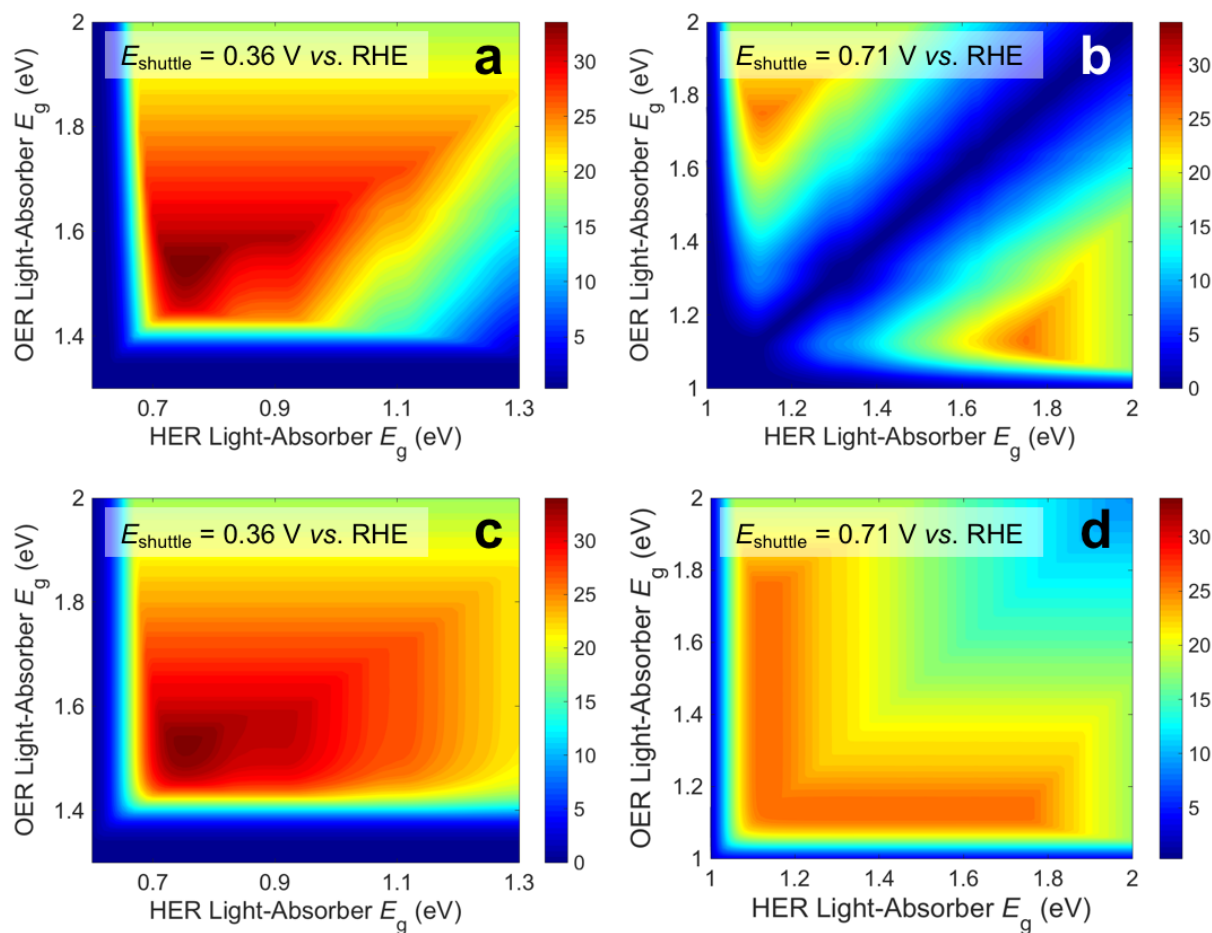


Figure 2.6. Contour plots of STH efficiency as a function of the bandgap of the HER and OER light-absorbers for (a, c) $E_{shuttle}$ = 0.36 V and (b, d) $E_{shuttle}$ = 0.71 V. Absorptance optimization is used to obtain the STH efficiencies in panels c and d.

Although absorptance optimization increases the number of high-efficiency bandgap combinations, it does not increase the maximum STH efficiency for a given value of $E_{\text{shuttle}}$. This is expected because whether or not absorptance optimization is used, the

ideal bandgap combination results in absorption of all photons above the minimum allowable bandgap, which is dictated by the electrochemical load on the bottom light-absorber, in a way that matches the current between the two light-absorbers. From a practical standpoint, having a larger range of useable bandgaps is desired because there is only a limited number of high-performance materials to choose from,[42] and the bandgaps of these materials are often difficult to adjust without negatively affecting other photocatalytic properties. Additionally, for all values of $E_{\text{shuttle}}$, absorptance optimization enables a nonzero STH efficiency for the configuration in which both light-absorbers have the same bandgap. The case where both bandgaps are equal is also the condition of maximum STH efficiency for the tandem design where the light-absorbers are positioned side-by-side and optically in parallel (Figure 2.7) instead of being stacked on top of each other and optically in series. Reactor designs incorporating tandem light-absorbers positioned optically in parallel were considered in initial techno-economic analyses of Z-scheme particle suspension reactors for solar water electrolysis.[29,72] For all other values of $E_{\text{shuttle}}$, and in the limit of key model assumptions including no gas crossover and no ohmic resistance/ion migration losses for both designs, the stacked tandem design can achieve a larger STH efficiency than the side-by-side tandem design for a fixed geometric area. The same conclusion was also observed from numerical device physics modeling of electronically-connected tandem devices.[49] Similar to absorptance optimization for the stacked tandem design, by allowing the relative areas of the two light-absorbers in the side-by-side design to differ, the maximum STH efficiency can be improved for all values of

$E_{shuttle} \neq 0.71$ V, however, the maximum STH efficiency is still smaller than for the stacked

tandem design, as shown in Figure 2.7.
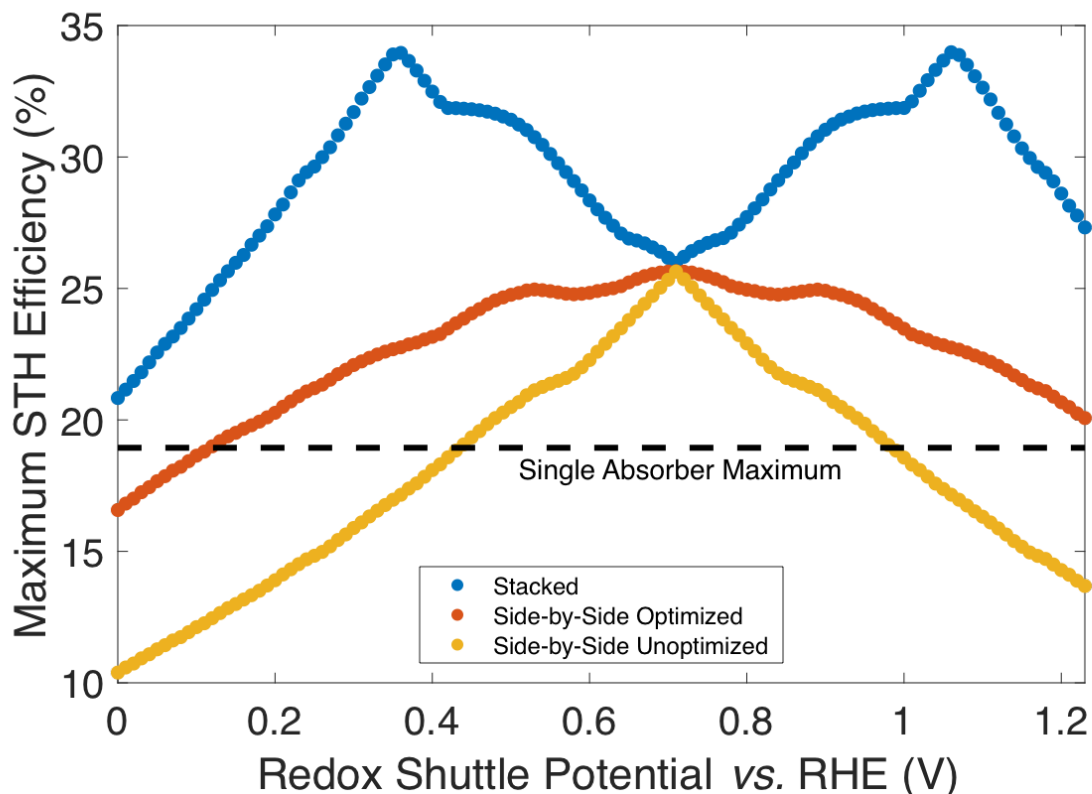


Figure 2.7. Maximum STH efficiency *vs.* $E_{shuttle}$ assuming ideal electrocatalytic parameters for a stacked tandem design, a side-by-side tandem design with the relative area of the two light-absorbers optimized, and a side-by-side tandem design with an equal (unoptimized) relative area of the two light-absorbers.

Figure 2.8 builds on Figure 2.4 and 2.6 and shows the bandgap combinations that result in near-optimal values for STH efficiency, which we define as within 99% of the maximum STH efficiency, for all values of $E_{shuttle}$ between 0 V and 1.23 V. The effect of absorptance optimization on the results is distinct under different regions. In regions 1 and 4, where the bandgap for the top light-absorber limits the maximum STH efficiency and therefore $A_{top} = 1$ is optimal, absorptance optimization does not affect the results and

therefore, a range of bandgaps for the bottom light-absorber results in the maximum STH efficiency for each value of $E_{shuttle}$. The minimum bandgap in the range is set by the electrochemical load and the maximum bandgap in the range is constrained by the condition of current-matching with the top light-absorber, which converge to a single bandgap combination at $E_{shuttle}$ values of 0.36 V and 1.06 V. In regions 2 and 3, which are bracketed by $E_{shuttle}$ values of 0.36 V and 1.06 V, the bottom light-absorber limits the STH efficiency and therefore absorptance optimization has a dramatic impact on the possible combinations of bandgaps that yield near-optimal values for STH efficiency. When the absorptance of the top light-absorber is not optimized (Figure 2.8a), there is only a single combination of bandgaps that maximizes the STH efficiency, and therefore an extremely narrow range of bandgap combinations, spanning only < 0.05 eV, results in STH efficiencies that are within 99% of their maximum value. When the absorptance of the top light-absorber is optimized (Figure 2.8b), the bandgap of the top light-absorber can range from a maximum value when $A_{top}$ = 1 to a minimum value fixed by its electrochemical load. The range of $A_{top}$ values resulting in near-optimal STH efficiencies increases to a maximum of 0.5 to 1 as $E_{shuttle}$ approaches the condition where a local minimum in STH efficiency occurs, at $E_{shuttle}$ = 0.71 V. In summary, in regions 1 and 4 absorptance optimization has no effect on bandgap combinations that result in near-optimal values for STH efficiency, but in regions 2 and 3, absorptance optimization allows for a larger range of bandgap combinations especially close to the boundary between these two regions at $E_{shuttle}$ = 0.71 V.
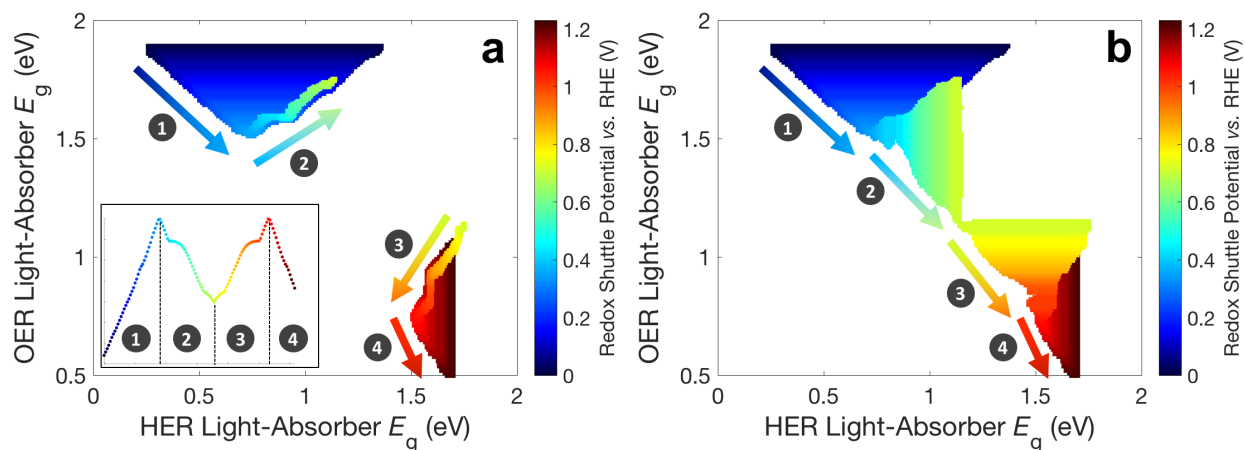
Figure 2.8. Bandgap combinations that result in an STH efficiency that is within 99% of the maximum STH efficiency for each value of $E_{shuttle}$ (a) without absorptance optimization and (b) with absorptance optimization. Marker color signifies the value of $E_{shuttle}$. The inset in panel a is a reproduction of Figure 2.4 using the same color scheme as in this figure.

For the results in Figures 2.3 – 2.8, the exchange current density of the redox shuttle was assumed to be effectively infinite, causing the redox shuttle reactions to contribute no kinetic overpotentials to the electrochemical load. Figure 2.9 shows the STH efficiency *vs.* $E_{shuttle}$ for a range of values of the exchange current density of the redox shuttle, $j_{0,shuttle}$, and still assuming selective catalysis toward the desired reactions. As $j_{0,shuttle}$ decreases, additional overpotential is required to drive redox shuttle electrocatalysis, meaning that there is an increased electrochemical load and therefore requires additional photovoltage and a larger bandgap for both light-absorbers for any value of $E_{shuttle}$. This results in a decrease in the maximum STH efficiency, which is found to have an approximately logarithmic dependence on $j_{0,shuttle}$. This logarithmic trend can be explained by Equations 2.7 and 2.8 which dictate that the electrocatalytic overpotential scales logarithmically with $j_{0,shuttle}$.
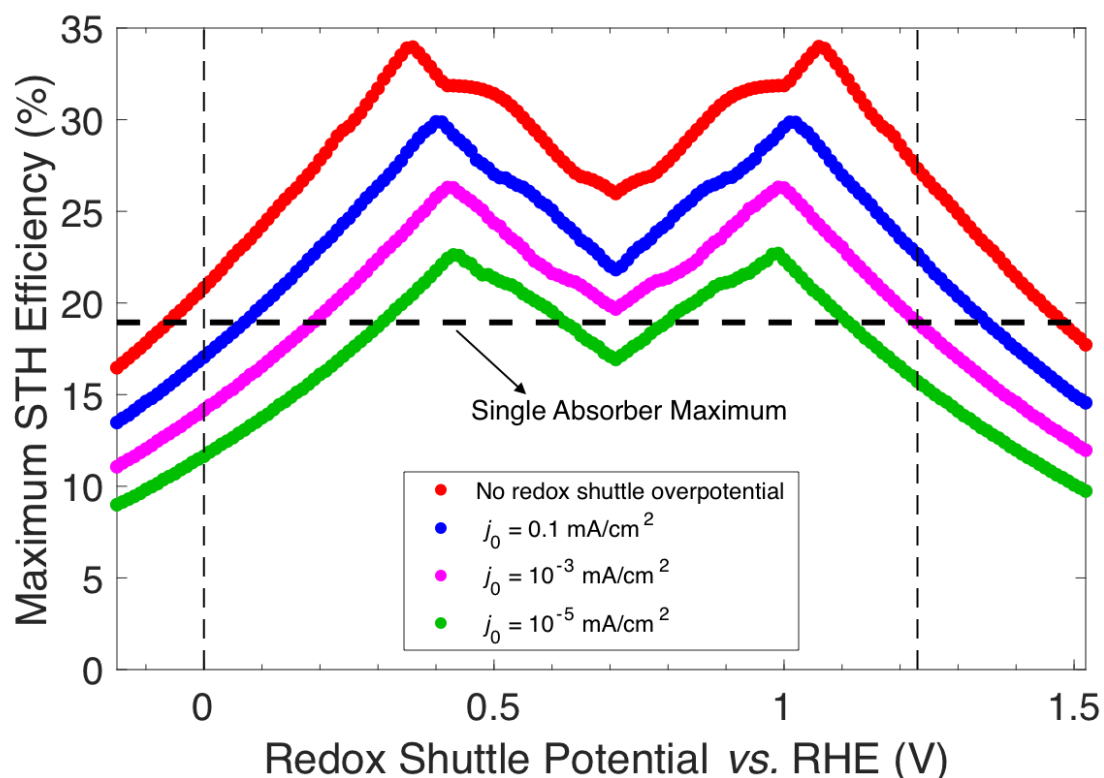
Figure 2.9. Maximum STH efficiency *vs.* $E_{shuttle}$ for different values of the redox shuttle exchange current density, $j_{0,shuttle}$, but with the same standard values for the charge-transfer coefficients. The horizontal dashed line indicates the value of the maximum STH efficiency for a single light-absorber to drive overall water electrolysis using the same electrocatalytic parameters for the OER and the HER as used for the tandem devices. The vertical dashed lines indicate the thermodynamic potentials of the HER at 0 V *vs.* RHE and the OER at 1.23 V *vs.* RHE.

For large enough values of $j_{0,shuttle}$ ($> 10^2$ mA/cm$^2$) the overpotential is effectively zero and the maximum STH efficiency plateaus, as shown in Figure 2.10; however, as $j_{0,shuttle}$ decreases the two redox shuttle potentials that result in a maximum STH efficiency converge slightly. For example, for $j_{0,shuttle}$ = $10^{-4}$ mA/cm$^2$ the maximum STH efficiency occurs for $E_{shuttle}$ = 1.00 V and 0.43 V, instead of for $E_{shuttle}$ = 1.06 V and 0.36 V when $j_{0,shuttle}$ is nearly infinite. This is because at smaller values of $j_{0,shuttle}$ the overpotential for redox shuttle reactions represents a larger fraction of the electrochemical load on each light-

absorber and therefore the electrochemical loads on each light-absorber are more similar in value. Because equal electrochemical loads on each light-absorber attains a maximum STH efficiency at $E_{\text{shuttle}}$ = 0.71 V, the two redox shuttle potentials that result in a maximum STH efficiency converge to this value as the electrochemical loads become more similar in value. The local minimum in STH efficiency always occurs at $E_{\text{shuttle}}$ = 0.71 V, because this is the condition where the operating electrochemical loads on each light-absorber are the same and therefore, when $j_{0,\text{shuttle}}$ for the two redox shuttle reactions is changed by the same amount, the additional overpotential and thus the increase in electrochemical load for each light-absorber is equal.
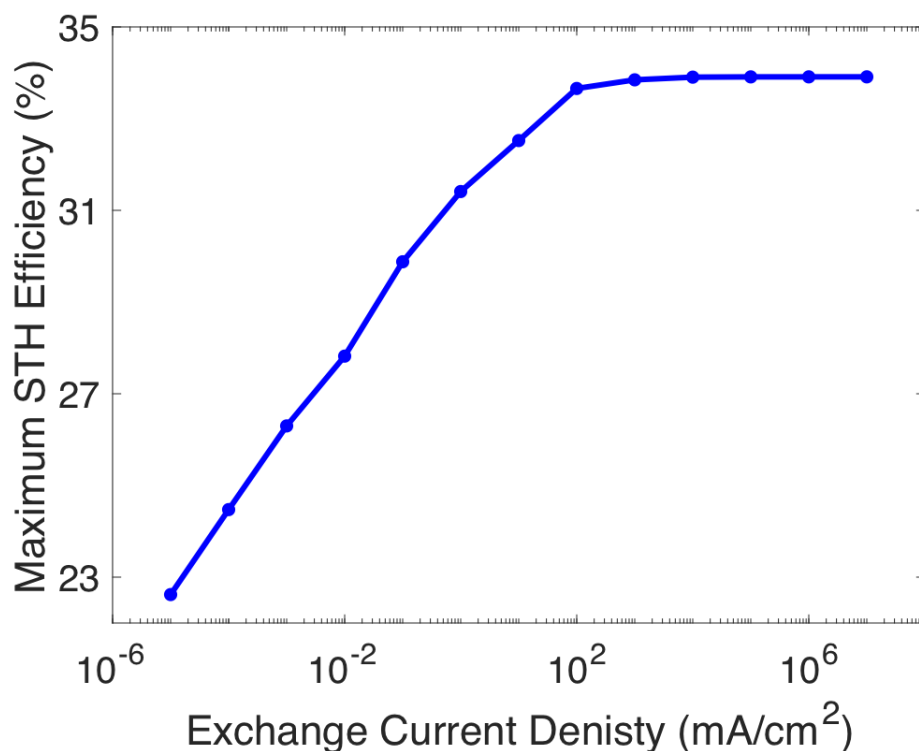


Figure 2.10. Global maximum STH efficiency *vs.* exchange current density for the redox shuttle reactions.

In Figure 2.9, the STH efficiency is plotted for $E_{\text{shuttle}}$ values that extend beyond the water stability window of 0 V to 1.23 V as indicated by vertical dashed lines. For $E_{\text{shuttle}} < 0$ V, the minimum electrochemical load for the top light-absorber, i.e. (1.23 V – $E_{\text{shuttle}}$) in region 1 by Equation 2.2, exceeds the minimum electrochemical load for overall water electrolysis, (1.23 V – 0 V) by Equation 2.1, while for $E_{\text{shuttle}} > 1.23$ V, the minimum electrochemical load for the top light-absorber, i.e. ($E_{\text{shuttle}} - 0$ V) in region 4 by Equation 2.3, also exceeds the minimum electrochemical load for overall water electrolysis. It is apparent from Figure 2.9 that the maximum STH efficiency of the tandem device exceeds that of a non-tandem device that incorporates a single light-absorber, as indicated by the horizontal dashed line; intersections of the colored plots with the horizontal dashed line represent conditions where the maximum STH efficiencies are the same for the two designs. Figure 2.11 shows the relationship between STH efficiency and bandgap for a single light-absorber design that uses the same OER and HER electrocatalytic parameters as the tandem design. This phenomenon occurs because, while the minimum electrochemical load on the top light-absorber in the tandem design is always larger than the minimum electrochemical load for overall water electrolysis, the operating electrochemical load is not necessarily larger than the operating electrochemical load for overall water electrolysis. This enables the tandem design to have a larger maximum STH efficiency than the single light-absorber design even when $E_{\text{shuttle}}$ values extend beyond the water stability window. This occurs when $|\eta_{\text{shuttle,red}}| < |\eta_{\text{HER}}|$ in region 1 and $\eta_{\text{shuttle,ox}} < \eta_{\text{OER}}$ in region 4 and is a consequence of the relative values for the exchange current densities of each reaction.
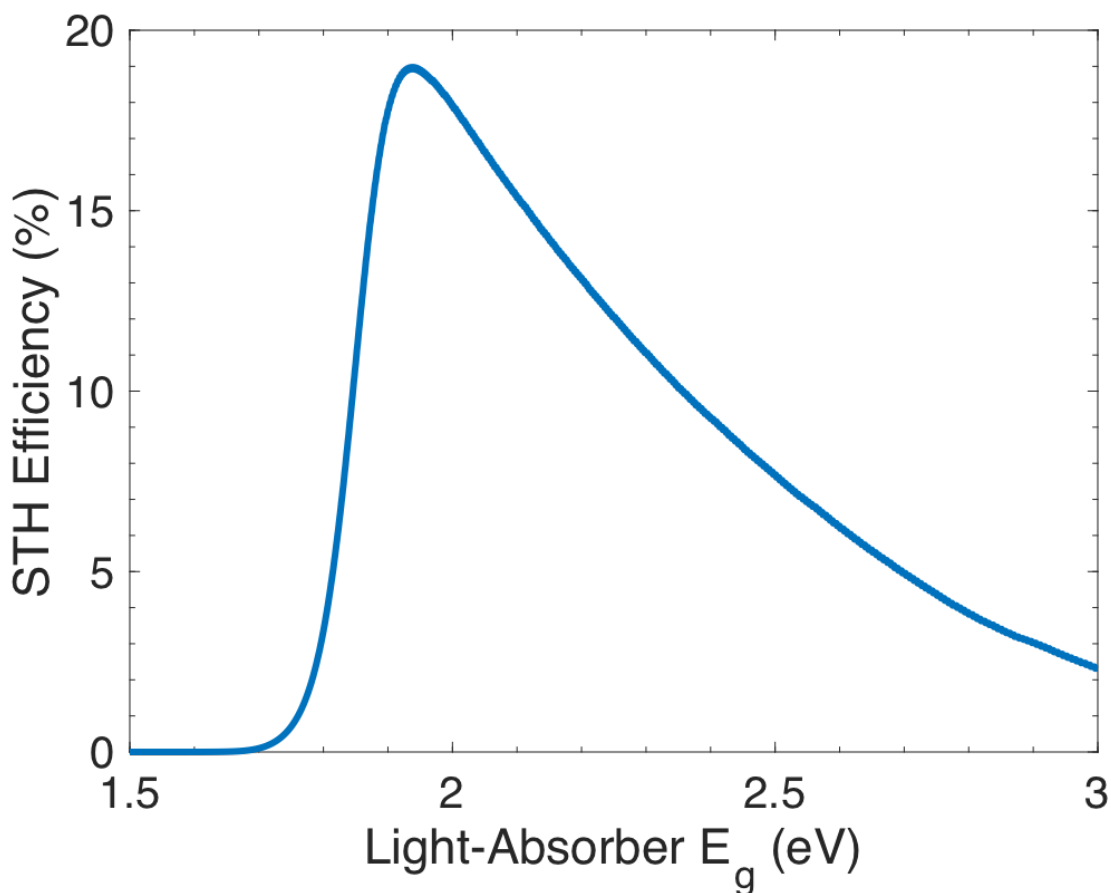
Figure 2.11. STH efficiency *vs.* light-absorber bandgap for the design in which a single light-absorber drives the OER and the HER (i.e. overall water electrolysis).

Because each light-absorber must catalyze two different redox reactions simultaneously, it may be necessary to utilize multiple co-catalysts each with fine-tuned electrocatalytic properties. Thus it is of practical importance to understand how the redox shuttle exchange current density, $j_{0,shuttle}$, affects STH efficiency. Practically, a wide range of factors can affect $j_{0,shuttle}$, including the material and surface properties of the co-catalyst(s) used, ion concentrations including the solution pH for proton-coupled electron-transfer reactions, and the number of electrons involved in the redox reaction[33,38,39,41]. Because

47

optimizing a device requires consideration of the HER, the OER, and the redox shuttle reactions, a wide range of $j_{0,shuttle}$ values is expected. As $j_{0,shuttle}$ decreases from its nearly infinite value (red) to a value similar that of $j_{0,HER(Pt)}$ (blue) and ultimately to a value that is similar to that of $j_{0,OER(RuO2)}$ (green), the range of values for $E_{shuttle}$ where the tandem design is more efficient than the single light-absorber design narrows. When $j_{0,shuttle}$ is large ($\geq 0.1$ mA/cm$^2$), the maximum STH efficiency for the tandem design exceeds that for the single light-absorber design over a significant range of $E_{shuttle}$ values above 1.23 V (up to 1.35 V for $j_{0,shuttle}$ = 0.1 mA/cm$^2$). Because the value of $j_{0,shuttle}$ is large, the electrochemical load of the top light-absorber is predominantly affected by the overpotential for either the HER or the OER, and to a lesser extent the overpotential for the redox shuttle reaction. This is in contrast to the design with the single light-absorber, which must supply the overpotential for both the HER and the OER and therefore leads to a larger electrochemical load and lower maximum STH efficiency. However, for $j_{0,shuttle} < 0.1$ mA/cm$^2$ there are conditions where the single light-absorber maximum STH efficiency exceeds that of the tandem light-absorber maximum STH efficiency even when $E_{shuttle}$ is within the water stability window. This occurs when the sum of the thermodynamic potentials and overpotentials for the redox shuttle reaction and either the HER or the OER (Equation 2.2 or 2.3) for the top light-absorber is *larger* than the sum of the thermodynamic potentials (1.23 V) and overpotentials for overall water electrolysis, such that the operating electrochemical load on each light-absorber in the tandem device is smaller than the operating electrochemical load on the single light-absorber.

We have clearly shown that the value of $E_{shuttle}$ substantially impacts the STH efficiency of electrochemically-connected tandem devices for solar water electrolysis. In practice, the optical and transport properties of the redox shuttle are also important; the shuttle must not competitively absorb sunlight and must transport rapidly between the two reactor compartments. In our previous work, we identified two candidate redox shuttles that had these beneficial properties, $IO_3^-/I^-$ and $Q/QH_2$, and predicted that a steady-periodic STH efficiency of ~4% was possible when either was used.[31] The thermodynamic potentials of these redox shuttles, 1.085 V for $IO_3^-/I^-$ and 0.7 V for $Q/QH_2$, lie near the predicted global maximum and local minimum in the STH efficiencies reported herein, respectively. Thus, we anticipate that the $IO_3^-/I^-$ redox shuttle is a more promising choice for a reactor, assuming that it is implemented in a device with nearly ideal HER and OER electrocatalysts and light-absorbers with bandgaps near 1.53 eV and 0.75 eV, respectively. Methylammonium lead triiodide perovskite or amorphous silicon is a close match for the larger bandgap while germanium or iron pyrite is a close match for the smaller bandgap. The $Q/QH_2$ redox shuttle could also be effectively utilized in a device with STH efficiency between 20% and 26%, for a wide range of bandgap combinations when absorptance optimization is used (Figure 2.6b). In this case, crystalline silicon could possibly be used for both light-absorbers. The other commonly considered redox shuttles, $Fe^{3+}/Fe^{2+}$ and $I_3^-/I^-$, with thermodynamic potentials of 0.77 V and 0.536 V, respectively, also lie near the predicted local minimum STH efficiencies, where implementing absorptance optimization can extend the range of effective light-absorber bandgaps that can be used to attain near-optimal STH efficiencies.

## 2.4. Conclusions

Presented herein are calculations of the theoretical STH efficiency limits of electrochemically-connected tandem solar water splitting devices with soluble redox shuttles mediating charge transport between the OER and the HER light-absorbers. These devices behave fundamentally different from the relatively well-understood electrically-connected tandem structures. The analyses showed that the thermodynamic potential of the redox shuttle reaction has a significant impact on the maximum possible STH efficiency and thus the selection of the redox shuttle is as important as the selection of the light-absorbers and co-catalysts.

For redox shuttles exhibiting zero kinetic overpotentials, optimally selective catalysis, and optimal redox potentials of $E_{shuttle}$ = 0.36 V or $E_{shuttle}$ = 1.06 V *vs.* RHE, electrochemically-connected tandem devices can attain the same maximum STH efficiency of 34% as possible with electronically-connected tandem devices. The total number of absorbed photons is maximized by splitting the electrochemical loads unevenly between the two light-absorbers. This study also demonstrated the influence of other design parameters on STH efficiency, including absorptance of the top light-absorber and exchange current density of the redox shuttle. Optical absorptance was determined to be a crucial parameter to widen the range of the top and bottom light-absorber bandgaps that attain near-optimal STH efficiencies, especially for redox shuttle potentials is between 0.36 V and 1.06 V. As the exchange current density of the redox shuttle reactions decreased, the maximum possible STH efficiency decreased and the redox shuttle potentials to attain this STH efficiency converged slightly to the redox shuttle potential of

0.71 V, which is the local minimum STH efficiency. Predicted results elucidate that even with slow redox shuttle electrocatalysis, e.g. $j_{0,\text{shuttle}} = 10^{-5}$ mA/cm$^2$, STH efficiencies above the limit of 19% for a single light-absorber design can still be achieved with a tandem device as long as the redox shuttle potential is in the range of 0.3 V – 0.6 V or 0.8 V – 1.1 V. Moreover, results prove that for optimal and selective redox shuttle electrocatalysis, the electrochemically-connected tandem design is more efficient than the single light-absorber design even when redox shuttle potentials lie outside of the water stability window.

Based on the predicted results in this work, and favorable optical and transport behavior revealed in prior work,[31] we expect that the $IO_3^-/I^-$ redox shuttle with a potential of 1.085 V exhibits great promise to achieve close to maximum STH efficiencies with optimally chosen light-absorber bandgaps of 1.53 eV and 0.75 eV. Collectively, these results provide insights to the broader community of researchers on the complex interplay between the numerous parameters in electrochemically-connected tandem devices for solar water electrolysis.

# 3. Detailed Balance Model for Ensembles of Optically Thin Light Absorbers Each Performing a Net Solar Fuels Reaction

Detailed balance models of solar cells and solar fuels constructs have been reported when materials are assumed to absorb above-bandgap light strongly. Herein we report a model that calculates the sunlight-to-fuel energy-conversion efficiency as a function of bandgap energy for an ensemble of identical, optically thin light-absorbers that are optically in series and each performs the fuel-forming reactions. We demonstrate that for catalytic Tafel parameters relevant to water electrolysis, the maximum efficiency increases from 19% for the case of a single light-absorber to 23% when that single light-absorber is split into 128 identical light-absorbers. Notably, the maximum efficiency for a 1.75 eV bandgap material is calculated to increase from 1% for a single light-absorber to 20% for 128 identical light-absorbers. These enhanced efficiencies are logarithmically dependent on the number of light-absorbers and are due to improvements in the utilization of photons which result in a better match of the light-absorber power output to the catalytic load. The improved match of the power output and load is attributed to radiative coupling between the light-absorbers and a decrease in the rate of electron–hole pair recombination. The second effect is unique to systems where light drives chemical reactions and is caused by the specific dependencies of the operating potential and current density of a light-absorber on its absorptance, incident light intensity, and Tafel parameters. We explore the complex

52

interdependencies of this model and describe how it can be applied to improve the efficiency of real solar fuels systems, such as those based on commercially relevant silicon and next-generation photocatalyst particle-suspension reactor designs.

## 3.1.    Motivation

Artificial photosynthesis aims to mimic natural photosynthesis by converting and storing photon energy as chemical potential via chemical transformations that are net thermodynamically unfavorable. The most effective photochemical demonstrations of artificial photosynthesis use photons to generate highly mobile electron and/or hole charge carriers in solid materials. These artificial photosynthetic constructs couple the physics of optical absorption and emission of photons with the chemical kinetics of generation and recombination of mobile charge carriers and electrochemical charge-transfer reactions. One of the most important guiding theories in the development of artificial photosynthetic systems is the theory that dictates the energy-conversion efficiency limit as a function of model parameters. This theory has been extensively developed for and has helped guide the experimental design of high efficiency solar water splitting and solar fuels devices using monolithic semiconductors as light-absorbers.[46,48–50,75] An extraordinary range of device designs, materials parameters, light harvesting scenarios, and redox chemistries have been explored, yet remarkably there is one consistent assumption in nearly all of these models[31,82]: *each pair of light-driven redox reactions is performed at the surface of a single monolithic unit*. This is true for not only single-absorber device models, but also tandem device models where each of the light-absorbers drives different redox reactions or exchanges charge with a different portion of the circuit. In none of these models were there

multiple independent light-absorbers, each with the same materials properties and driving the same pair of redox reactions. The changes to the theoretical considerations of such a system are subtle: when there are multiple independent light-absorbers that are electronically decoupled from each other, each light-absorber drives both redox reactions but has a different rate of generation of mobile charge carriers and net reaction products.

It is not surprising that models of artificial photosynthetic systems only incorporate monolithic units to drive desired energy conversion and storage redox chemistry, because nearly all demonstrations of semiconductor solar fuels devices use monolithic components. However, there is a unique class of solar energy conversion designs that instead use ensembles of molecules or semiconductor photocatalyst particles that are not in direct electronic contact with each other to each perform the same net redox chemistry.[39,41,42,66,67,69,83,84] The lack of an electronic connection means that each unit individually performs the desired redox chemistry and the net rate of product formation from the ensemble determines the overall solar-to-fuels energy conversion (STF) efficiency. This arrangement of multiple independent light-absorbers is pertinent to natural photosynthesis in green plants, where each pair of photosystems only absorbs a small amount of incident sunlight and independently drives two half-reactions, but the net effect of the collection of all dual-photosystems is to generate substantial amounts of reaction products. The most successful experimental demonstrations of artificial photosynthesis where each unit weakly absorbs incident sunlight were reported by Domen and coworkers using photocatalyst sheets to perform water electrolysis.[83–85] In these devices the size of the photocatalyst particles is small enough that they transmit significant amounts of light

and the particles are weakly coupled so that particle-to-particle electron-transfer is inefficient.

Reports of models that evaluate these types of artificial photosynthetic constructs are uncommon[31,86–88]. Most recently, we developed a device-level transport model for a Z-scheme photocatalyst particle suspension reactor mediated by a redox shuttle that included optical absorption, semiconductor charge separation, and chemical species transport.[31] This continuum model captured the phenomena of variable quasi-Fermi-level splitting and differing rates of electrocatalysis and diffusive charge transport at different light intensities, because incident light was attenuated deeper into the device by a Beer–Lambert law absorption profile. However, inclusion of chemical species transport in that model resulted in reactor-level STF efficiencies that were dominated by these physical processes and masked the effects that multiple light-absorbers have on the STF efficiency. This explains why the phenomena we describe herein were not apparent in that work and provides rationale for why our model does not intentionally include effects due to mass transport.

In the work presented herein we report a generalized model that specifically isolates the effect of having an ensemble of light-absorbers, instead of a single light-absorber, each perform water electrolysis after absorbing only a portion of the above-bandgap incident light. Simulations performed with these models identify several physical processes that only occur when multiple independent light-absorbers each perform a net solar fuels reaction and this results in substantially increased STF efficiencies for materials with desirable bandgaps. These processes include more efficient matching of the power

output from each light-absorber to the electrochemical load when each light-absorber absorbs less incident solar radiation and reabsorption of photons emitted from other particles via radiative recombination.

## 3.2. Numeric Model

### 3.2.1. General Considerations

Our goal is to define a general model that can accurately predict the efficiency limits of an ensemble of light-absorbers that convert sunlight into chemical energy via redox chemistry. Although the particle suspension reactor is a motivating design for such a model, we do not make specific choices about materials properties or device geometries in order to keep the model general. As a result, we assume all materials are identical, have index of refraction of one, and are perfectly planar and extend infinitely in that plane. The terms in the detailed-balance analysis that arise from specific geometries and material refractive indices appear as coefficients in the photodiode equation and are independent of other model parameters. Therefore the trends presented in this work are perfectly expandable to other periodic systems with specific device properties. Instead of modeling a three-dimensional grid of light-absorbers, it suffices to model the light-absorbers as infinite sheets because in a three-dimensional model, symmetry causes there to be no net radiative coupling in the planar directions, under the reasonable assumption of either perfectly reflective container walls or a sufficiently large container with negligible edge-effects. A three-dimensional grid of cubic light-absorbers thus would give the exact same result as the infinite sheets considered in this model. A three-dimensional model using other absorber shapes, such as spheres, complicates the model because the scaling relationship

between absorptance of solar photons and absorber size does not simply follow the Beer–Lambert law; the thickness of each absorber in the direction of solar photon propagation is not constant over the area of the absorber which causes the average absorptance over the entire absorber to have a more complex dependence on absorber radius. It would certainly be possible to incorporate this into the model, but for generality and clarity we use the simplest planar case. The simplification from three-dimensions to two-dimensions would break down if the light-absorbers were of different shapes and/or sizes but should represent a large ensemble of similarly-sized nanoparticles well. We only consider a single light-absorber bandgap in order to focus specifically on the effects of a multiple-absorber configurations without the convolutions of optimizing a tandem design. However, again, the results herein are applicable to multiple-absorber configurations that are either electrically or electrochemically connected. We use electrocatalytic parameters relevant to water electrolysis, although the model can be applied to any set of electrochemical reactions. Lastly, because data for most efficient demonstrations of solar fuels production are reported in terms of potential ($V$) and current density ($j$), and not (electro)chemical potential ($\mu$) and flux ($J$), when possible our derivations and analyses use the more widely recognized electrochemical terminology and nomenclature.

### 3.2.2. Detailed Balance Model of $N$ Absorbers

Figure 3.1 shows a schematic of the model, which consists of a one-dimensional array of $N$ planar light-absorbers each with identical bandgap energy, $E_g$, and optical thickness, $\tau$. The parameter $\tau$ is the dimensionless product of the absorber thickness and the absorption coefficient. Although this is generally a wavelength-dependent property, every other

portion of the model treats all above-bandgap photons identically and thus the use of a single absorption coefficient for all photons above the bandgap energy has no ultimate effect on the model results while drastically simplifying the formulation. The absorptance $A$ of above-bandgap photons is then,

$$A = 1 - e^{-\tau} \tag{3.1}$$

The $N$-absorber stack is assumed to be in thermal equilibrium with its surroundings at temperature $T$. There is thus incident blackbody radiation on the top and bottom of the stack while each light-absorber is able to emit light via radiative recombination. This means that the absorbers are radiatively coupled to one another because some of this light can be reabsorbed by neighboring absorbers. Solar flux is incident only on the top of the stack; we use the convention that the first absorber is closest to the Sun while the $N$th absorber is furthest from the Sun.
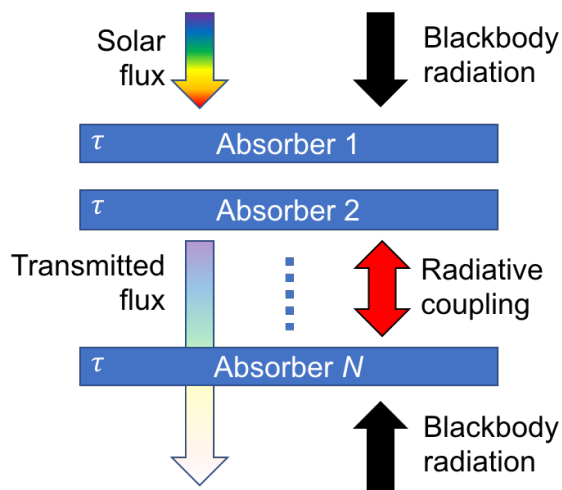


Figure 3.1. Schematic of the modeling domain for serial ensemble of optically coupled absorbers.

The net flux of charge carriers that drive redox chemistry from each absorber, which when multiplied by their charge equals the current density, is a sum of the absorbed

58

photon flux from solar and blackbody radiation and the negative flux due to radiative and non-radiative recombination. Using the subscript n to denote the $n^{th}$ absorber in the stack, we define the current density due to absorption of solar photons as follows,

$$j_{ph,n} = q\Phi_0 (1-A)^{n-1}(A) \tag{3.2}$$

where $q$ is the elementary charge and $\Phi_0$ is the total solar photon flux incident on the absorber stack. This expression is the product of the total solar flux, the fraction $(1-A)^{n-1}$ that is transmitted by the (n – 1) absorbers that lie between the sun and the $n^{th}$ absorber, and the fraction $A$ that the $n^{th}$ absorber absorbs. The total blackbody flux incident on one side of the stack, $j_{bb}$, is as follows,

$$j_{bb} = \frac{2\pi q}{c^2} \int_{E_g/h}^{\infty} v^2 e^{-hv/kT} \, dv \tag{3.3}$$

where $c$ is the speed of light in vacuum, $h$ is the Planck constant, $v$ is the frequency of the radiation, $k$ is the Boltzmann constant, and $T$ is the ensemble and blackbody temperature. An isolated absorber would be exposed to this radiation on both its top-side and bottom-side but only absorb a fraction $A$. Detailed-balance dictates that the potential-dependent radiative recombination rate must be equal to this total absorption rate at zero current and that in general the following expression for the recombination rate holds,

$$j_{rad,n} = -2j_{bb}Ae^{qV_n/kT} \tag{3.4}$$

where $V_n$ is the operating potential of the light-absorber.[54–57] This negative current density due to radiative recombination *vs.* potential relationship has the form used in the Shockley photodiode equation, which is a broadly utilized Boltzmann approximation of the actual relationship for an ideal solar converter.[55,56,59] The difference between the ideal equation

and the approximate equation is negligible for all bandgaps and rates of illumination studied in this work.

Each absorber in the stack absorbs light emitted by the rest of the stack, a phenomenon termed "photon recycling[89-91]." Because of Equation 3.4, this means that the current for each absorber depends on the potential of the other absorbers. The current density resulting from absorber n absorbing light emitted by absorber m is as follows,

$$j_{\text{abs,m}\rightarrow\text{n}} = \frac{1}{2}j_{\text{rad,m}}(1-A)^{|m-n|-1}(A) \tag{3.5}$$

The factor of one half is due to the fact that only half of the total radiation from absorber m propagates in the direction of absorber n. Including terms for the absorption of ambient blackbody flux, the total current density at absorber n resulting from absorption of non-solar photons takes on the following expression,

$$j_{\text{abs,n}} = j_{\text{bb}}A[(1-A)^{\text{n}-1} + (1-A)^{N-\text{n}}] + \sum_{\text{m}\neq\text{n}} j_{\text{abs,m}\rightarrow\text{n}} \tag{3.6}$$

This expression satisfies the requirement that $j_{\text{abs,n}} = j_{\text{rad,n}}$ for all n when all $V_{\text{n}}$ are zero and there is no incident solar radiation which is analytically proven in Section 3.2.3. The complete current density *versus* potential relationship describing non-radiative recombination follows,

$$j_{\text{NR}} = 2j_{\text{bb}}A\left(\frac{1}{f_{\text{c}}}-1\right)(1-e^{qV_{\text{n}}/kT}) \tag{3.7}$$

where $f_{\text{c}}$ is the fraction of recombination that is radiative. This expression for non-radiative recombination assumes that $f_{\text{c}}$ is not dependent on absorbed photon flux or on electric potential and that non-radiative recombination has the same potential dependence as radiative recombination. Again, this is a common assumption made in analogous analyses

that is a good first approximation for most conditions. The Kirchhoff current law condition requires that at steady-state the current into and out of the light-absorber is equal, which yields the following complete current density *vs.* potential relationship for each absorber,

$$j_n = j_{ph,n} + j_{abs,n} + j_{rad,n} + j_{NR} \qquad (3.8)$$

where $j_{rad,n}$ and $j_{NR}$ (Equations 3.4 and 3.7) both include a recombination term with $e^{qV_n/kT}$; the total coefficient for this exponential term in Equation 3.8 is $\frac{1}{f_c} 2j_{bb}A$, which is the reverse saturation current density in the photodiode equation. The larger the reverse saturation current density, the larger the dark current, and the smaller the open-circuit potential under illumination.

The electrochemical load on each light-absorber is determined by two Butler–Volmer equations and the potential difference required to drive the two redox reactions, $E_0 = E_0^{ox} - E_0^{red}$, where the superscripts "ox" and "red" denote the (ox)idation and (red)uction reactions. Because each light-absorber performs an oxidation and a reduction reaction with equal and opposite signs of the current density in order to maintain charge neutrality, the following current density *versus* potential relationships hold,

$$j_n = j_0^{ox} \left( \exp\left( \frac{\alpha_a^{ox} \eta_n^{ox} q}{kT_{atm}} \right) - \exp\left( -\frac{\alpha_c^{ox} \eta_n^{ox} q}{kT_{atm}} \right) \right) \qquad (3.9)$$

$$j_n = -j_0^{red} \left( \exp\left( \frac{\alpha_a^{red} \eta_n^{red} q}{kT_{atm}} \right) - \exp\left( -\frac{\alpha_c^{red} \eta_n^{red} q}{kT_{atm}} \right) \right) \qquad (3.10)$$

where for i = ox/red, $j_0^i$ is the exchange current density, $\alpha_a^i$ and $\alpha_c^i$ are the anodic are cathodic charge transfer coefficients, respectively, and $\eta_n^i$ is the overpotential beyond $E_0^i$ that is required to obtain $j_n$. The following relationship between the operating potential, the two overpotentials, and $E_0$ is then,

61

$$V_n = \left(E_0^{ox} - E_0^{red}\right) + \left(\eta_n^{ox} - \eta_n^{red}\right) \tag{3.11}$$

Equations 3.8–3.11 represent $4N$ coupled equations which are simultaneously solved using the vpasolve numeric solve function in MATLAB 2017b.

The total solar-to-fuel (STF) efficiency of the ensemble is found by taking of the sum of the individual $j_n$ values, multiplying it by the formal potential of the fuel-forming reaction, $E_0 = E_0^{ox} - E_0^{red}$, and dividing by the total incident solar irradiance $I_0$,

$$\eta = \frac{\sum j_n \times E_0}{I_0} \tag{3.12}$$

where the sum of the individual $j_n$ values is multiplied by the potential stored in the fuels and divided by the total incident solar irradiance $I_0$. The baseline parameters used in the model are shown in Table 1. The catalytic parameters are assumed based on state-of-the-art literature values at room temperature for the aqueous oxygen evolution reaction and the aqueous hydrogen evolution reaction.[50,77,78] The optical thickness of the entire stack is $\tau_{total} = \tau * N.$ Unless otherwise noted, $\tau_{total}$ is kept as a fixed parameter while $N$ is varied, meaning the total amount of light absorbed by the system remains constant for different values of $N$. Conversely, this means that as $N$ increases, the absorptance of each individual absorber decreases. A baseline value of $\tau_{total} = 4.6$ is selected, meaning that the stack absorbs 99% of all incident light. Other baseline parameters include 100% radiative recombination and $\Phi_0$ follows the AM1.5G solar spectrum.

| Parameter | Baseline Value |
|---|---|
| $\tau_{\text{total}}$ | 4.6 |
| $T$ | 298 K |
| $f_c$ | 1 |
| $E_0$ | 1.23 V |
| $j_0^{\text{ox}}$ | 3.3 x $10^{-6}$ mA/cm$^2$ |
| $j_0^{\text{red}}$ | 1.5 x $10^{-1}$ mA/cm$^2$ |
| $\alpha_a^{\text{ox}}$ | 1.97 |
| $\alpha_c^{\text{ox}}$ | 1.97 |
| $\alpha_a^{\text{red}}$ | 1.60 |
| $\alpha_c^{\text{red}}$ | 1.60 |

Table 1. Baseline parameters used in the model.

### 3.2.3. Proof of radiative microscopic reversibility

Consider an ensemble on $N$ identical planar light-absorbers each with optical thickness, $\tau$, in thermal equilibrium with their surroundings through radiative coupling via their top and bottom surfaces only and no interactions from their sides. Solar radiation is incident on the ensemble on the top side of the $n = 1$ light-absorber, and blackbody radiation is exchanged with the surroundings via the top of the $n = 1$ light-absorber and bottom $n = N$ light-absorber. Following the main text, the transmittance of each absorber, $T$, and the incident blackbody flux on one side of the ensemble, $j_{\text{bb}}$, are defined as follows,

$$T = e^{-\tau} \tag{3.13}$$

$$j_{\text{bb}} = \frac{2\pi q}{c^2} \int_{E_g/h}^{\infty} v^2 \exp(-hv/kT) \tag{3.14}$$

63

where $q$ is the fundamental charge, $c$ is the speed of light in vacuum, $E_g$ is the material bandgap, $h$ is the Planck constant, $k$ is the Boltzmann constant, and $T$ is the ensemble and blackbody temperature. Using the subscript n to denote the $n^{th}$ light-absorber in the ensemble, the total radiative flux emitted by both sides of a light-absorber is defined as follows,

$$j_{rad,n} = j_{bb}(1 - T)e^{qV_n/kT} \tag{3.15}$$

where $V_n$ is the potential of the $n^{th}$ light-absorber. Photon fluxes are converted to current densities via multiplication by $q$. The radiative flux emitted by absorber m and absorbed by absorber n is then

$$j_{abs,m \to n} = \frac{1}{2}j_{rad,m}\left(T^{|m-n|-1}\right)(1 - T) \tag{3.16}$$

Summing all fluxes absorbed by a single absorber, n, gives an expression for the total absorbed flux by the $n^{th}$ absorber as follows,

$$j_{abs,n} = j_{bb}[T^{n-1} + T^{N-n}](1 - T) + \sum_{m \neq n} j_{abs,m \to n} \tag{3.17}$$

In order to obey microscopic reversibility, $j_{abs,n}$ and $j_{rad,n}$ must be equal for all n when $V_n = 0$ and in the absence of additional incident light. We first set $V_n$ to zero to obtain a new expression for $j_{rad,n}$,

$$j_{rad,n} = 2j_{bb}(1 - T) \tag{3.18}$$

We then plug this expression in and evaluate the expression for $j_{abs,n}$,

$$j_{abs,n} = j_{bb}\left[T^{n-1}(1 - T) + T^{N-n}(1 - T) + \sum_{m \neq n} T^{|m-n|-1}(1 - T)^2\right] \tag{3.19}$$

Factor this expression and expand the term in the sum as follows,

$$j_{\text{abs,n}} = j_{\text{bb}}(1 - T)\left[T^{n-1} + T^{N-n} + \sum_{m \neq n}\left(T^{|m-n|-1} - T^{|m-n|}\right)\right] \tag{3.20}$$

Add and subtract the m = n terms, which constitutes adding zero to the expression, to rewrite the sum as follows,

$$j_{\text{abs,n}} = j_{\text{bb}}(1 - T)\left[T^{n-1} + T^{N-n} - T^{-1} + T^0 + \sum_{m}\left(T^{|m-n|-1} - T^{|m-n|}\right)\right] \tag{3.21}$$

Expand both terms in the sum, which is bounded from m = 1 to m = $N$ with no excluded terms,

$$\sum_{m} T^{|m-n|-1} = T^{n-2} + T^{n-3} + \cdots + T^1 + T^0 + T^{-1} + T^0 + T^1 + \cdots T^{N-n-2} + T^{N-n-1} \tag{3.22}$$

$$\sum_{m} T^{|m-n|} = T^{n-1} + T^{n-2} + T^{n-3} + \cdots + T^1 + T^0 + T^1 + \cdots + T^{N-n-2} + T^{N-n-1} + T^{N-n} \tag{3.23}$$

And evaluate the full sum as follows,

$$\sum_{m}\left(T^{|m-n|-1} - T^{|m-n|}\right) = -T^{n-1} + T^{-1} + T^0 - T^{N-n} \tag{3.24}$$

This allows for simplification to obtain the final expression,

$$j_{\text{abs,n}} = j_{\text{bb}}(1 - T)[T^{n-1} + T^{N-n} - T^{-1} + T^0 - T^{n-1} + T^{-1} + T^0 - T^{N-n}] \tag{3.25}$$

$$\boldsymbol{j_{\text{abs,n}} = 2j_{\text{bb}}(1 - T) = j_{\text{rad,n}}} \tag{3.26}$$

Therefore, the system obeys microscopic reversibility for photon absorption and emission with the thermal bath.

### 3.2.4. Decoupled Models

There are two major differentiating features in the ensemble-based model used herein in comparison to a traditional single-absorber model. The first feature is that even though each light-absorber absorbs the same fraction of incoming solar photon flux, there is a

65

substantial decrease in $j_{\mathrm{ph}}$ values through the stack as the incident light on each light-absorber is progressively attenuated. This means that each light-absorber has a unique $j$–$V$ relationship, but the same electrochemical load curve, which has drastic effects on the total amount of net fuel production from the ensemble. The second feature is the presence of inter-absorber photon recycling that occurs when some of the radiative emission from one light-absorber is reabsorbed by the other light-absorbers in the stack. The extent of this effect is strongly influenced by the fraction of radiative recombination, $f_{\mathrm{c}}$. Because most absorbers have small values of $f_{\mathrm{c}}$,[92] and therefore emit few photons, it is important to study the $N$-absorber design without the effects of photon recycling, a condition that we term "decoupled."

Although this condition could be modeled in a straightforward manner by varying $f_{\mathrm{c}}$, doing so drastically effects the $j$–$V$ behavior of even the single-absorber case, making it difficult to specifically isolate the effect of reduced photon recycling. We therefore use a model with optically stacked absorbers and a baseline value of $f_{\mathrm{c}} = 1$, but where there is no radiative coupling between light-absorbers. In this decoupled model, the $j$–$V$ relationship for the light-absorbers is the standard photodiode equation but with $j_{\mathrm{ph,n}}$ unchanged from its form in Equation 3.2 as follows,

$$j_{\mathrm{n}} = q\Phi_0 A(1-A)^{n-1} + \frac{1}{f_{\mathrm{c}}}\left(1 - e^{qV_{\mathrm{n}}/kT}\right) \tag{3.27}$$

This represents the unrealistic physical situation where for absorption of solar photons, the absorbers are positioned optically in series but for absorption of all other photons, the absorbers are optically isolated and individually surrounded by blackbodies. However, this model effectively decouples the effects of photon recycling from all other elements of the

66

model and it is thus a useful tool for analyzing the effects of partial solar light absorption alone. In the decoupled model, which has a $j/V$ relationship dictated by the semiconductor photodiode equation, the expression for $V_{oc}$, assuming $f_c = 1$, is

$$V_{oc} = \frac{kT}{q} \log\left(\frac{j_{ph}}{j_{bb}} + 1\right) \tag{3.28}$$

and thus $V_{oc}$ is determined entirely by the ratio $j_{ph}/j_{bb}$.

### 3.2.5. Decoupled Models with Uniform Photon Absorption

Each light-absorber in the above model has the same optical thickness but a different incident solar photon flux and thus a different rate of photon absorption. The total STF efficiency depends on the sum of all $N$ operating current densities, and therefore, comparison of this value to the STF efficiency for the single-absorber case at the same total number of absorbed photons will determine whether having multiple light-absorbers is beneficial or detrimental. In many cases, the effect of having multiple light-absorbers is convoluted by opposing behaviors: certain light-absorbers in the stack exhibit large external quantum yields for generation of reaction products, and therefore utilize photons well, while other light-absorbers in the stack do not. Therefore, we also investigated conditions that remove the chance for opposing behavior by ensuring that each light-absorber in a multiple-light-absorber model absorbs the same number of incident solar photons. There are two distinct ways to accomplish this, depicted in Figure 3.2, which each utilize $N$ single light-absorbers, yet produce strikingly different results. In the *thick-absorber / 1/N Suns* model, each absorber is assumed to be as thick as in the single-absorber case with $\tau = 4.6$ and therefore each absorbs 99% of the incident light, and but the incident photon flux to each absorber is scaled by $N$, such that $\Phi_0 = \frac{\Phi_{0,AM1.5G}}{N}$. Physically,

this condition would be achieved by using optics to evenly split the solar radiation covering the area of a single absorber across $N$ different identical absorbers that are each thick enough to each absorb 99% of the split solar photon flux. In the *thin-absorber / 1 Sun* model, the incident photon flux remains at the 1 Sun intensity, $\Phi_0 = \Phi_{0,\text{AM1.5G}}$, but each absorber only absorbs $(^{99}/_N)$% of the light. Physically, this condition would be achieved by exposing $N$ identical optically thin light-absorbers to 1 Sun illumination. In each model, a total of 99% of the solar flux incident on the area of one absorber is absorbed by the $N$ absorbers, which is exactly the same condition used in the other models, where $N$ absorbers are stacked optically in series with $\tau_{\text{total}} = 4.6$. It is important to note that for these models the STF efficiency is still defined in terms of the solar flux incident on the area of a single light absorber in order to compare more effectively to the results of the other models. If the thin absorber scenario were actually fabricated, the true STF efficiency would be the value reported in this work divided by $N$.
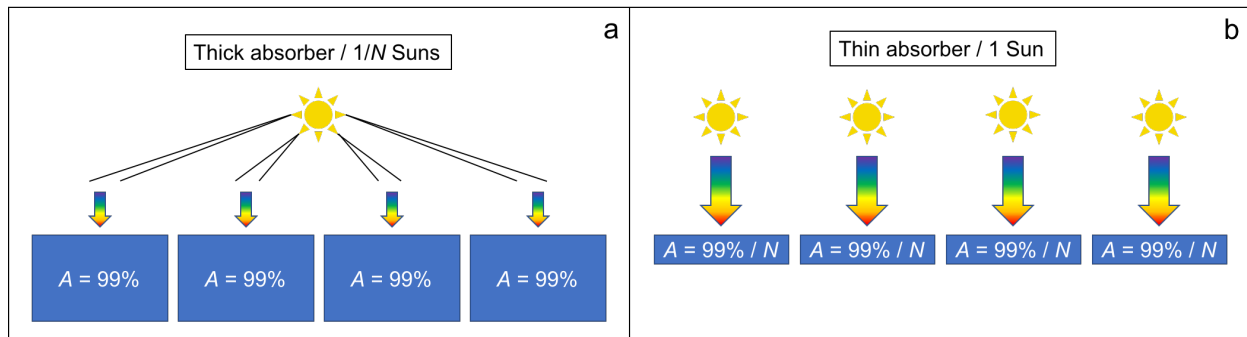


Figure 3.2. Schematic of decoupled models with uniform photon absorption: (a) thick-absorber / 1/$N$ Suns model and (b) thin-absorber / 1 Sun model.

## 3.3.    Results and Discussion

Figure 3.3a shows STF efficiency *vs.* $E_g$ for a range of values of $N$ while Figure 3.3b shows the enhancement in STF efficiency relative to the case when $N = 1$. Over the range of $E_g =$

1.6 – 2.0 eV, the STF efficiency increases logarithmically as a function of $N$ and the maximum STF efficiency occurs for smaller bandgaps. This means that incident photons are better utilized when multiple small-bandgap absorbers are present. To understand this behavior, we first briefly explain the cause of the shape of the $N = 1$ data. The STF efficiency is directly dependent on the operating current. However, to provide any current density in the fuel-forming direction, the absorber must generate an open-circuit potential ($V_{oc}$) that exceeds the thermodynamic potential of the fuel-forming reactions. To drive water electrolysis at room temperature and standard state conditions, which requires $V_{oc}$ > 1.23 V, the minimum bandgap energy for a single absorber with the baseline parameters shown in Table 1 is $E_g$ = 1.52 eV. For bandgap energies between 1.52 eV and the maximum STF efficiency value of 1.93 eV, the absorber can generate enough potential to drive the reactions, but the Butler–Volmer relationships limit the operating potential to values close to $V_{oc}$, such that a substantial amount of excited charge carriers recombines. In this case the light-absorber is *potential-limited*. Beyond 1.93 eV, the light-absorber generates enough potential that it operates very close to its maximum operating current density, which is dictated by the absorbed solar photon flux, $j_{ph}$. In this case the light-absorber is *current-limited*, and every increase in the energy of the bandgap results in fewer absorbed photons and therefore a lower operating current density.
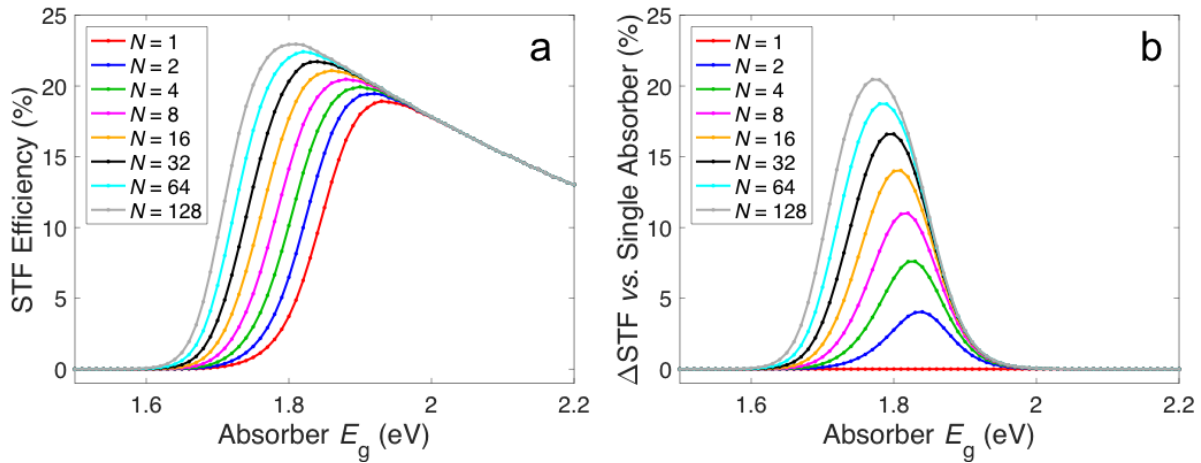
Figure 3.3. STF efficiency *vs.* bandgap as a function of the number of light-absorbers, *N*. (b) Difference in STF efficiency (from the *N* = 1 case) *vs.* bandgap for the same range of values for *N*.

The improvement in STF efficiency caused by using multiple light-absorbers ($N > 1$) *vs.* a single light-absorber ($N = 1$), which Figure 3.3b shows only occurs in the potential-limited regime, is caused by a convolution of two effects. The first effect is photon recycling; when the operating current density of one light-absorber is less than $j_{ph}$, a fraction $f_c$ of the difference in current density between $j$ and $j_{ph}$ is reemitted. The other absorbers in the stack are able to reabsorb this radiation and thus the percent of incident photons on the ensemble that are ultimately utilized for chemical reactions increases. The closer the operating potential is to $V_{OC}$, the more photons are reemitted, and therefore the largest increase in STF efficiency from photon recycling occurs at lower bandgap energies.

The other beneficial effect of having multiple light-absorbers is due to the changes in the individual photodiode curves caused by optical thinning. The improvements in STF efficiency are due to a convolution of partial solar light absorption by each absorber in the stack and the relative shapes and locations of the semiconductor photodiode *j–V* relationships (power curves) and electrocatalytic Butler–Volmer *j–V* relationship (load

70

curve). When the thickness of each of the $N$ light-absorbers is the same, the absorptance of each absorber is the same but $j_{ph}$ for each absorber differs due to different light intensities incident on each of the absorbers. This in turn causes each of their power curves to be different. Quantum efficiency for a given light-absorber is improved when its power curve intersects the load curve such that the ratio between the operating current and the absorbed photon flux, defined as $j_{ratio,n} = j_n/j_{ph,n}$, is larger than $j_{ratio}$ for the single light-absorber case. STF efficiency is improved when all or most of the light-absorbers have improved $j_{ratio,n}$, resulting in a larger total operating current density from the $N$ light-absorbers. Because the rate-limiting recombination flux has the same dependence on optical thickness as sunlight absorption, optical thinning decreases $j_{ph}$ and $j_{bb}$ by the same factor. This means that neglecting photon recycling, the $V_{OC}$ of the first absorber is independent of the amount of light it absorbs and therefore independent of $N$ by Equation 3.14. Thus as $N$ increases, $j_{ratio,1}$ increases because the power and load curves intersect at potentials successively further from $V_{OC}$ and current densities successively closer to $j_{ph}$. For subsequent light absorbers, light attenuation causes $j_{ph}$ to exponentially decrease while $j_{bb}$ is the same as $j_{bb}$ of the top absorber, meaning $V_{OC}$ decreases logarithmically with n. $j_{ratio,n}$ is only improved in light-absorbers 2-$N$ if the curvature of the load curve is sufficiently small relative to the logarithmic decrease in $V_{oc}$, i.e. that catalysis is slow, as depicted in Figure 3.4. The slower the catalysis, the greater the increase in STF efficiency with respect to $N$. This trend can be clearly seen in iterations of Figure 3.3a with varied values of exchange current density and varied values of charge transfer coefficient, which are presented in Figure 3.5 and Figure 3.6, respectively.
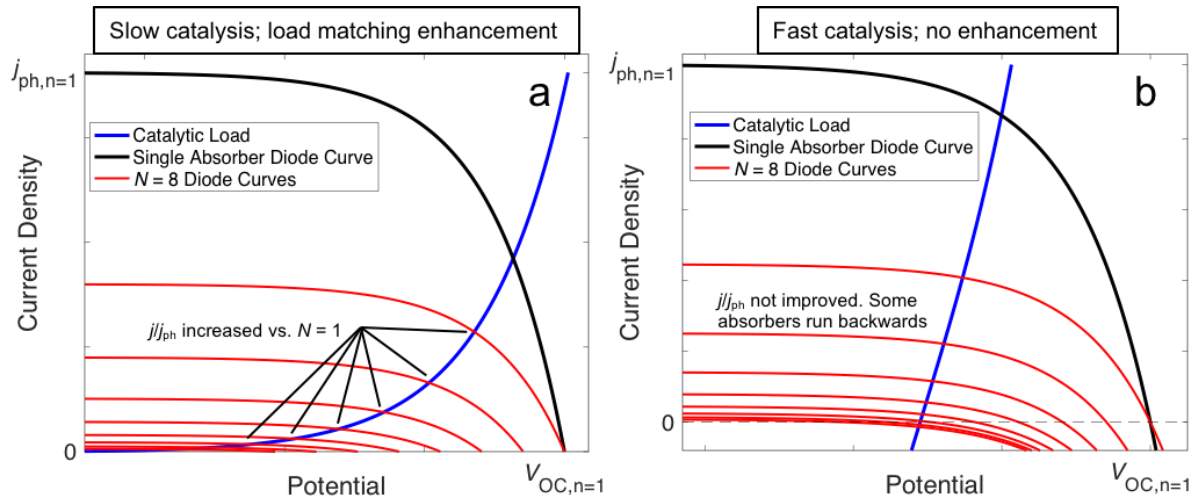
Figure 3.4. Examples of load curves where load matching enhancement occurs (a) and where load matching does not occur (b). $N = 8$ case selected for easiest visualization.
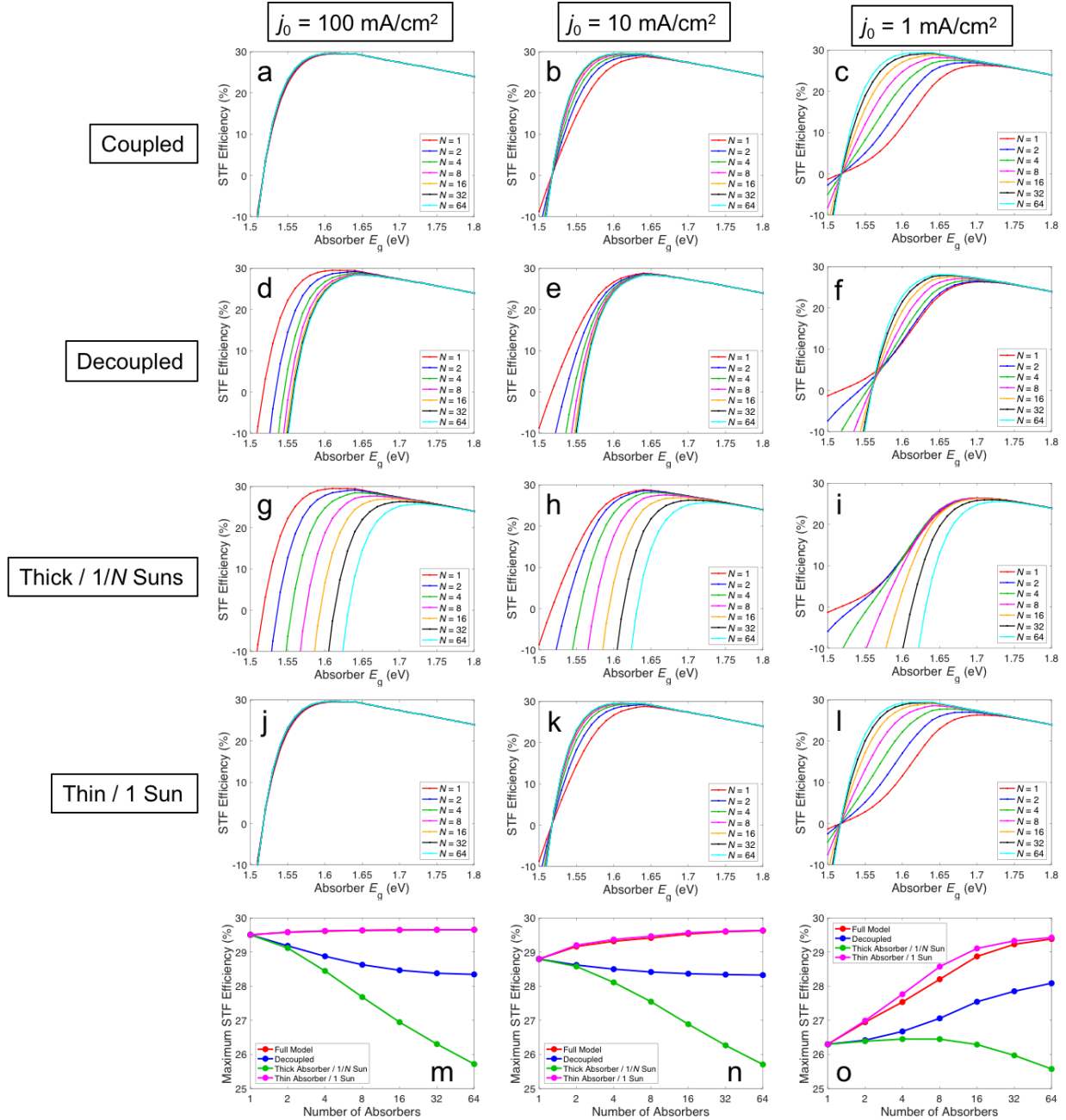
Figure 3.5. STF Efficiency *vs.* bandgap for different values of *N* in the (a, b, c) coupled and (d, e, f) decoupled models, with exchange current density for both reactions set to (a, d) 1, (b, e) 10, and (c, f) 100 mA/cm². (g) Maximum STF efficiency *vs. N* on a base 2 logarithmic scale for all cases.
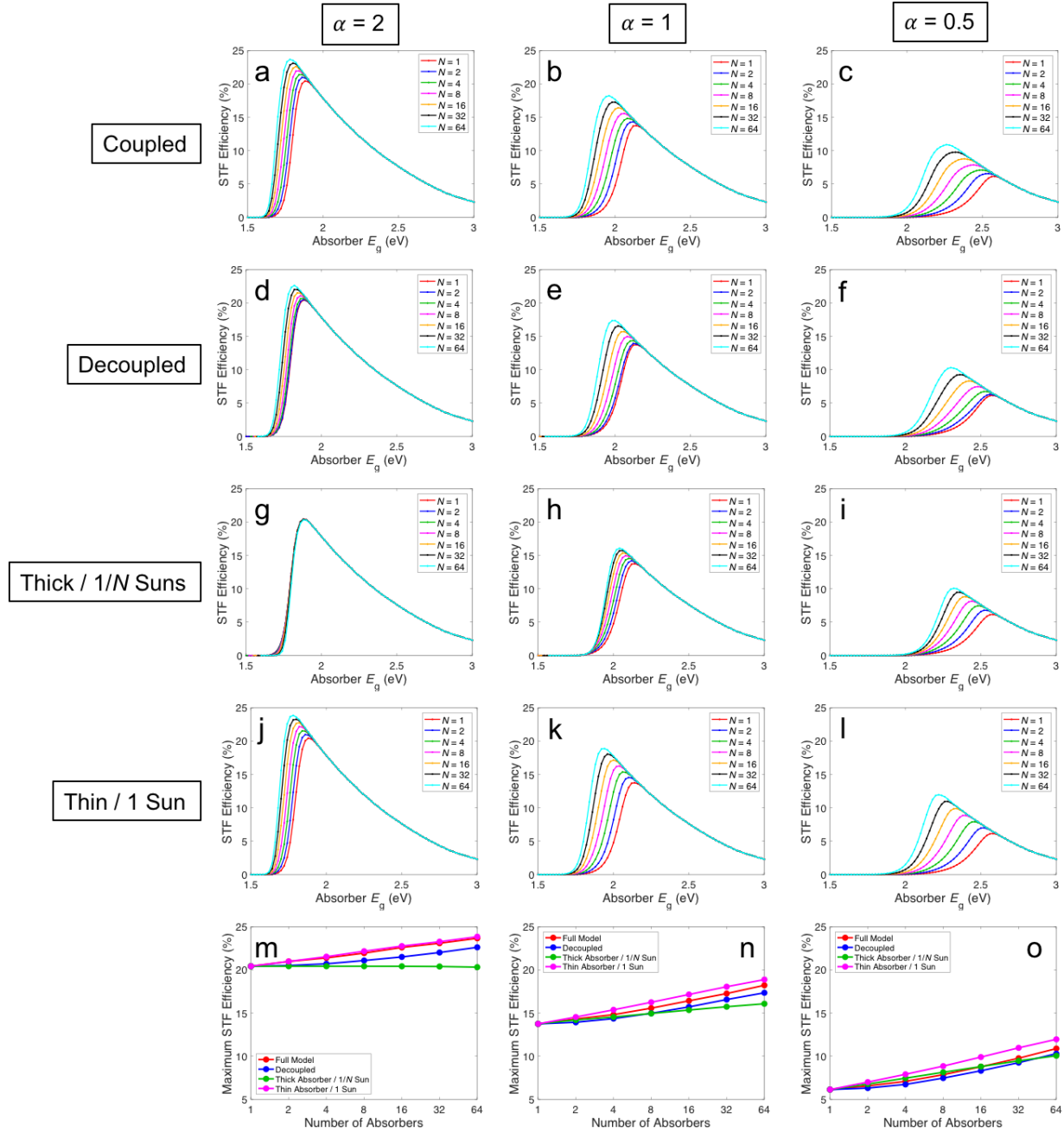
Figure 3.6. STF Efficiency *vs.* bandgap for different values of *N* in the coupled models, with charge transfer coefficient for all reactions set to (a) 2.0, (b) 1.0, and (c) 0.5. (d) Maximum STF efficiency *vs. N* on a base 2 logarithmic scale for all cases.

By studying the decoupled model, which removes the effects of photon recycling, we

can specifically analyze the effect of optical thinning. Figure 3.7a shows the efficiency *vs.*

bandgap energy, Figure 3.7b shows the difference between the coupled model efficiency

and the decoupled model for each $N$ as a function of the energy of the bandgap, and Figure 3.7c shows the maximum STF efficiency for both models *vs. N* on a base 2 logarithmic scale. Because the treatment of solar photons in the decoupled model is identical to the full model but the diode behavior of each absorber in the decoupled model resembles that of an isolated absorber, the increase in STF efficiency for multiple absorbers seen in the decoupled model is singularly a result of optical thinning. The increase in STF efficiency in Figure 3.7b is then specifically due to photon recycling. Photon recycling has the most impact at bandgap energies slightly lower than the value that maximizes STF efficiency for each value of $N$. This is because these conditions are in the potential-limited regime where radiative recombination fluxes are large. Increases is STF efficiency from both photon recycling and optical thinning only occur in this model because the efficiency for a fuel-forming device is dependent on only the device current, not the product of current and potential like in a solar cell. This is illustrated in Figure 3.8, which shows analogs of Figure 3.3a and Figure 3.7a, but where the operating current density and potential are chosen as the point that maximizes power density, ignoring the constraints from the electrocatalytic Equations 3.9–3.11. Figure 3.8 reports the power conversion efficiency, which is the figure-of-merit for a solar cell and is optimum at small $N$.
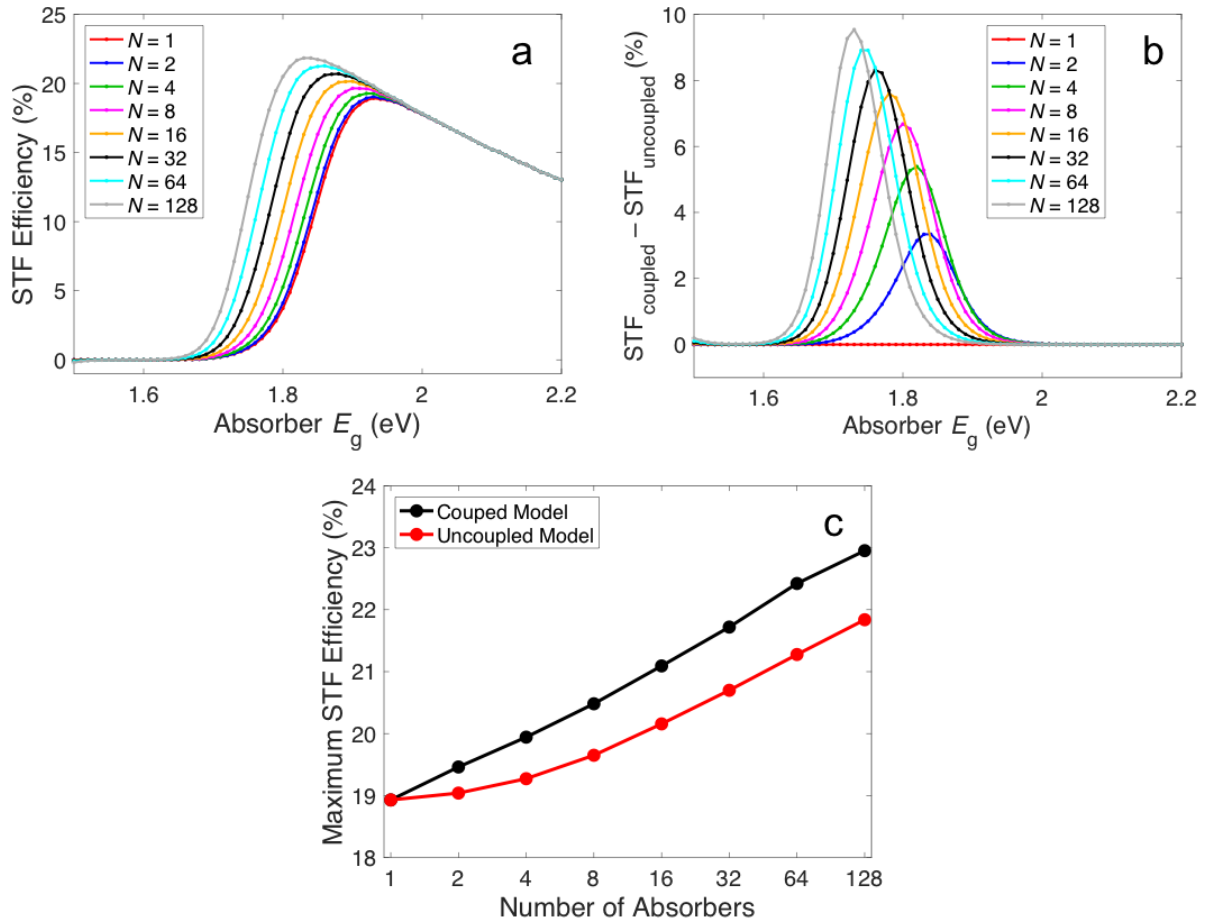
Figure 3.7. STF efficiency (in the absence of photon recycling) *vs.* bandgap as a function of the number of light-absorbers, *N*. (b) Difference in STF efficiency (in the presence minus absence of photon recycling) *vs.* bandgap for the same range of values for *N*. (c) Maximum STF efficiency (in the presence and absence of photon recycling) *vs.* *N* on a base 2 logarithmic scale.
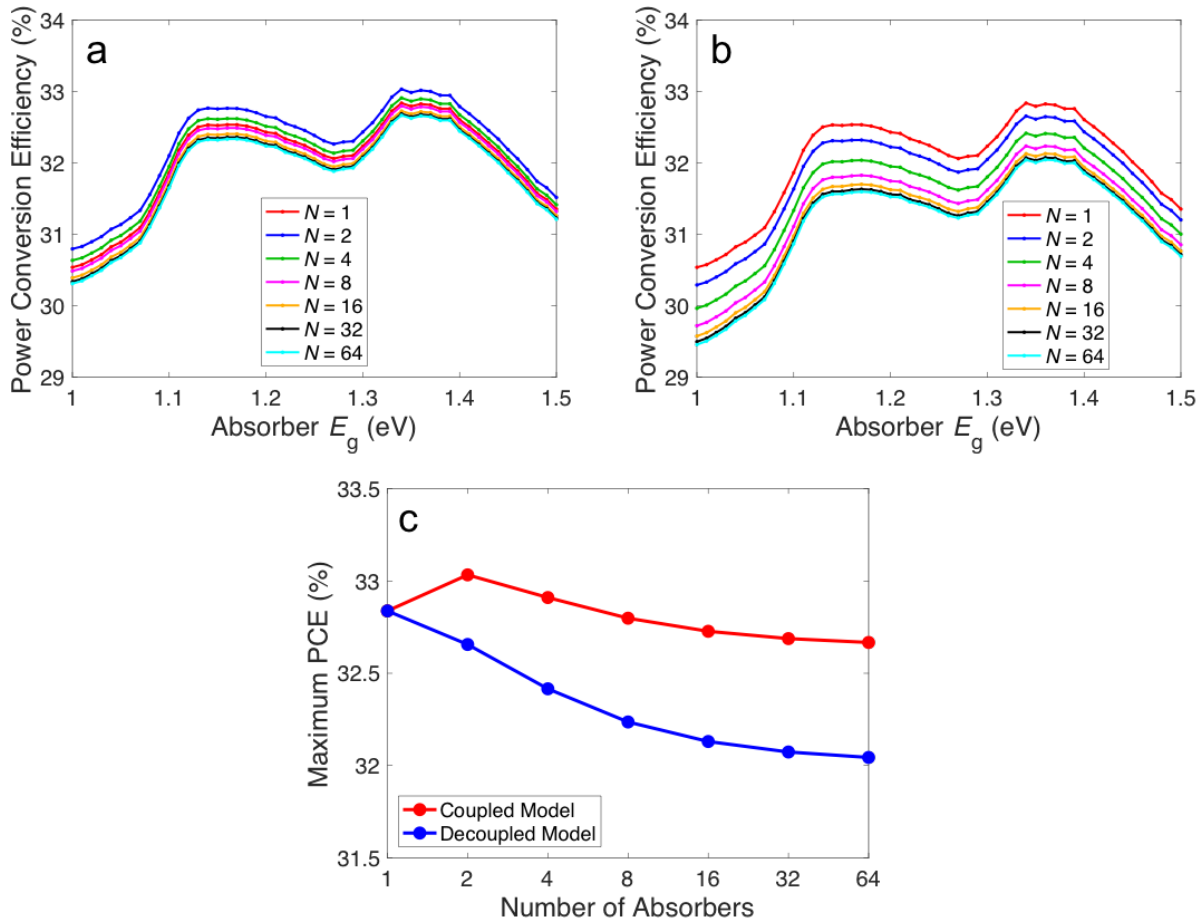
Figure 3.8. Power conversion efficiency (PCE) *vs.* bandgap for (a) coupled and (b) decoupled models where each operating current and voltage is selected at the point that maximizes power. (c) Maximum PCE *vs. N* on a base 2 logarithmic scale for both cases.

The effect of optical thinning on STF efficiency has a complex dependence on numerous absorption and electrocatalytic system parameters and the extent to which it contributes to improved STF efficiency varies for each value of $E_g$, *N*, and n. In order to visualize this complex dependence, Figure 3.9 presents maps for $N = 128$ of various current density terms *vs.* n and $E_g$ for both the coupled and decoupled models. The current densities represent those due to absorption of blackbody photons from other absorbers (Figure 3.9a; coupled model), absorption of incident solar photons only (Figure 3.9d), radiative

recombination when $f_c = 1$ (Figure 3.9b, e), and net operating current density (Figure 3.9c, f). Comparing the three maps generated using the coupled model (Figure 3.9a, b, c) it is apparent that at low bandgap energies, large rates of photon recycling are almost completely negated by equally large rates of radiative recombination. Only at bandgap energies in a narrow range near 1.75 eV does photon recycling have a net beneficial effect, which is in agreement with Figure 3.7b. All data in Figure 3.9 indicate that almost all of the fuel-forming current density is provided by the top half of the light-absorbers in the stack. This makes sense because the top half of the stack absorbs 90% of the incident light, while the bottom half of the stack absorbs only 9%. In cases where many of the bottom light-absorbers perform the undesired back-reaction, optimization of the STF efficiency occurs when the bottom half of the absorbers are removed, without changing the top half. While this sacrifices small amounts of additional light absorption, it provides a net benefit by eliminating the portion of the stack that net performs the undesired back-reaction.
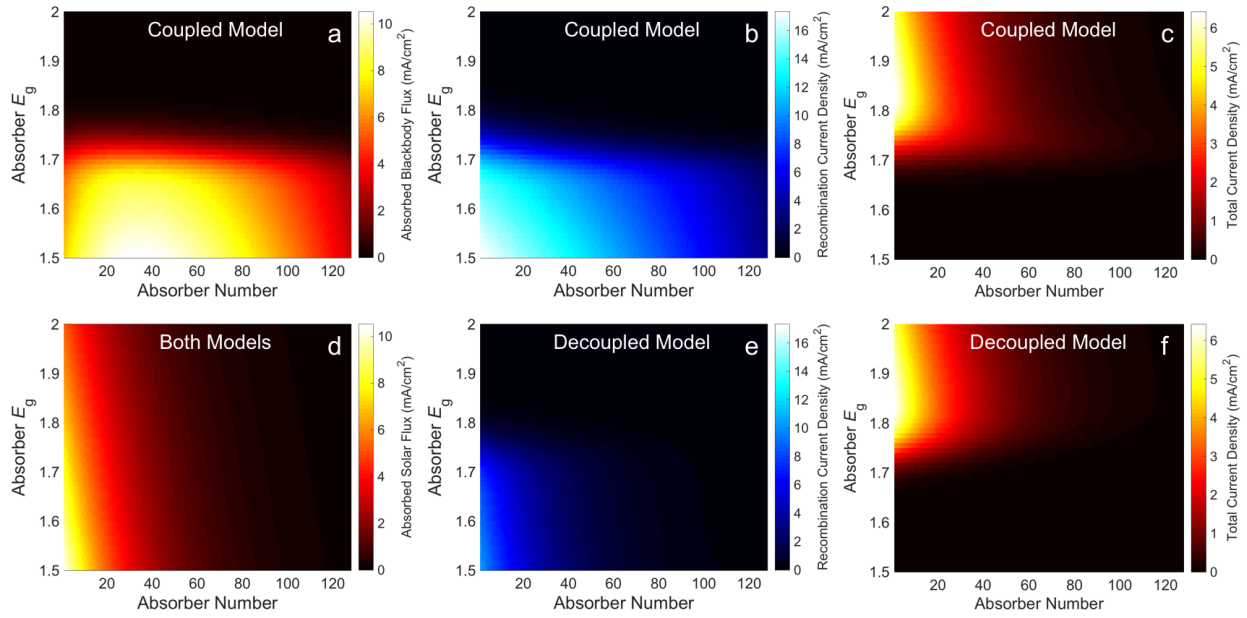
Figure 3.9. Maps of current density values as a function of bandgap and light-absorber number for the coupled model: (a) absorbed blackbody flux from neighboring light-absorbers, (b) radiative recombination flux, and (c) net current density; for both models: (d) absorbed incident solar flux; and for the decoupled model: (e) radiative recombination flux and (f) net current density.

It is clear from the results of the decoupled model with baseline parameters (Figure 3.7b, c) that optical thinning causes the maximum STF efficiency to increase logarithmically with $N$ when electrocatalysis is suitably slow. The root cause of this relationship is the suppression of dark current; detailed balance dictates that an optically thin absorber has a lower reverse saturation current density (Equations 3.4 and 3.7) so despite absorbing less incident light, the first absorber in the ensemble has the same $V_{OC}$ as a single absorber that absorbers 99% of the incident light. This phenomenon of a $V_{OC}$ that is independent of optical thickness has been demonstrated theoretically and experimentally.[93–96] As n increases, fewer photons are present for absorption, which means that $j_{ph}$ is reduced. This would be beneficial if $V_{OC}$ was unchanged because the power and load curves would intersect at a current density close to $j_{ph}$, resulting in higher $j_{ratio,n}$. However, the value of $j_{bb}$

is independent of n and therefore as n increases, $V_{oc}$ decreases which causes the power and load curves to intersect at a lower current density and eventually causes some absorbers to operate in reverse. The net effect obscures this tradeoff. Therefore, we introduce decoupled models with uniform photon absorption to independently explore these processes in more detail.

Figure 3.10, b show results from the thick-absorber / $1/N$ sun model and thin-absorber / 1 sun model, respectively, and Figure 3.10c shows the comparison of the maximum STF efficiency between these two models and the standard decoupled model (same data as red trace in Figure 3.7c). The thin-absorber model is slimilar to the case where bulk or radiative recombination limits performance because reverse saturation current density scales with $j_{ph}$; the data exhibits the same trend of improved maximum STF efficiency with increasing $N$ as the standard decoupled model, but with an even larger magnitude of improvement. The thick-absorber model is similar to the case where surface recombination limits performance because reverse saturation current density is independent from $j_{ph}$; the data shows almost no change as $N$ is varied.[42] The difference between these two seemly similar models is due to how $j_{ph}$ and $V_{oc}$ change with respect to $N$. In the thin-absorber model, $j_{ph,N>1} = \frac{j_{ph,N=1}}{N}$ and $j_{bb,N>1} = \frac{j_{bb,N=1}}{N}$ meaning $j_{ph}/j_{bb}$ and thus $V_{oc}$ is the same for all $N$. Every absorber in this model has suppressed dark current but is also exposed to one sun, so every absorber behaves like the first absorber in the full model, with $V_{OC}$ equal to the single absorber $V_{OC}$. As $N$ increases, the progressively lower value of $j_{ph}$ and unchanged value of $V_{oc}$ ensure that $j_{ratio}$ continuously increases. In the thick-absorber model, $j_{ph,N>1} = \frac{j_{ph,N=1}}{N}$ while $j_{bb,N>1} = j_{bb,N=1}$, and thus both $j_{ph}$ and $V_{oc}$ decrease.

The absorbers in this model have the same dark current as the single absorber but absorb less light due to lower incident light per absorber. Load matching enhancement occurs when an absorber has a low absorptance but a high incident photon flux, which results in a large $V_{OC}$ and a small $j_{ph}$; this is the case in the thin-absorber model while the opposite is the case in the thick-absorber model. The behavior of $j_{ph}$ and $V_{oc}$ in the two models elucidates the balance that determines why STF efficiency increases with respect to $N$ in the full models. Optical thinning causes the first absorber to have the same $V_{OC}$ and lower $j_{ph}$ than the single absorber, guaranteeing improved $j_{ratio,1}$ in the potential-limited regime. This improvement occurs for each absorber in the thin absorber / 1 Sun model. For subsequent absorbers, changing n causes $j_{ph}$ and $V_{oc}$ scale with the same functional relationship as $j$ and $\eta_{ox/red}$ in the Butler–Volmer equation (Equations 3.9 and 3.10). This scaling relationship is captured in the thick absorber / 1/$N$ Suns model, but the scaling occurs with changing $N$, not n. In the full models, every absorber in the stack exhibits improved $j_{ratio.n}$ as long as electrocatalysis is slow enough, i.e. that the two exchange current densities and four charge transfer coefficients are low enough that the slope of the load curve is sufficiently small, until the limiting case when $V_{oc}$ is less than $E_0$. Even in the case of faster electrocatalysis where eventually the bottom portion of the stack does not operate more efficiently than a single absorber, the top portion, which absorbs the majority of the incident light, performs so much more efficiently that the net result is enhanced STF efficiency over the single-absorber case. This is elucidated in Figures Figure 3.5 and Figure 3.6, which show that the electrocatalytic exchange current density for both reactions must approach 100 mA/cm$^2$ for multiple absorbers to perform worse than a single absorber in

81

the decoupled model and can exceed 1000 mA/cm² without multiple absorbers performing worse in the coupled model, while STF efficiency is still improved in both models with charge transfer coefficients as high as 2.
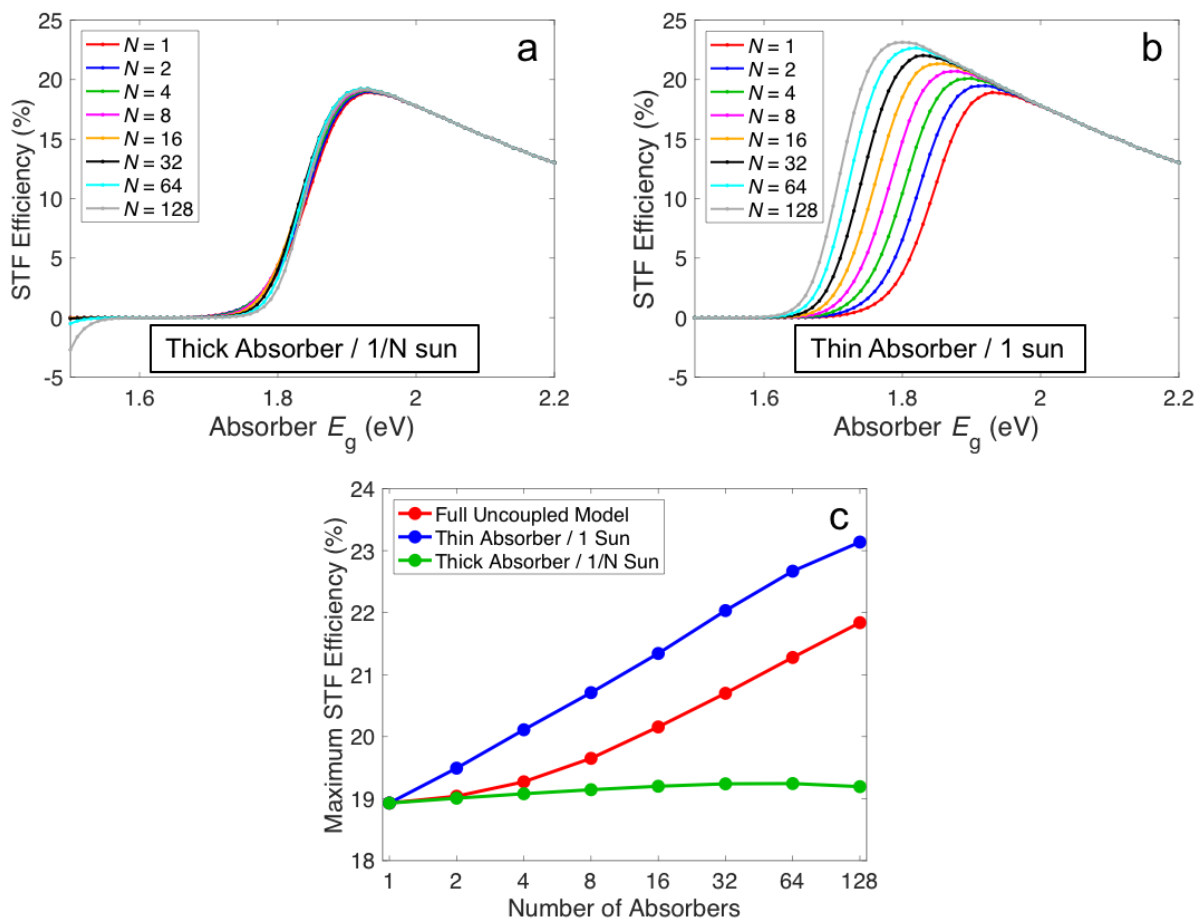


Figure 3.10. STF efficiency *vs.* bandgap as a function of the number of light-absorbers, *N* for (a) the thick-absorber / 1/*N* Sun model and (b) the thin-absorber / 1 Sun model. (c) Maximum STF efficiency *vs. N* on a base 2 logarithmic scale.

The results of the decoupled models with uniform photon absorption show that in the full models, where all absorbers have the same optical thickness, the top absorber will have the same $V_{oc}$ as a single absorber, in the absence of photon recycling, and as incident light is attenuated, $V_{oc}$ from each light-absorber will decrease as it is located deeper in the

stack. This means that the top light-absorbers will have the most improved performance while the bottom light-absorbers will have the least improved performance, and may possibly perform worse, compared to a single light-absorber. By analyzing the current density of each absorber in a stack, we can quantify how this performance changes within a stack using $j_{ratio,n}$ (equal to $j_n$ /$j_{ph,n}$). $j_{ratio,n}$ is very closely related to external quantum efficiency; it differs because the denominator is only the total absorbed solar photons and does not count recycled photons. If $j_{ratio,n}$ for a light-absorber in the stack is higher than $j_{ratio}$ for the single-absorber case, then that light-absorber contributes to overall larger STF efficiency. Figure 3.11a, b show maps of $j_{ratio,n}$ as a function of n and $E_g$ for the coupled and decoupled models, respectively, using baseline parameters shown in Table 1 and $N = 128$. The regions below and to the right of the green line are regions where $j_{ratio,n}$ is lower than $j_{ratio}$ for the single light-absorber. Remarkably, this only occurs when the operating current density is very close to or smaller than zero, i.e. where the light-absorber operates in reverse. At all substantial values of $j$, all absorbers in the stack outperform the single absorber for the baseline electrocatalytic parameters used. In the coupled model, $j_{ratio,n}$ can exceed 1 because of photon recycling. This occurs most substantially for light-absorbers deeper in the stack because $j_{ph}$ is so small for these light-absorbers that small changes in the number incident photons have large impacts on the operating current density.

83
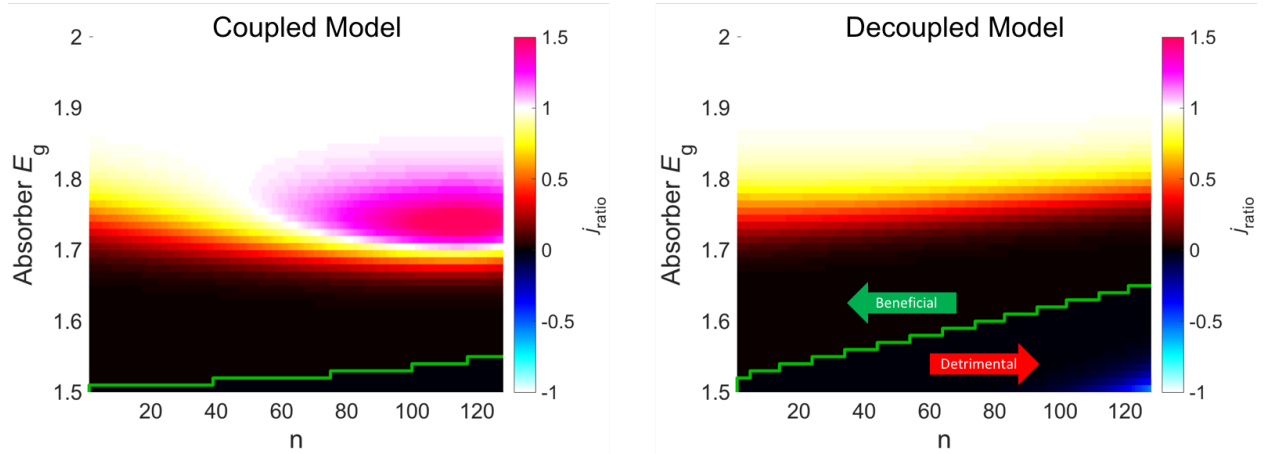
Figure 3.11. Maps of $J_{ratio}$ *vs.* absorber number and bandgap with $N = 128$ for (a) the coupled model and (b) the decoupled model. Green line indicates the division between absorbers which have $J_{ratio}$ higher (left and above) and lower (right and below) than $J_{ratio}$ for the single absorber.

Figure 3.12 shows iterations of Figure 3.11 with higher values of exchange current density ranging from 0.1 – 100 mA/cm². As $j_0$ increases, the number of absorbers that perform worse that the $N = 1$ increases, and the magnitudes of the negative $j_{ratio,n}$ values drastically increase, once again demonstrating that large $N$ has the most benefit when catalysis is slow.

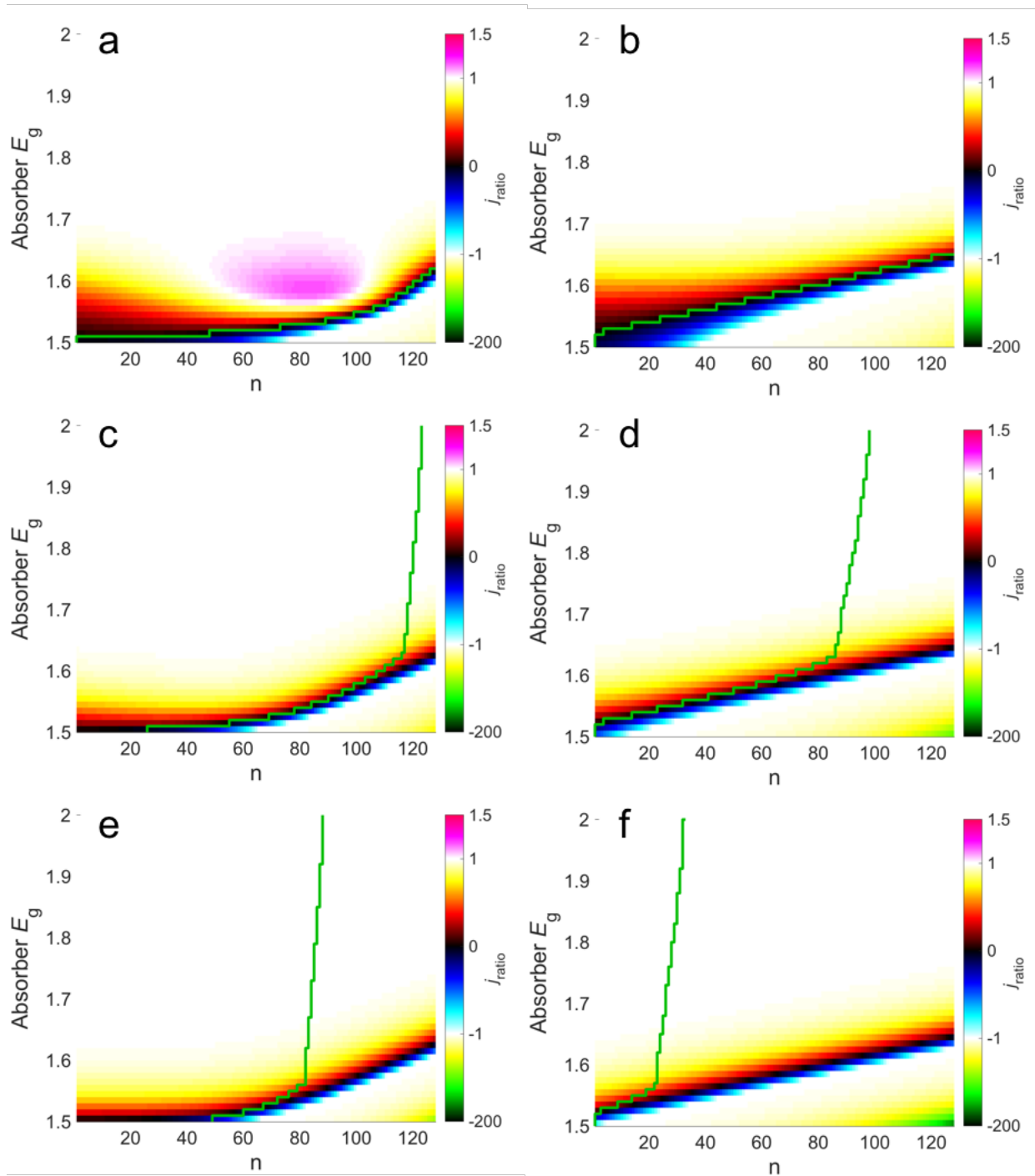Figure 3.12. Maps of $J_{ratio}$ *vs.* absorber number and bandgap with $N$ = 128 for (a, c, e) the coupled model and (b, d, f) the decoupled model with exchange current density for both reactions set to 0.1 (a, b), 1 (c, d), and 10 (e, f) mA/cm². Green line indicates the division between absorbers which have $J_{ratio}$ higher (left and above) and lower (right and below) than $J_{ratio}$ for the single absorber.

The maximum STF efficiency for water electrolysis under standard-state conditions at room temperature and assuming no catalytic overpotentials (infinite exchange current density), is 30.6%,[46] while the maximum efficiency using state-of-the-art electrocatalytic parameters is in the range of 15 – 20% depending on the exact model parameters chosen. The large discrepancy is mainly due to the poor catalysis of the OER, which has been an active area of research of over half-a-century[79–81]. However, even in the absence of any breakthroughs in the rate of OER electrocatalysis, we have shown that utilizing multiple light-absorbers can effectively overcome limitations imposed by this slow rate of OER electrocatalysis. This leads to a shift in the STF efficiency toward its maximum theoretical value and therefore, represents a promising way to develop high-efficiency water electrolysis devices.

The fraction of radiative recombination, $f_c$, is one of the most important parameters in determining the maximum efficiency of a solar fuels device. Figure 3.13 shows STF efficiency vs. bandgap energy for varied $N$ in the coupled model with $f_c$ varied in two ways. In the left-hand plots (a, c, e, g), a value of $f_c$ is chosen and kept constant for all N. This models the case where the nonradiative recombination process occurs in the bulk of the material and thus radiative and nonradiative recombination scale equally with distance. In the right-hand plots (b, d, f, h), a value of $f_c$ is chosen for the $N = 1$ case, which by Equation 3.7 determines the nonradiative reverse saturation current density, $j_{0,\mathrm{NR}}$,

$$j_{0,\mathrm{NR}} = 2j_{\mathrm{bb}}A\left(\frac{1}{f_c} - 1\right) \tag{3.29}$$

This value of $j_{0,NR}$ is then used for all subsequent $N$, which effectively decreases $f_c$ with increasing $N$. This models the case where the nonradiative recombination process is a surface phenomenon that does not change with the thickness of the light absorber.

The maximum STF efficiencies for all $N$ clearly scale logarithmically with $f_c$. The magnitude of improvement in STF efficiency for successively larger $N$ is unchanged when the bulk recombination model is used, while there is no improvement when the surface recombination model is used. Thus, while larger $f_c$ is always desirable, the benefits of large $N$ are seen for high rates of bulk nonradiative recombination. State-of-the-art GaAs solar cells[97] and solution-processed organic–inorganic hybrid perovskite solar cells[98] have achieved nearly unity values of $f_c$. However, for widely studied solar cell materials there is a range of values for $f_c$ that span over ten orders-of magnitude.[92] In particular, devices that incorporate nanomaterials typically have low values of $f_c$ because of the dramatic increase in the number of surface trap states due to the presence of large surface areas,[99] although radiative recombination fractions on the order of $3 \times 10^{-4}$ have recently been reported for inorganic perovskite quantum dot solar cells.[100] Additionally, most trap states in these devices arise from the need to cast the quantum dots into electronically coupled thin films; colloidal suspensions of numerous types of quantum dots exhibit extremely high photoluminescence yields. These quantum dots can be prepared using low-cost, facile synthesis methods with bandgaps easily tunable within the ranges of optimal STF efficiency over a wide range of $N$ and $f_c$[101–103]. If water-stable colloidal suspensions of these quantum dots could be prepared with ligands that performed solar fuels catalysis, they would be direct manifestations of the model presented here with extremely high $N$.

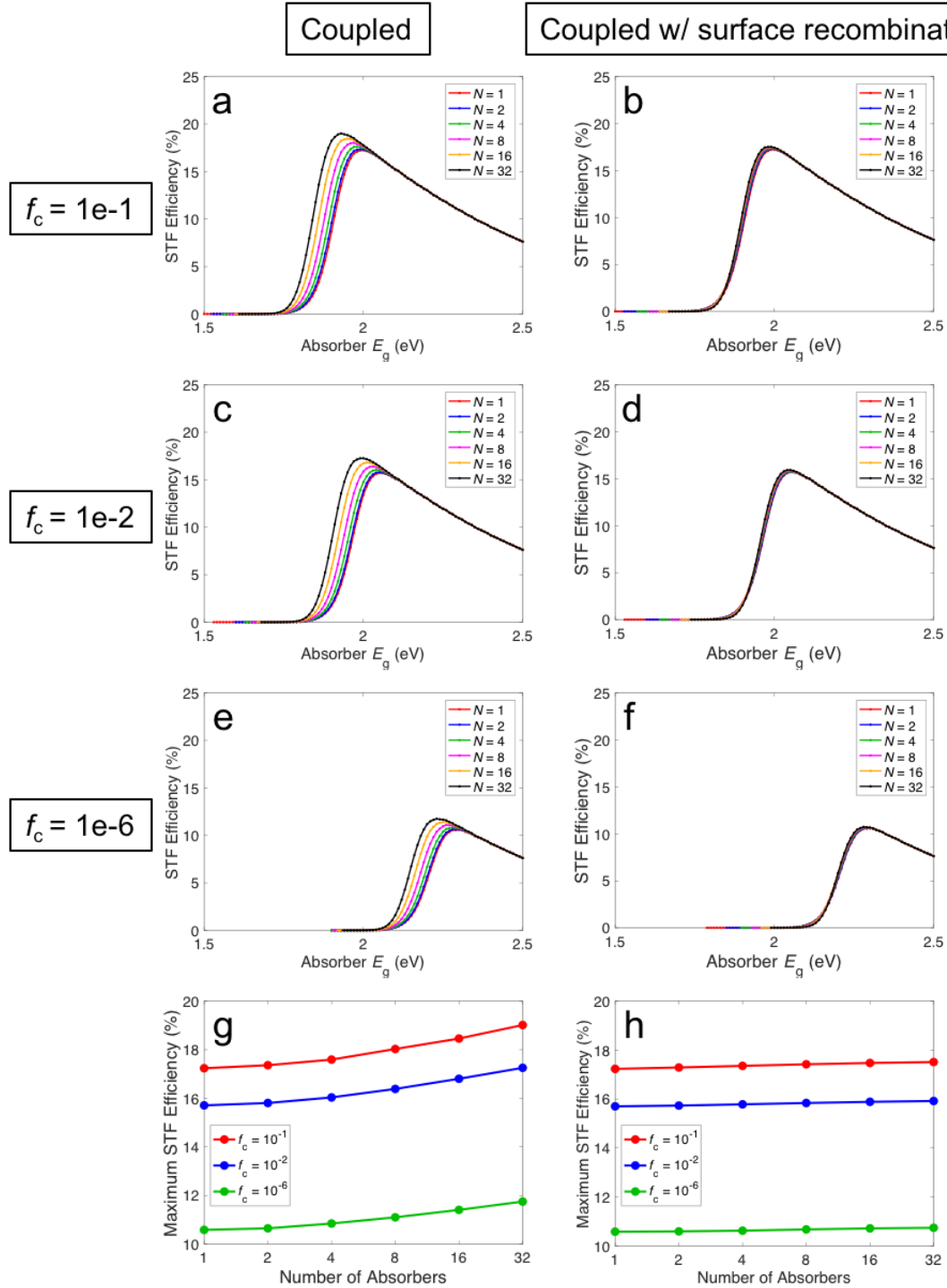Figure 3.13. STF efficiency *vs.* bandgap for the coupled model with radiative recombination fraction ($f_c$) equal for all $N$ to (a) 1e-1, (c) 1e-2, and (e) 1e-6, and for $f_c$ in the $N = 1$ case equal to (b) 1e-1, (d) 1e-2, and (f) 1e-6 and $j_{0,NR}$ kept constant for all subsequent N. Maximum STF efficiency *vs.* $N$ on a base 2 logarithmic scale for (g) the constant $f_c$ case and (h) the constant $j_{0,NR}$ case.

Hybrid organic–inorganic halide perovskite materials, which are grown using low-temperature, solution-processed techniques, have been used as the light-absorber in solar cells with > 20% PV efficiency[104] and tandem solar water-electrolysis devices with > 12 % STF efficiency[26]. While the most efficient perovskite materials have bandgap energies that are slightly too small to drive water electrolysis and related solar fuels reactions at large rates, their bandgap energies are highly tunable in the range of 1.5 – 2.3 eV via partial substitution with $Br^-$ for $I^-$.[105] Moreover, these materials have been reported to have $f_c$ values that range from near unity[98] to several orders-of-magnitude below unity, both conditions that would result in large gains in STF efficiency by increasing $N$. This is accomplished by decreasing the film thickness, which is facile with the solution-processed techniques used to fabricate these materials. Assuming that issues of materials water instability can be overcome and/or surfaces can be protected, this represents a direct pathway to a single-material, low-cost, high-efficiency solar-to-fuel device.

There are several demonstrations of solar water-electrolysis devices that already utilize numerous optically thin absorbers. One of the most successful is the photocatalyst sheet developed by the Domen group.[83–85] These devices utilize porous sheets of photocatalyst nanoparticles that independently perform water electrolysis due to negligible charge transport between particles. While coevolution of $H_2$ and $O_2$ gases presents an explosive mixture, recent work suggests that via engineering controls, explosion hazards can be mitigated[85]. This configuration is directly applicable to the models presented herein because it is a system of optically thin light-absorbers in optical series that independently perform solar fuels reactions. The challenge for these devices is

to develop electrocatalytically active materials with smaller bandgaps, because most of the materials studied so far are well within the current-limited regime due to their large bandgap energies,[42] meaning that there is no benefit to having multiple light-absorbers. Experimentally this condition has been shown by the linear dependence on the rate of $H_2$ production on excitation light intensity.[85] Another similar device is the Z-scheme particle suspension reactor, which we have modeled extensively[31] and contains two types of photocatalyst nanoparticles that exchange charge via a redox shuttle. Similar to the photocatalyst sheets, most Z-scheme materials studied thus far have had bandgap energies that are too large[42] to benefit from having multiple thin light-absorbers. The ideal material would have a tunable particle size, tunable direct bandgap, large quantum yield for emission, and be stable in an aqueous environment.

Another means to increase the STF efficiency is to increase the surface area for electrocatalysis. In the ideal case, the resulting effect on STF efficiency is the same as for the decoupled thin-absorber case but does not require that recombination be bulk or radiative limited. However, there are benefits to using multiple light-absorbers instead of simply increasing loading of the electrocatalysts. Many electrocatalysts absorb light and so minimizing the total electrocatalyst thickness is critical to obtaining large STF efficiencies. The largest surface-area to volume ratio is obtained by coating semiconductor surfaces in monolayers of electrocatalysts. This can be accomplished in photocatalyst designs using facile photochemical deposition routes,[42] while it is not possible for single light-absorbers without substantially increasing the mass loading required for porosity and therefore optical absorption. Particles are also beneficial because they each operate at small currents

and therefore have lesser issues with species mass transport, are themselves mobile and have better access to reactants and products due to lack of a mesoporous electrode where forced convection within the pores is difficult. Moreover, their small size facilitates rapid charge separation and their large surface-area-to-volume ratios mean little electrocatalyst must be present, which can lead to beneficial effects due to pinch-off.

## 3.4.    Conclusions

We have developed a novel model to show that through photon recycling and load matching enhancement, an ensemble of optically stacked thin light-absorbers can have substantially increased solar-to-fuels efficiency when compared to a single absorber. Poor catalysis, which has been one of the major barriers to solar fuels applications such as water electrolysis, can be overcome by selecting a large number of absorbers with the correct bandgap. The results of this model show that there are promising avenues to explore using materials and devices with low processing costs, such as perovskite solar cells, photocatalyst sheets, and particle suspension reactors.

# Conclusion

Models are based on the thermodynamic principles of detailed balance and blackbody radiation, semiconductor device physics, and simple catalysis were used to calculate the maximum theoretical solar-to-fuel efficiencies of novel solar fuels devices. They demonstrated the substantial benefits of using a system of photocatalyst particles or other optically thin light-absorbers to perform solar fuels reactions over traditional monolithic light-absorbers. The importance of the redox shuttle thermodynamic potential and other catalytic parameters when implementing these light-absorbers in an electrochemically-mediated tandem system was also demonstrated. This work will allow future researchers to develop solar fuels devices that have the potential to be economically viable on a large scale.

# Bibliography

1       *IPCC, Contribution of Working Groups I, II and III to the Fifth Assessment Report of the Intergovernmental Panel on Climate Change*, Geneva, Switzerland, 2014.

2       *A Report by the APS Panel on Public Affairs Integrating Renewable Electricity on the Grid*, Washington, DC, 2011.

3       J. A. Turner, *Science*, 2004, **305**, 972–4.

4       C. Graves, S. D. Ebbesen, M. Mogensen and K. S. Lackner, *Renew. Sustain. Energy Rev.*, 2011, **15**, 1–23.

5       D. G. Nocera, *Acc. Chem. Res.*, 2012, **45**, 767–776.

6       M. G. Walter, E. L. Warren, J. R. McKone, S. W. Boettcher, Q. Mi, E. A. Santori and N. S. Lewis, *Chem. Rev.*, 2010, **110**, 6446–6473.

7       J. Rongé, T. Bosserez, D. Martel, C. Nervi, L. Boarino, F. Taulelle, G. Decher, S. Bordiga and J. A. Martens, *Chem. Soc. Rev.*, 2014, **43**, 7963–7981.

8       J. W. Ager, M. R. Shaner, K. A. Walczak, I. D. Sharp and S. Ardo, *Energy Environ. Sci.*, 2015, **8**, 2811–2824.

9       P. P. Edwards, V. L. Kuznetsov, W. I. F. David and N. P. Brandon, *Energy Policy*, 2008, **36**, 4356–4362.

10      Y. Wang, K. S. Chen, J. Mishler, S. C. Cho and X. C. Adroher, *Appl. Energy*, 2011, **88**, 981–1007.

11      A. Evans, V. Strezov and T. J. Evans, *Renew. Sustain. Energy Rev.*, 2012, **16**, 4141–4147.

12      A. Fujishima and K. Honda, *Bull. Chem. Soc. Jpn.*, 1971, **44**, 1148–1150.

13    A. Fujishime and K. Honda, *Nature*, 1972, **238**, 37–38.

14    M. S. Wrighton, D. S. Ginley, P. T. Wolczanski, A. B. Ellis, D. L. Morse and A. Linz, *Proc. Natl. Acad. Sci.*, 1975, **72**, 1518–1522.

15    J. Keeney, D. H. Weinstein and G. M. Haas, *Nature*, 1975, **253**, 719–720.

16    J. G. Mavroides, D. I. Tchernev, J. A. Kafalas and D. F. Kolesar, *Mater. Res. Bull.*, 1975, **10**, 1023–1030.

17    A. J. Nozik, *Nature*, 1975, **257**, 383–386.

18    T. Ohnishi, Y. Nakato and H. Tsubomura, *Berichte der Bunsengesellschaft für Phys. Chemie*, 1975, **79**, 523–525.

19    O. Khaselev, A. Bansal and J. A. Turner, *Int. J. Hydrogen Energy*, 2001, **26**, 127–132.

20    S. Licht, B. Wang, S. Mukerji, T. Soga, M. Umeno and H. Tributsch, *J. Phys. Chem. B*, 2000, **104**, 8920–8924.

21    K. Fujii, S. Nakamura, M. Sugiyama, K. Watanabe, B. Bagheri and Y. Nakano, *Int. J. Hydrogen Energy*, 2013, **38**, 14424–14432.

22    T. J. Jacobsson, V. Fjällström, M. Sahlberg, M. Edoff and T. Edvinsson, *Energy Environ. Sci.*, 2013, **6**, 3676.

23    C. R. Cox, J. Z. Lee, D. G. Nocera and T. Buonassisi, *Proc. Natl. Acad. Sci.*, 2014, **111**, 14057–14061.

24    G. Peharz, F. Dimroth and U. Wittstadt, *Int. J. Hydrogen Energy*, 2007, **32**, 3248–3252.

25    O. Khaselev and J. A. Turner, *Science (80-. ).*, 1998, **280**, 425 LP-427.

26    J. Luo, J.-H. Im, M. T. Mayer, M. Schreier, M. K. Nazeeruddin, N.-G. Park, S. D. Tilley, H. J. Fan and M. Grätzel, *Science (80-. ).*, 2014, **345**, 1593 LP-1596.

27    J.-W. Schüttauf, M. A. Modestino, E. Chinello, D. Lambelet, A. Delfino, D. Dominé, A. Faes, M. Despeisse, J. Bailat, D. Psaltis, C. Moser and C. Ballif, *J. Electrochem. Soc.*, 2016, **163**, F1177–F1181.

28    J. Jia, L. C. Seitz, J. D. Benck, Y. Huo, Y. Chen, J. W. D. Ng, T. Bilir, J. S. Harris and T. F. Jaramillo, *Nat. Commun.*, 2016, **7**, 13237.

29    B. A. Pinaud, J. D. Benck, L. C. Seitz, A. J. Forman, Z. Chen, T. G. Deutsch, B. D. James, K. N. Baum, G. N. Baum, S. Ardo, H. Wang, E. Miller and T. F. Jaramillo, *Energy Environ. Sci.*, 2013, **6**, 1983.

30    C. A. Rodriguez, M. A. Modestino, D. Psaltis and C. Moser, *Energy Environ. Sci.*, 2014, **7**, 3828–3835.

31    R. Bala Chandran, S. Breen, Y. Shao, S. Ardo and A. Z. Weber, *Energy Environ. Sci.*, 2018, **11**, 115–135.

32    K. Sayama, K. Mukasa, R. Abe, Y. Abe and H. Arakawa, *Chem. Commun.*, 2001, **0**, 2416–2417.

33    Y. Miseki, S. Fujiyoshi, T. Gunji and K. Sayama, *Catal. Sci. Technol.*, 2013, **3**, 1750.

34    R. Abe, T. Takata, H. Sugihara and K. Domen, *Chem. Commun.*, 2005, **0**, 3829.

35    K. Maeda, M. Higashi, D. Lu, R. Abe and K. Domen, *J. Am. Chem. Soc.*, 2010, **132**, 5858–5868.

36    S.-C. Yu, C.-W. Huang, C.-H. Liao, J. C. S. Wu, S.-T. Chang and K.-H. Chen, *J. Memb. Sci.*, 2011, **382**, 291–299.

37    C.-C. Lo, C.-W. Huang, C.-H. Liao and J. C. S. Wu, *Int. J. Hydrogen Energy*, 2010, **35**, 1523–1529.

38      H. Suzuki, O. Tomita, M. Higashi and R. Abe, *Catal. Sci. Technol.*, 2015, **5**, 2640–2648.

39      H. Kato, Y. Sasaki, N. Shirakura and A. Kudo, *J. Mater. Chem. A*, 2013, **1**, 12327.

40      R. Abe, K. Sayama and H. Arakawa, *Chem. Phys. Lett.*, 2003, **371**, 360–364.

41      Y. Sasaki, A. Iwase, H. Kato and A. Kudo, *J. Catal.*, 2008, **259**, 133–137.

42      D. M. Fabian, S. Hu, N. Singh, F. A. Houle, T. Hisatomi, K. Domen, F. E. Osterloh and S. Ardo, *Energy Environ. Sci.*, 2015, **8**, 2825–2850.

43      J. R. Bolton, S. J. Strickler and J. S. Connolly, *Nature*, 1985, **316**, 495–500.

44      M. C. Hanna and A. J. Nozik, *J. Appl. Phys.*, 2006, **100**, 074510.

45      L. C. Seitz, Z. Chen, A. J. Forman, B. A. Pinaud, J. D. Benck and T. F. Jaramillo, *ChemSusChem*, 2014, **7**, 1372–1385.

46      K. T. Fountaine, H. J. Lewerenz and H. A. Atwater, *Nat. Commun.*, 2016, **7**, 13706.

47      M. T. Winkler, C. R. Cox, D. G. Nocera and T. Buonassisi, *Proc. Natl. Acad. Sci.*, 2013, **110**, E1076–E1082.

48      C. Xiang, A. Z. Weber, S. Ardo, A. Berger, Y. Chen, R. Coridan, K. T. Fountaine, S. Haussener, S. Hu, R. Liu, N. S. Lewis, M. A. Modestino, M. M. Shaner, M. R. Singh, J. C. Stevens, K. Sun and K. Walczak, *Angew. Chemie Int. Ed.*, 2016, **55**, 12974–12988.

49      S. Haussener, C. Xiang, J. M. Spurgeon, S. Ardo, N. S. Lewis and A. Z. Weber, *Energy Environ. Sci.*, 2012, **5**, 9922.

50      S. Hu, C. Xiang, S. Haussener, A. D. Berger and N. S. Lewis, *Energy Environ. Sci.*, 2013, **6**, 2984.

51      S. Haussener, S. Hu, C. Xiang, A. Z. Weber and N. S. Lewis, *Energy Environ. Sci.*, 2013, **6**, 3605.

52    W. Shockley, *Bell Syst. Tech. J.*

53    D. M. Chapin, C. S. Fuller and G. L. Pearson, *J. Appl. Phys.*, 1954, **25**, 676–677.

54    W. Shockley and H. J. Queisser, *J. Appl. Phys.*, 1961, **32**, 510–519.

55    W. Ruppel and P. Wurfel, *IEEE Trans. Electron Devices*, 1980, **27**, 877–882.

56    A. De Vos and H. Pauwels, *Appl. Phys.*, 1981, **25**, 119–125.

57    C. H. Henry, *J. Appl. Phys.*, 1980, **51**, 4494–4500.

58    R. T. Ross and J. M. Collins, *J. Appl. Phys.*, 1980, **51**, 4504–4507.

59    P. Würfel and Wiley InterScience (Online service), *Physics of solar cells : from principles to new concepts*, Wiley-VCH, 2005.

60    C. Kittel and C. Fong, *Quantum theory of solids*, Wiley New York, 1963, vol. 3.

61    C. Kittel, *Introduction to solid state physics*, Wiley New York, 1976, vol. 8.

62    S. M. Sze and K. K. Ng, *Physics of semiconductor devices*, John wiley & sons, 2006.

63    S. H. Simon, *The Oxford solid state basics*, OUP Oxford, 2013.

64    C. C. L. McCrory, S. Jung, I. M. Ferrer, S. Chatman, J. C. Peters and T. F. Jaramillo, *J. Am. Chem. Soc.*, 2015, **137**, 4347–4357.

65    G. Liu, K. Du, S. Haussener and K. Wang, *ChemSusChem*, 2016, **9**, 2878–2904.

66    T. Hisatomi, J. Kubota and K. Domen, *Chem. Soc. Rev.*, 2014, **43**, 7520–7535.

67    K. Maeda and K. Domen, *J. Phys. Chem. Lett.*, 2010, **1**, 2655–2661.

68    F. E. Osterloh, *Chem. Soc. Rev.*, 2013, **42**, 2294–2320.

69    A. Iwase, S. Yoshino, T. Takayama, Y. H. Ng, R. Amal and A. Kudo, *J. Am. Chem. Soc.*, 2016, **138**, 10260–10264.

70    H. Zhao, X. Ding, B. Zhang, Y. Li and C. Wang, *Sci. Bull.*, 2017, **62**, 602–609.

71    H. Li, W. Tu, Y. Zhou and Z. Zou, *Adv. Sci.*, 2016, **3**, 1500389.

72    B. D. James, G. N. Baum, J. Perez and K. N. Baum, *Technoeconomic Analysis of Photoelectrochemical (PEC) Hydrogen Production*, 2009.

73    M. R. Shaner, K. T. Fountaine and H.-J. Lewerenz, *Appl. Phys. Lett.*, 2013, **103**, 143905.

74    Y. Surendranath, D. K. Bediako and D. G. Nocera, *Proc. Natl. Acad. Sci. U. S. A.*, 2012, **109**, 15617–21.

75    B. Seger, O. Hansen and P. C. K. Vesborg, *Sol. RRL*, 2017, **1**, e201600013.

76    M. F. Modest, *Radiative Heat Transfer*, Academic Press, Second., 2003.

77    S. Trasatti, *J. Electroanal. Chem. Interfacial Electrochem.*, 1972, **39**, 163–184.

78    G. Lodi, E. Sivieri, A. De Battisti and S. Trasatti, *J. Appl. Electrochem.*, 1978, **8**, 135–143.

79    J. K. Nørskov, J. Rossmeisl, A. Logadottir, L. Lindqvist, J. R. Kitchin, T. Bligaard and H. Jónsson, *J. Phys. Chem. B*, 2004, **108**, 17886–17892.

80    I. C. Man, H.-Y. Su, F. Calle-Vallejo, H. A. Hansen, J. I. Martínez, N. G. Inoglu, J. Kitchin, T. F. Jaramillo, J. K. Nørskov and J. Rossmeisl, *ChemCatChem*, 2011, **3**, 1159–1165.

81    A. Kulkarni, S. Siahrostami, A. Patel and J. K. Nørskov, *Chem. Rev.*, 2018, **118**, 2302–2312.

82    S. Keene, R. Bala Chandran and S. Ardo, *Energy Environ. Sci.*, , DOI:10.1039/C8EE01828F.

83    Q. Wang, T. Hisatomi, Q. Jia, H. Tokudome, M. Zhong, C. Wang, Z. Pan, T. Takata, M. Nakabayashi, N. Shibata, Y. Li, I. D. Sharp, A. Kudo, T. Yamada and K. Domen, *Nat. Mater.*, 2016, **15**, 611–615.

84    Q. Wang, T. Hisatomi, Y. Suzuki, Z. Pan, J. Seo, M. Katayama, T. Minegishi, H. Nishiyama, T. Takata, K. Seki, A. Kudo, T. Yamada and K. Domen, *J. Am. Chem. Soc.*, 2017, **139**, 1675–1683.

85    Y. Goto, T. Hisatomi, Q. Wang, T. Higashi, K. Ishikiriyama, T. Maeda, Y. Sakata, S. Okunaka, H. Tokudome, M. Katayama, S. Akiyama, H. Nishiyama, Y. Inoue, T. Takewaki, T. Setoyama, T. Minegishi, T. Takata, T. Yamada and K. Domen, *Joule*, 2018, **2**, 509–520.

86    R. J. Brandi, O. M. Alfano and A. E. Cassano, *Environ. Sci. Technol.*, 2000, **34**, 2623–2630.

87    R. R. Jaini and T. F. Fuller, *Int. J. Hydrogen Energy*, 2014, **39**, 2462–2471.

88    A. Busciglio, O. M. Alfano, F. Scargiali and A. Brucato, *Chem. Eng. Sci.*, 2016, **142**, 79–88.

89    C. N. Eisler, Z. R. Abrams, M. T. Sheldon, X. Zhang and H. A. Atwater, *Energy Environ. Sci.*, 2014, **7**, 3600–3605.

90    A. G. Imenes and D. R. Mills, *Sol. Energy Mater. Sol. Cells*, 2004, **84**, 19–69.

91    B. Mitchell, G. Peharz, G. Siefer, M. Peters, T. Gandy, J. C. Goldschmidt, J. Benick, S. W. Glunz, A. W. Bett and F. Dimroth, *Prog. Photovoltaics Res. Appl.*, 2011, **19**, 61–72.

92    M. A. Green, *Prog. Photovoltaics Res. Appl.*, 2012, **20**, 472–476.

93    T. Tiedje, E. Yablonovitch, G. D. Cody and B. G. Brooks, *IEEE Trans. Electron Devices*, 1984, **31**, 711–716.

94    T. Mishima, M. Taguchi, H. Sakata and E. Maruyama, *Sol. Energy Mater. Sol. Cells*, 2011, **95**, 18–21.

95 A. Augusto, S. Y. Herasimenka, R. R. King, S. G. Bowden and C. Honsberg, *J. Appl. Phys.*, 2017, **121**, 205704.

96 S. Yoshiba, M. Hirai, Y. Abe, M. Konagai and Y. Ichikawa, *AIP Adv.*, 2017, **7**, 025104.

97 O. D. Miller, E. Yablonovitch and S. R. Kurtz, *IEEE J. Photovoltaics*, 2012, **2**, 303–311.

98 I. L. Braly, D. W. deQuilettes, L. M. Pazos-Outón, S. Burke, M. E. Ziffer, D. S. Ginger and H. W. Hillhouse, *Nat. Photonics*, 2018, **12**, 355–361.

99 C.-H. M. Chuang, A. Maurano, R. E. Brandt, G. W. Hwang, J. Jean, T. Buonassisi, V. Bulović and M. G. Bawendi, *Nano Lett.*, 2015, **15**, 3286–3294.

100 E. M. Sanehira, A. R. Marshall, J. A. Christians, S. P. Harvey, P. N. Ciesielski, L. M. Wheeler, P. Schulz, L. Y. Lin, M. C. Beard and J. M. Luther, *Sci. Adv.*, 2017, **3**, eaao4204.

101 Y. Wang, X. Li, J. Song, L. Xiao, H. Zeng and H. Sun, *Adv. Mater.*, 2015, **27**, 7101–7108.

102 L. Protesescu, S. Yakunin, M. I. Bodnarchuk, F. Krieg, R. Caputo, C. H. Hendon, R. X. Yang, A. Walsh and M. V. Kovalenko, *Nano Lett.*, 2015, **15**, 3692–3696.

103 A. Swarnkar, A. R. Marshall, E. M. Sanehira, B. D. Chernomordik, D. T. Moore, J. A. Christians, T. Chakrabarti and J. M. Luther, *Science*, 2016, **354**, 92–95.

104 W. S. Yang, J. H. Noh, N. J. Jeon, Y. C. Kim, S. Ryu, J. Seo and S. Il Seok, *Science*, 2015, **348**, 1234–7.

105 S. A. Kulkarni, T. Baikie, P. P. Boix, N. Yantara, N. Mathews and S. Mhaisalkar, *J. Mater. Chem. A*, 2014, **2**, 9221–9225.